MELTING AND SOURCE VARIABILITY IN THE TONGA-KERMADEC-LAU ARC-BACK-ARC SYSTEM

A thesis submitted for the degree of Doctor of Philosophy

Macquarie University, Sydney

Presented by Milena Viktoria Schoenhofen

from Trier, Germany

Department of Earth and Environmental Sciences, Faculty of Science, Macquarie University, Sydney, Australia

29th June 2020

Resubmitted after corrections 31st January 2021

Nichts wird man je verstehen können, dachte sie. Aber im Kleinen können wir ahnen.

Marianne Fredriksson

ABSTRACT

Melting along back-arc spreading centres is dominated by decompression melting typical for ocean floor spreading but with influence by fluids from the subducting slab. Slab derived fluids may enhance the degree of melting exceeding that from decompression melting at mid-ocean ridges. Basaltic lavas occurring along back-arcs are the so-called back-arc basin basalts (BABB) showing elevated water contents and an enrichment in large-ion lithophile elements (LILE) and depleted in high-field-strength elements (HFSE) relative to normal mid-ocean ridge basalts (N-MORB). The elemental and isotopic signature of the subducting slab in lavas from the back-arc is variable in dependence of several processes, amongst which the distance from the volcanic arc and the dip of the subducting slab are particularly important.

Due to the complexity of processes influencing the composition of BABB, backarc systems are not fully understood. In order to make further constraints on the melting and source variability along back-arcs, we selected two areas that are located at the opposite ends of the Lau basin of the Tonga Arc system in the Pacific Ocean. From north to south, the Lau basin displays a decreasing distance from the arc. While the northernmost Lau basin is known as a tectonically highly active region with high mantle temperatures, the spreading rate decreases towards the southernmost Lau spreading centre. In the south, the distance from the volcanic arc is the lowest and previous studies already assumed a high subduction influence.

Major and trace element contents along with water contents and Sr-Nd-Pb isotopic ratios from the North-East Lau Spreading Centre (NELSC; Chapter 3) at the northern end of the basin were analysed to investigate the processes that are dominating the geochemical composition of melts in this area. Sampling was conducted at three different settings that have sparsely been sampled before: the transition to the rear-arc (Diagonal Ridge), the back-arc spreading centre (NELSC) and seamounts from the south. The data show that the area is influenced by three sources variably distributed along the sampled volcanic systems and reflect the heterogeneous mantle of this area. Two endmembers are highly enriched in Pb-isotopes compared to common lavas from the back-arc, and are potentially derived from Ocean Island Basalt (OIB) mantle sources. Although previous studies indicated that the mantle source signature from the subducted Louisville Seamount chain is restricted to the arc, I can show that its reactivation due to slab rollback affects also the rear-arc in this area. The spreading centre is influenced by an OIB source highly similar to the Samoan mantle plume located further north. While the southernmost seamounts are directly connected to the spreading centre and display the continuing spreading towards the south, there is no extensive melt flow between the rear-arc and spreading centre.

Previous melting models have shown that the Lau basin is dominated by two styles of melting: dry melting at the arc averted side of the spreading axis and wet melting on the arc facing side.

With increasing distance from the arc the subduction input to the overlying mantle wedge decreases and therefore the effect of wet melting decreases. In the Lau basin, this has been observed as a gradual change from north to south as the distance to the arc decreases. To further investigate the melting model, I used a sample set from an E-W transect (Chapter 4) from the southernmost tip of the Lau Basin in order to disentangle the spatial scales on which changes in fluid input from the slab influence the melts that erupt in back-arcs. Using Uranium-series and water contents, I can show that the melting zones in the Tonga backarc in <50 km distance from the arc overlap and mix with each other and a gradual decrease of the slab input cannot be seen.

STATEMENT OF ORIGINALITY

This thesis is being submitted to Macquarie University in accordance with the Cotutelle agreement (21st January 2018).

To the best of my knowledge and belief, the thesis contains no material previously published or written by another person except where due reference is made in the thesis itself.

Erlangen, 31st January 2021

STATEMENT OF THE CANDIDATE

I certify that the work in this thesis entitled **"Melting and source variability in the Tonga-Kermadec-Lau arc- back-arc sytem"** has not previously been submitted for a degree nor has it been submitted as part of requirements for a degree to any other university or institution other than Macquarie University and the Friedrich-Alexander-University Erlangen-Nürnberg and is presented here under a cotutelle agreement between these two Universities.

I also certify that the thesis is an original piece of research and it has been written by me. Any help and assistance that I have received in my research work and the preparation of the thesis itself have been appropriately acknowledged.

In addition, I certify that all information sources and literature used are indicated in the thesis.

This thesis contains material that has been prepared for publication, as follows:

Schoenhofen, M. V., Beier, C., Haase, K.M., Brandl, P.A., Romer, R.H.W., Regelous, M., Rubin, K. & Turner, S. (*in preparation*). Melting and mantle flow along the North-East Lau Spreading Centre.

My contribution to the research and paper: Concept - 90%; Data collection - 95%; Analysis - 95%; Writing - 90%; Total - 90%

Schoenhofen, M. V., Beier, C., McGee, L.E., Haase, K.M., Brandl, P.A., Regelous, M. & Turner, S. (*in preparation*). Dynamics of melting along backarc spreading centres close to subduction zones.

My contribution to the research and paper: Concept - 85%; Data collection - 95%; Analysis - 95%; Writing - 90%; Total - 90%

Erlangen, 31st January 2021

ACKOWLEDGEMENTS

First of all, I would like to thank Prof. Dr. Christoph Beier and Dr. Philipp A. Brandl for choosing me to take part in their research project, for supporting me throughout the entire time and giving me hope when I lost it.

Special thanks (or cheers!) go to my Australian supervisors Prof. Dr. Simon Turner and Prof. Dr. Bruce Schaefer giving me the great opportunity to work with you at Macquarie University and for opening me the doors to your laboratory.

Thank you Prof. Dr. Karsten M. Haase for the countless meetings, your ideas, corrections and the input that improved this thesis a lot.

I also would like to thank Dr. Marcel Regelous and Dr. Lucy E. McGee for introducing me to the world of U-Series, column chemistry and machine analyses. Thanks for your patience, for answering me a ton of questions and giving me more self-confidence. Thanks a lot, to all the people that provided help during the analyses in Erlangen, Sydney, Canberra and Wollongong: H. Brätz, M. Hertel, Dr. Y. Lai, P. Wieland, Prof. Dr. T. Ireland, A. Dossetto, A. Francke and J. Sikdar.

Thanks to all my colleagues in at the GeoZentrum in Erlangen: Amelie, Anna, Betti, C. Scharf, David, Domenico, Dominic, Fred, Henning, Jan, Johann, Katha, Fred, Manuel, Meike, Patrick, Tobi, Thomas, Simon, Stefan, Yadong and all the others I might forgot to mention because I am so bad with names.

Thanks to all the amazing people I met during my stay in Sydney – Ala, Ana, Alex, Ben, Coti, Franky, Hindol, John, Julia, Kui, Laura, Lauren, Micha, Rosa, Tomas, Zai and many, many more! You made the time abroad so much better. I especially want to thank Basti and Inès for being there for me and supporting me throughout my stays and to Thusitha for all the funny moments, trips and for being an amazing friend. Dear Marina, I have no idea what I would have done without you. I am so grateful that we have met, my soulsister! Thank you for your support, your hugs, all the teas/moments/thoughts we shared and for making me feel like home in Australia.

I also would like to thank my dear friends Ali, Astrid, Emy, Franzi, Kolli, Philipp, Resi and Steffi for supporting me during this time, for your calls, messages, kind words and for just being there! Kathi and Andy, I am unbelievable grateful for your support, help and dinners, the distraction from work and your open ears.

I would like to thank my family for your support, your help, your love and that you always gave me the feeling that I am enough! Thank you for always being there for me and making home

such a solid anchor. Momo and Gisbert, I also want to thank you for making the hard times so much more bearable.

I would never be able to write these acknowledgments without this one special person. You supported me in the best and worst times, helped me, believed in me. You spent your weekends in the lab, flew around the world and stayed up late to spend time with me. Thank you for being such an amazing person, for every single second with you and for helping me finishing up this thesis.

I want to acknowledge the very constructive and helpful comments of the reviewers R. Arculus, M. Handler and L. Kirstein.

I also acknowledge the support from Macquarie University in form of an Australian Government Research Training Program (RTP) Scholarship and the Deutsche Forschungsgemeinschaft (DFG) by funding this research the projects BE 4459/8-1 and BR 5297/2-1. Thanks for the support.

CONTENTS

LIST OF FIGURES

1 INTRODUCTION

3 MELTING AND MANTLE FLOW ALONG THE NORTH-EAST LAU SPREADING CENTRE

LIST OF TABLES

FULL PUBLICATION LIST

PEER-REVIEWED PUBLICATIONS

Schoenhofen, M. V., Haase, K. M., Beier, C., Woelki, D., & Regelous, M. (2020). Chemical evolution of calc-alkaline magmas during the ascent through continental crust: constraints from Methana, Aegean arc. Journal of Petrology.

Woelki, D., Haase, K. M., **Schoenhofen, M. V.**, Beier, C., Regelous, M., Krumm, S. H., & Günther, T. (2018). Evidence for melting of subducting carbonate-rich sediments in the western Aegean Arc. Chemical Geology, 483, 463-473.

PUBLICATIONS IN PREPARATION

Schoenhofen, M. V., Beier, C., Haase, K.M., Brandl, P.A., Romer, R.H.W., Regelous, M., Rubin, K. & Turner, S. (in preparation). Melting and mantle flow along the North-East Lau Spreading Centre.

Schoenhofen, M. V., Beier, C., McGee, L.E., Haase, K.M., Brandl, P.A., Regelous, M. & Turner, S. (*in preparation*). Dynamics of melting along backarc spreading centres close to subduction zones.

CONFERENCE ABSTRACTS

Schoenhofen, M. V., Beier, C., Haase, K. M., Regelous, M., Turner, S. P., & Brandl, P. A. (2019) Goldschmidt Abstracts, 2019 3012.

Schoenhofen, M. V., Beier, C., Brandl, P. A. and Turner, S. P. (2017). Dynamics of melting in the Valu Fa- Lau Basin backarc. Presented at GeoBremen 2017.

Schoenhofen, M. V., Woelki, D., Haase, K. M., & Beier, C. (2017). Goldschmidt Abstracts, 2017 3551.

1 INTRODUCTION

1.1 OUTLINE OF THE THESIS

This thesis targets the formation and evolution of magmas in the Tonga Arc and Lau backarc systems (Figure 1.1) which has previously been subject to studies. New and existing data are used to investigate the transition in magma sources and melting regimes between the arc and backarc in the northern Lau Basin and along the Valu Fa area, not explored to date, using major element, trace element, H_2O contents and U-series isotope geochemistry of new samples from the northern Lau Basin sampled during expedition RV Sonne 263 TongaRift (Haase et al., 2018), combined with available and/or previously published samples (references are given in the respective chapters).

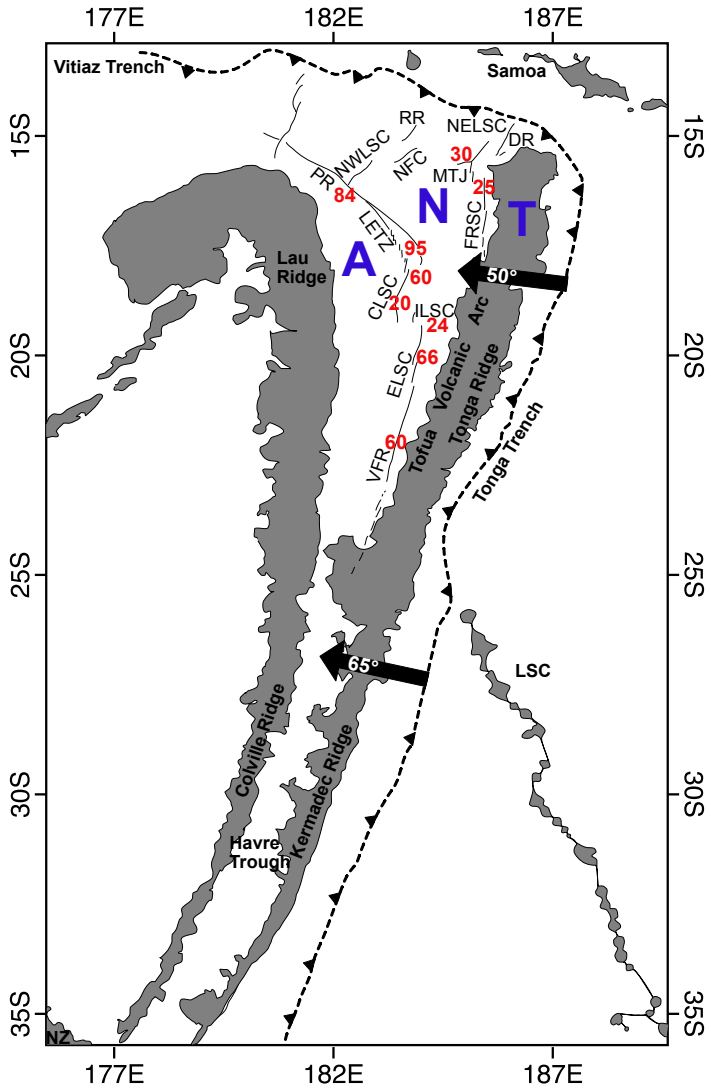

Figure 1.1 *Map of the Tonga-Kermadec subduction zone and Lau basin-Havre Trough backarc system in the SW Pacific south of the Vitiaz Trench and the Samoa islands adapted after (Pearce et al., 2007). The Tonga Trench is located east of the arc system and New Zealand (NZ) is located south of the region. The Tonga Arc is divided into the remnant Lau Ridge and Tonga Ridge with the active Tofua Arc in between. The northernmost spreading centres in the Lau Basin are the Rochambeau Rift (RR), the Niuafo'ou Spreading Centre (NSC), the North-West and North-East Lau Spreading Centres (NWLSC and NELSC), the Diagonal Ridge (DR), the Mangatolu Triple Junction (MTJ) and Fonualei Rift Spreading Centre (FRSC). Further south, the Peggy Ridge (PR) transitions over the Lau Extensional Transform Zone (LETZ) to the south in the Central LSC (CLSC) followed by the Intermediate LSC (ILSC) to the Eastern Lau Spreading Centre (ELSC) and the Valu Fa Ridge (VFR). Spreading rates in red (Baker et al., 2019; Bevis et al., 1995; Parson and Wright, 1996; Sleeper et al., 2016). The Kermadec Arc in south of the Louisville Seamount Chain (LSC) is divided into the remnant Colville Ridge and the Kermadec Ridge in the west with the Havre Trough in between. The black arrows display the subduction angles by van der Hilst (1995). In blue the Australian (A), Niuafo'ou and Tonga (T) Plates (Zellmer and Taylor, 2001).*

The northernmost Lau Basin is known as a tectonically active and complex region which is influenced by spreading rates of up to 4.2 cm/a (Baker et al., 2019; Sleeper et al., 2016) and high mantle temperatures of ~1450°C (Kelley et al., 2006; Wiens et al., 2006). Previous studies have been dealing with the different spreading centres in this region (Figure 1.1) like the Mangatolu Triple Junction, the North-West Lau Spreading Centre or the Peggy Ridge forming from a compositionally heterogeneous mantle in the northern Lau Basin (e.g. Tian et al. (2011), (Hawkins, 1995), Escrig et al. (2012), Paropkari et al. (2010), Jenner et al. (2012)). Nevertheless, little is known about the North-East Lau Spreading Centre (NELSC), which is

both closest to the adjacent arc and the northern trench due to relatively sparse sampling (Clague et al., 2010; Falloon et al., 2007; Haase et al., 2018; Resing et al., 2011).

During R/V *Sonne SO263 TongaRift* cruise in 2018, we collected a new sample set from the NELSC along with the adjacent seamounts and the DR (Diagonal Ridge) extending from the reararc volcano Niuatahi towards the NELSC. Three alkaline seamounts to the south of the NELSC are not directly connected to the active NELSC and are expected to represent the youngest volcanic edifices of the southwestwards propagating NELSC. The DR connects the Niuatahi volcano and the NELSC and samples retrieved from the DR are young, fresh volcanic glasses and volcaniclastic rocks (Haase et al., 2018) allowing to investigate the melting processes and changes of the mantle sources from the arc into the backarc. In this work (Chapter 3), I focus on major and trace element, water and isotope analyses from the NELSC (Figure 1.1) along with literature data from the adjacent arc and backarc settings (references are provided in Chapter 3). The main aim is to decipher the processes influencing the magmas in this area, i.e. deciphering the input from the subducting slab components, the depleted mantle wedge and an enriched component comparable to Ocean Island Basalts (OIB) ubiquitous to this region (Beier et al., 2017; Falloon et al., 2007; Jenner et al., 2012; Price et al., 2016; Price et al., 2014). By comparing the influence from the subducting slab components, mantle wedge depletion and partial melting of the different localities, the different magma sources are identified and mantle heterogeneities influencing volcanism in this region. Moreover, the geodynamic relationship between the NELSC, southernmost seamounts and DR is discussed, and I finally conclude on the distribution of mantle sources and melt flows in this region.

Melts in backarcs and island arcs may either form by adiabatic decompression or fluid-fluxed melting or a combination of both (Figure 1.2). The highly variable structural features and magmatic conditions from the arc into the backarc environment provide a unique opportunity

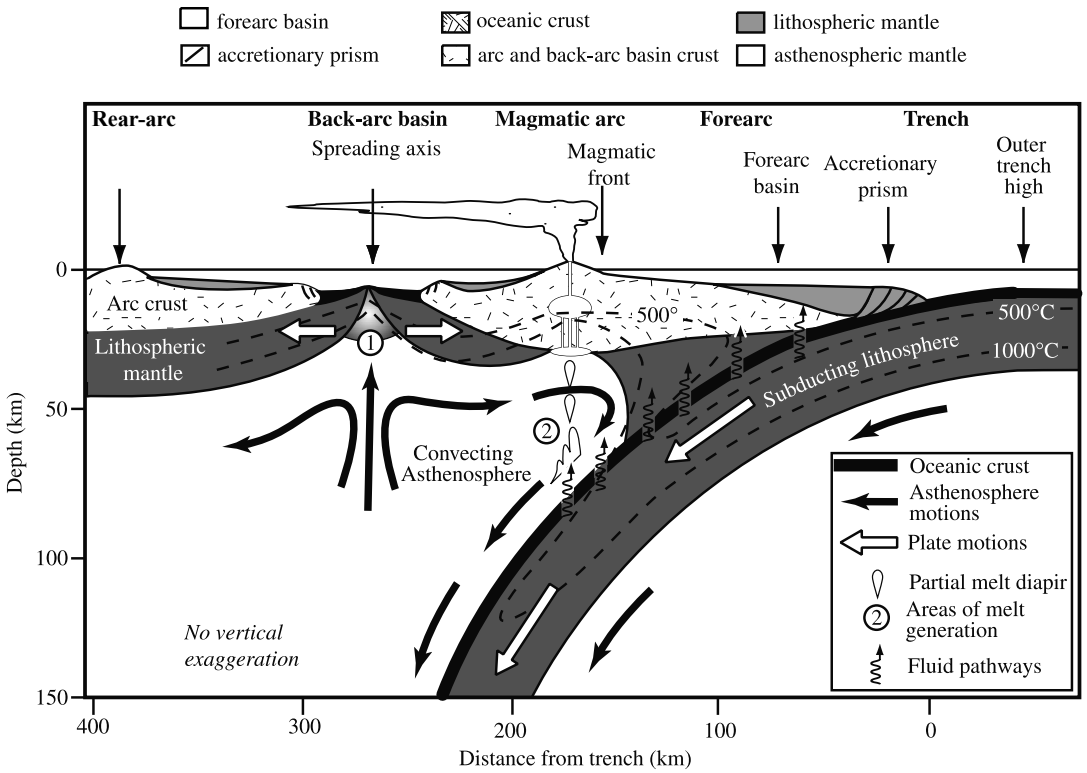

Figure 1.2 *Schematic section through a subduction zone adapted after Stern (2002).*

to investigate a large diversity of magmatic processes related to both arc and backarc melt generation. Previous works mostly focused on the N-S transect along the Lau Basin showing differences in fluid influence and style of melting with decreasing distance to the arc. One of the influential models by Langmuir et al. (2006) shows a gradual transition from fluid fluxed melting closer to the arc towards decompressional melting dominated in the backarc. They propose a two-sided melting model (Figure 1.3a) in which the side closer to the arc is influenced by hydrous, shallow melting (<100 km distance to the arc) and less hydrous to dry melting on the backarc spreading centre side distal to the arc (>100 km distance to the arc) comparable to mid ocean ridges uninfluenced. Their model (Figure 1.3a) suggests that the hydrous input from the arc decreases with increasing distance like e.g. in the northern Lau Basin (Langmuir et al., 2006). On the other hand, e.g. Sleeper and Martinez (2014) propose an overlap of melting zones that separate with increasing distance to the arc, i.e. towards the northern Lau Basin (Figure 1.3b). The model shows three distinct mantle domains with a

hydrous domain <70 km distant from the arc generating shallow andesitic to deep basaltic melts that is followed by a more dry, depleted domain which transitions to a mantle comparable to MORB composition (Sleeper and Martinez, 2014). Backarc magmatism located in arc proximity (<50 km) is dominated by the hydrous domain (Figure 1.3b.3), while more distant backarcs are dominantly influenced by adiabatic decompressional melting domains (Figure 1.3b.1-2) (Sleeper and Martinez, 2014).

To further distinguish between these models (Chapter 4), I choose seven samples from a transect across the southernmost Valu Fa Ridge which is situated ~40 km distant from the active Tonga Arc. Based on new U-series and H_2O analyses I investigate the melting regime to show the differences between arc and backarc influenced melting in proximity to the arc.

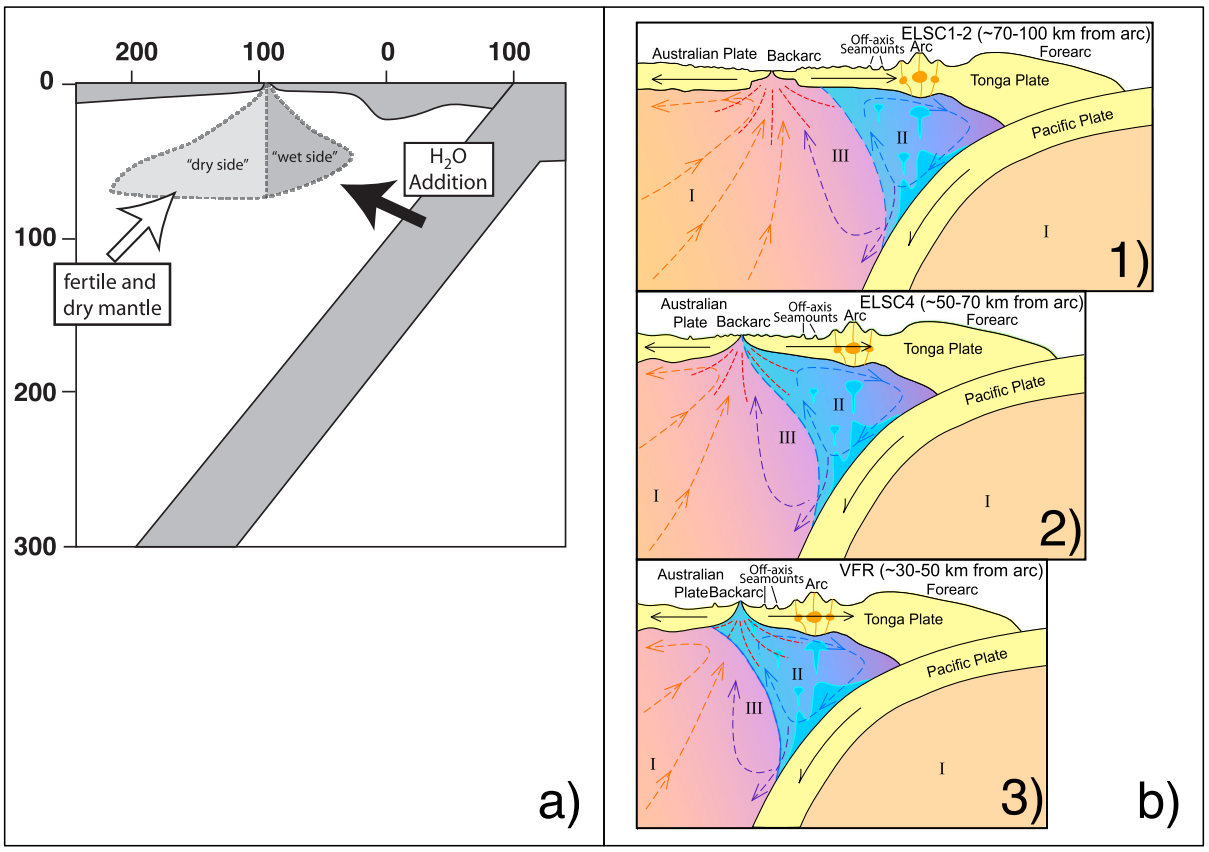

Figure 1.3 *Melting models for backarc magmas from a) Langmuir et al. (2006), showing the two-sided model with a wet-side close and a dry side distal to the arc and b) Sleeper et al. (2016) showing three distinct mantle domains (I – III) with changing influence of the hydrous domain (II) with decreasing distance between arc and backarc from 1) to 3).*

I can show that the transition between dry and wet melting regimes may variably depend on the distance between the arc and backarc, i.e. at distances of less than 50 km the overlapping melting zones of the arc and backarc do not easily allow a distinction into a wet and dry side of melting. Instead, abundant mixing of sources and magmas overprints the geochemical signatures derived from the subducting slab.

1.2 SUBDUCTION ZONES AND BACKARC BASINS

Oceanic and continental subduction zones are the major regions of mass exchange on Earth and act as a driver for modern plate tectonics (Tatsumi and Kogiso, 2003). At these convergent margins, oceanic crust, sediments and lithosphere (Figure 1.2) are subducted and “recycled” into the Earth’s mantle (Stern, 2002). The major surface expression of subduction zones are deep-sea trenches and volcano chains combined with the largest gravity anomalies overserved globally and frequent strong, shallow and deep earthquakes. These regions are commonly referred to as oceanic and continental arcs which form from a combination of dehydration of the subduction slab, slab melting and melting of the overlying mantle wedge (Tatsumi et al., 1983). The mafic magmas ascend through crust of variable thickness (Leeman, 1983; Plank and Langmuir, 1988) and are chemically modified during formation, melt extraction and ascent (Plank and Langmuir, 1988; Profeta et al., 2015; Woodhead et al., 1993).

The major geological components influencing the composition and petrological variability of magmas erupted in a subduction zone system are: the subducting oceanic lithosphere with variable amounts of oceanic and continental sediments, the mantle wedge and the arc-trench complex (Figure 1.2) which forms as a result of subduction (Stern, 2002). The subduction angle and geometry are highly influenced by plate motion, convergence and age and composition of the subducting plate (Cross and Pilger, 1982). The lithosphere density increases with age and shallow angles are observed at subduction of young plates (Cross and Pilger, 1982). Both the subduction zone geometry and magma composition along the arc and backarc are influenced

by the subduction of volcanic edifies like intraplate seamount chains, along the subducting plate (Cross and Pilger, 1982). The composition and state of alteration of the subducting crust and the thickness of the arc crust impact on the geochemical composition of the arc magmas involved. Due to the nature of the geological components involved, i.e. subducting oceanic crust, its degree of alteration/serpentinization, the thickness of the sediment layer, variably thick island arc crust and mantle wedge material, subduction zones are key drivers for the recycling of major and trace elements and volatiles between the Earth's surface and interior (Rüpke et al., 2004; Stern, 2002). A major factor for water storage and release during subduction is the degree of serpentinization of the lithospheric mantle that releases up to 40% of its stored water during the subduction process (Rüpke et al., 2004). These factors together may act as drivers e.g., for the deep H_2O or CO_2 cycles globally (van Keken et al., 2011; Wallace, 2005).

The subducting plate is subject to significant increases in temperature and pressure, during which metamorphic reactions take place (Peacock, 1990; Peacock, 2003). As the mineral assemblages and volatile content change, significant amounts of aqueous fluids and melts are released (Davies and Stevenson, 1992; Kogiso et al., 1997; Peacock, 1990; Stern, 2002; Tatsumi et al., 1986). The classic view is that these fluids ascend from the subducting slab (Figure 1.2) to the variably depleted mantle wedge causing fluid flux melting of the depleted mantle wedge by lowering of the mantle solidus (Tatsumi and Eggins, 1995). This mantle melting is driven by the solid flow of the mantle wedge and the location and width of the melting region is dependent on the convergence rate and the correlated mantle temperatures (Cagnioncle et al., 2007). The composition of the arc magmas is highly influenced by the mantle wedge thermal structure and upper plate thickness (Turner et al., 2016). The thermal structure is influenced by the slab dip (Cagnioncle et al., 2007) and impacts on the arc magma composition by the degree of magma migration and the degree of melting (Jones et al., 2018). Also, arc lavas typically show elevated concentrations of fluid-mobile elements like large ion

lithophile elements (LILEs) derived from the subducting igneous and sedimentary portions of the slab influencing the trace element and stable and radiogenic isotopic composition of the lavas. Moreover, lavas erupted along arcs are often water-rich (up to 6 wt.% H_2O; Johnson et al. (1994)) and show a high degree of depletion of the high field strength elements (HFSE) due to previous melt extraction (Pearce, 1983; Pearce and Stern, 2006a; Stern, 2002; Woodhead et al., 1993). Nevertheless, nearly anhydrous melting occurs along arcs (Conder et al., 2002; Jagoutz et al., 2011; Kohut et al., 2006). The general fluid-induced melting is not applicable due to the low water contents of these melts, wherefore adiabatic decompressional melting for generating these lavas is expected. The subducting slab abrades the base of the overriding plate which leads to corner flow by filling the newly built gap with asthenosphere (Conder et al., 2002). The thinning of the abraded overriding plate in combination with the upwelling of hot asthenosphere, decompressional melting is triggered (Conder et al., 2002).

The formation of backarc basins behind the arc is dependent on the age and dip of the subducting plate (Sdrolias and Müller, 2006). They are developed at lithosphere ages >55 Ma and dips of >30° (Sdrolias and Müller, 2006). Different models for backarc formation have been proposed due either to opposite slab movement while the slab is stagnant within the deeper mantle or to slab rollback (Heuret and Lallemand, 2005). The investigation of lavas from backarc spreading centres relatively close to arc systems (e.g., in the Manus Basin, Lau backarc or Izu-Bonin) is advantageous over using island arc lavas in that the overlying lithospheric lid is relatively thin allowing for a relatively undisturbed view into the upper mantle processes of dehydration, melting and magma mixing (Pearce and Stern, 2006a).

Backarc basins are generally relatively shallow (<3000 meters below sea level, mbsl) (Hawkins, 1995). The new oceanic crust formed at backarcs is comparable in its stratigraphy to that from mid-ocean ridges (MOR) and is formed simultaneously to the island arc lavas (Hawkins, 1995), however, is compositionally distinct in that backarcs commonly form from a combination of enriched, subducting sources and depleted mantle (Kelley et al., 2006;

Langmuir et al., 2006; Taylor and Martinez, 2003) and may range from volatile-rich backarc basin basalts (BABB) to normal MORB (Beier et al., 2010; Sinton et al., 2003). The melting mechanism along backarcs is generally dominated by decompression melting (Kelley et al., 2006) where the passively upwelling asthenosphere, due to the extensional movement, rises adiabatically above the solidus (Asimow et al., 1995). Nevertheless, geochemical signatures show that the backarc magmas are distinct from MORBs (Figure 1.4), erupting BABB seen for example in low Na, Ti, Fe and HFSE concentrations and enrichment in H_2O and LILEs (Gill, 1976; Pearce and Stern, 2006a; Taylor and Martinez, 2003) compared to depleted MORB (Workman and Hart, 2005). BABBs are variably influenced by different degrees of input from the depleted wedge mantle and the varying subduction zone components, mixing of the distinct sources, the degrees of mantle melting and different assimilation or fractionation processes as the magmas ascend (Pearce and Stern, 2006a). The most common geochemical differences between normal MORB and BABBs are enhanced water contents and increased LILE concentrations along backarcs derived by the adjacent arc, which also leads to higher degrees of partial melting (Pearce and Stern, 2006a).

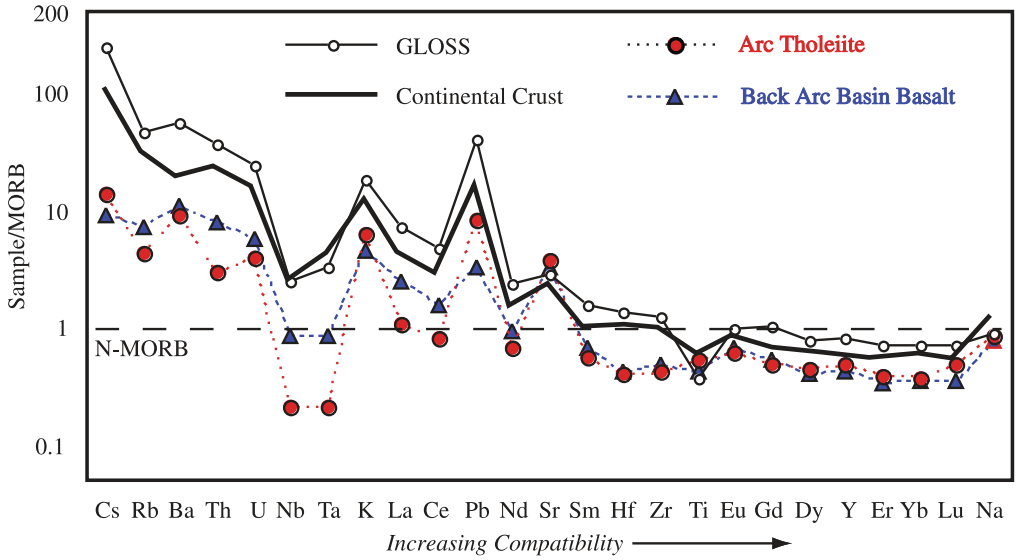

Figure 1.4 *Element variations in a multielement diagram displaying differences between arc tholeiites (red), backarc basalts (blue), average continental crust and average sediment composition (GLOSS) in comparison to N-MORB adapted after Stern (2002) and references therein. Elements are listed by increasing compatibility from left to right. Both arc and backarc lavas are enriched in LILE (Rb, Ba, U, K, Pb and Sr) while being depleted in HFSE (Nb, Ta, Zr, Ti, Y and HREE) relative to N-MORB.*

The major aim of the thesis is to improve our understanding of the transition between fluid flux melting in the arc towards a decompression-dominated melting regime more distant from the arc using samples derived from backarcs (Langmuir et al., 2006; Pearce and Stern, 2006a; Taylor and Martinez, 2003).

1.3 THE TONGA-KERMADEC ARC AND LAU BASIN BACKARC SYSTEM

In this chapter I will present a brief overview of the geological and geodynamic setting of the study area of my thesis. The Tonga-Kermadec Arc and Lau Basin backarc system is located in the Southwest Pacific (Figure 1.1) and is part of a near continuous system of subduction zones along the western margin of the Pacific Plate.

1.3.1 The Tonga-Kermadec island arc

The NNE-trending Tonga-Kermadec island arc system is located in the Southwest Pacific between the islands of Samoa and New Zealand (Figure 1.1). The northern Samoa island chain is formed by a mantle plume influencing the northern part of the Tonga-Lau system (Danyushevsky et al., 1995; Falloon et al., 2007; Jenner et al., 2012; Nebel and Arculus, 2015; Wendt et al., 1997). The OIB source is highly complex including the diverse endmembers of OIB sources like enriched, depleted and Focal Zone (FOZO; ε_{Nd}~3–4) components (Nebel and Arculus, 2015). The Samoa plume fractions are proposed to be mixed with the local backarc mantle sources in the upper mantle and being dragged southwards (Nebel and Arculus, 2015).

The arc extends for over 2500 km from the Taupo Volcanic Zone (North Island, New Zealand) in the south to the Vitiaz strike-slip zone in the north (Caulfield et al., 2012; Turner et al., 1997). The intra-oceanic subduction zone system results from subduction of the Pacific Plate under the Australian Plate (Caulfield et al., 2012; Turner et al., 1997) and subduction initiated in the Eocene (Sutherland et al., 2020). The Tonga-Kermadec Arc system is known for the highest plate motion rates globally; however, the subduction rate is not constant along the trench but

increases from 50 mm/a in the south up to 240 mm/a in the north (Bevis et al., 1995). Subduction of the Louisville Seamount Chain (LSC) as part of the Pacific Plate results in a morphological discontinuity and separates the island arc system into a northern Tonga (Tofua) Arc and southern Kermadec Arc (Ewart and Hawkesworth, 1987).

The volcanoes along the Tonga-Kermadec Arc are located 100 km above the subducting slab (Smith and Price, 2006). The volcanoes are distributed continuously along the whole Tonga-Kermadec Arc with the subaerial volcanoes concentrated in a zone of 40 km width, while older arc volcanoes are distributed further west within the Havre Trough (Smith and Price, 2006). Most volcanoes are not located straight on the ridge axis but distributed with variably distance to the ridge crest (Graham et al., 2008; Smith and Price, 2006). The distance between arc and trench varies along the Tonga-Kermadec Arc. Cross and Pilger (1982) identified different aspects controlling the subduction angle and therefore the distance between arc and trench: the relative convergence rate, the absolute plate motion, the subducting lithosphere's age and the subduction of large quantities of sediment, ridges or ocean island chains. In the northern part of the Tonga-Kermadec Arc, the slab angle is ~50° changing towards near 0° in the transition zone between 400 and 700 km depth before it reaches into the lower mantle (van der Hilst, 1995). In contrast, the southern part of the arc is influenced by a steeper angle (~65°) and no changes along the transition zone can be seen (van der Hilst, 1995).

The northern Tonga Arc is divided into two island chains with the Tonga Ridge representing the remnant arc in the east and the active Tofua Arc to the west (Figure 1.1). Recent arc magmatism along the Tofua arc (Table 1.1) is located about 120 to 150 km west of the Tonga Trench (Ewart et al., 1977; Ewart and Hawkesworth, 1987; Keller et al., 2008). A remnant Miocene-aged arc is located west of the Lau Basin backarc and is named Lau Ridge (Figure 1.1) (Smith and Price, 2006). The Tonga Arc follows the trench shape and is curved at the northern end towards the west where it transitions into the Vitiaz Lineament (Figure 1.1). The northern part of the arc forms a broad plateau with elevated water depths (Smith and Price,

2006). The central Tonga Arc is broader but shallower and the volcanoes are located 55–65 km west of the platform's axis mostly lying subaerial (Smith and Price, 2006). In the southern Tonga Arc, all volcanoes but Ata are submarine (Smith and Price, 2006).

The area that marks the border between the Tonga and Kermadec Arc is dominated by a west–south–west trending fracture influenced by the LSC (Smith and Price, 2006). The LSC, separating the Tonga from the Kermadec Arc, is a ~4200 km long chain of age-progressive

	Timing	Observation	youngest activity/ evidence	*References*
ARC	~66 Ma	ages of seamounts closest to modern arc		*Cheng et al., 1987; Ewart et al., 1998*
	~55 Ma	Subduction initiation	until present	*Sutherland et al., 2020*
	~51 Ma	oldest forearc plagiogranites found at Tonga		*Sutherland et al., 2020; Meffre et al., 2012*
	~48 Ma	first evidence for arc magmatism at Tonga	until present	*Sutherland et al., 2020; Meffre et al., 2012*
	~46-40 Ma	Eua; Tonga Ridge (Eocene basement)	17 Ma: youngest dykes	*Hergt & Woodhead 2007; Duncan et al., 1985*
	~25 Ma	first evidence of volcanism on Lau-Colville-Three Kings Arc		*Yan, 1993; Ewart et al., 1998*
	~16.7 Ma	oldest Colville Ridge samples		*Mortimer et al., 2010*
	~14-5.4 Ma	first stage of Lau Ridge magmatism	until 0.3 Ma: youngest stage	*Gill (1976), Woodhall (1985), Whelan et al. (1985), Hergt & Woodhead, 2007*
	~5-4 Ma	Subduction of LSC		*Regelous et al., 1997; Ruellen et al., 2003*
	~3.5 Ma	first recorded Tofua Arc samples	until present	*Tappin et al., 1994; Hergt & Woodhead, 2007*
LAU BASIN	~6 Ma	Initial opening of the Lau Basin	until present	*Taylor et al., 1996*
	~5-4.5 Ma	Lau Basin spreading initiation along PR towards ELSC		*Martinez et al., 2006; Tian et al., 2008*
	~1.5-1.2 Ma	Opening CLSC		*Martinez et al., 2006; Tian et al., 2008*
	~0.9-0.7 Ma	Opening VFR		*Vallier et al.., 1991*
HAVRE TROUGH	~5.5 Ma	Initial opening of the western Havre Trough	until ~2.0 Ma	*Tontini et al., 2019*
	~2.0	Initial opening of the eastern Havre Trough	until present	*Tontini et al., 2019*

Table 1.1 *Summary table of timings of key tectono-magmatic events in the Tonga-Kermadec region (Cheng et al., 1987; Duncan, 1985; Ewart et al., 1998; Gill, 1976; Hergt and Woodhead, 2007; Martinez et al., 2006; Meffre et al., 2012; Mortimer et al., 2010; Regelous et al., 1997; Ruellan et al., 2003; Sutherland et al., 2020; Tappin et al., 1994; Taylor et al., 1996; Tian et al., 2008; Tontini et al., 2019; Vallier et al., 1991; Whelan et al., 1985; Woodhall, 1985; Yan, 1993).*

seamounts that intersects the Tonga-Kermadec Arc system at 25.6°S (Beier et al., 2011; Hawkins et al., 1987; Smith and Price, 2006). At least 60 seamounts and guyots are lined up from the Tonga-Kermadec trench to the Pacific-Antarctic Ridge (Hawkins et al., 1987) that formed in the past 80 Ma along the Pacific plate by a hotspot (Koppers et al., 2004). The subduction of the LSC started about 4 to 5 Ma ago beneath the northern paleo-Tonga trench and the subduction angle increased significantly from 0° to 36° (Ruellan et al., 2003). The southward migration of the Tonga Arc rotation pole is associated with a southward migration of subduction of the LSC seamounts (Ruellan et al., 2003). By today, the LSC has covered more than 880 km distance southward leaving in its wake the geochemical signatures from the intraplate volcanoes (Ruellan et al., 2003; Turner et al., 1997). The transition zone between Tonga and Kermadec Arc shows a shoal zone resulting from the subduction of the LSC (Timm et al., 2013).

The Kermadec Arc system contains two remnant ridges (Table 1.1), the Colville Ridge in the west and the Kermadec Ridge in the east, the active Kermadec Arc front and the active Havre Trough backarc basin (Timm et al., 2019). The Kermadec Arc system continues in a curved line of volcanoes towards the south with a narrower and deeper ridge than the Tonga Arc (Smith and Price, 2006). The Transition Zone between the Kermadec and Tongan arc, including the Monowai submarine volcano is located 10 to 30 km west of the Tonga Ridge (Smith and Price, 2006; Timm et al., 2011). The active arc front is located west of the Kermadec Ridge except for the region between 29° and 32°S where it is located on the Kermadec Ridge crest (Bassett et al., 2016). Active volcanism along the Kermadec Arc system occurs along a single ~1200 km long chain of volcanoes about 150 to 180 km from the Kermadec trench (Caulfield et al., 2012; Ewart et al., 1977; Ewart and Hawkesworth, 1987) and extends in the south on continental crust (Ngatoro Ridge) (Turner et al., 1997). The Colville Ridge is the elongation of the Lau Ridge, while the Kermadec Ridge is the elongation of the Tonga Ridge

and both remnant ridges are segmented and narrow towards the south from ~60 km at >32°S to >30 km at <35°S (Bassett et al., 2016; Timm et al., 2013).

1.3.2 The Lau Basin-Havre Trough backarc system

Backarc spreading in the Lau Basin-Havre Trough region started about 6 Ma ago (Table 1.1) along with the progression of the Pacific plate boundary to the east, moving the Lau and Colville Ridges westward (Ewart et al., 1977; Hawkins, 1995; Vallier et al., 1991).

The entire Lau Basin is >1000 km long and the width ranges from 450 km in the north to 200 km in the south (Keller et al., 2008) resulting from the successive propagation of backarc opening to the south (Hawkins, 1995). It is enclosed by the remnant Lau Ridge in the west and the Tonga Arc in the east. Spreading rates range from ~3 cm/a in the north along the Mangatolu Triple Junction (MTJ) (Sleeper et al., 2016) to 8.2 cm/a at the Central Lau Spreading Centre (CLSC) to 9.0 cm/a along the East Lau Spreading Centre (ELSC) decreasing to a spreading rate of 6.2 cm/a in the south (Valu Fa Ridge; VFR) (Taylor et al., 1996; Zellmer and Taylor, 2001).

The northern Lau Basin is a triangular-shaped backarc basin (Figure 1.1) known for its tectonic complexity (Baxter et al., 2020), and high spreading rates and several distinct spreading centres (Escrig et al., 2012). Most spreading centres in the Lau Basin are aligned in a S to SW direction (Keller et al., 2008). The system of spreading axes is composed of at least six main spreading centres from north to south: Peggy Ridge (PR) and the Lau Extensional Transform Zone (LETZ), a central, intermediate (ILSC) and eastern spreading centre and the VFR. There are several smaller spreading centres in the northernmost Lau Basin with the Niuafo'ou Spreading Centre (NSC) propagating from NE in SW direction down to the NWLSC (North-West Lau Spreading Centre). The NWLSC merges into the PR, the NELSC and DR close to the MTJ (also known as Kings Triple Junction) north of the Fonualei Rift and Fonualei Rift Spreading Centre (FRSC). The FRSC extends southwards to the subaerial Fonualei arc

volcano. A three-plate kinematic model for the opening of the Lau Basin was proposed by Zellmer and Taylor (2001) for the time since the last geomagnetic pole shift (Brunhes Chron). They show that the Niuafo'ou microplate is separated from the Australian Plate by the PR, LETZ and CLSC, and that the FRSC separates it from the Tongan Plate, a microplate located along the Tongan forearc, while the ELSC describes the border between the Australian and Tongan Plates, respectively (Figure 1.1). The backarc rifting in the Lau Basin started ~6 Ma (Hawkins, 1995), while spreading was initiated ~5 to 4.5 Ma along the PR and propagated southwards forming the 400-km-long ELSC and the CLSC since 1.5 to 1.2 Ma (Martinez et al., 2006; Tian et al., 2008). Nowadays, the two segments are connected by the ILSC (Tian et al., 2008).

In the south, the spreading rates decrease to 6 cm/a along the VFR (Vallier et al., 1991). This part of the Lau Basin has been active for only 0.7 to 0.9 Ma (Vallier et al., 1991). The narrow NE trending spreading axis is located only 40 to 50 km west of the adjacent Tofua arc (Vallier et al., 1991), correlating with the fact that the Lau spreading axes are curved towards the Tofua arc in southern direction and the arc-backarc distance decreases (Zellmer and Taylor, 2001).

The Australian-Tongan plate pole is located close to the transition zone of the Lau Basin in the north and the Havre Trough (Figure 1.1) in the south (Zellmer and Taylor, 2001). This leads to a non-copolar extension of the two basins with faster opening rates along the Lau Spreading Centre (Zellmer and Taylor, 2001).

The Havre Trough is a ~110 km (N) to ~50 km (W) wide backarc basin located between the Kermadec Ridge in the west and the remnant Colville Ridge in the east that stated opening ~5.5 Ma (Tontini et al., 2019). The spreading rates decrease from 5.5 cm/a in the north to 2.7 cm/a in the south (Bird, 2003; Smith and Price, 2006). Tontini et al. (2019) propose the first stage of spreading started about 5.5 Ma due to trench rollback and the second stage shows a

shift of tectonic activity from the western to the (still active) eastern part of the Havre Trough ~2 Ma ago.

1.4 PRINCIPLES OF URANIUM-SERIES

A major part of the thesis was the analysis of uranium series isotopes (^{238}U, ^{230}Th, ^{226}Ra) in lavas from an E-W transect along the southernmost VFR. These isotopes can be used to determine the timescales of slab dehydration, melting and fractionation processes in subduction zone systems (Bourdon et al., 2003a). The method is based on the naturally occurring radioactive decay of the long-lived nuclides ^{238}U, ^{235}U and ^{232}Th (parent isotopes) to stables isotopes of Pb, via a chain of short-lived radioactive nuclides (Figure 1.5). The half-lives of the daughter isotopes are very short in comparison to the parent isotopes except for ^{234}U, ^{230}Th and ^{226}Ra (Figure 1.5) which can therefore be taken to investigate the processes and timescales in magmatic systems.

For further processing the data, the activity ratios (A_i) were calculated by multiplying the decay constants (λ_i) by the numbers of atoms (N_i). Activity ratios denoted by brackets show the

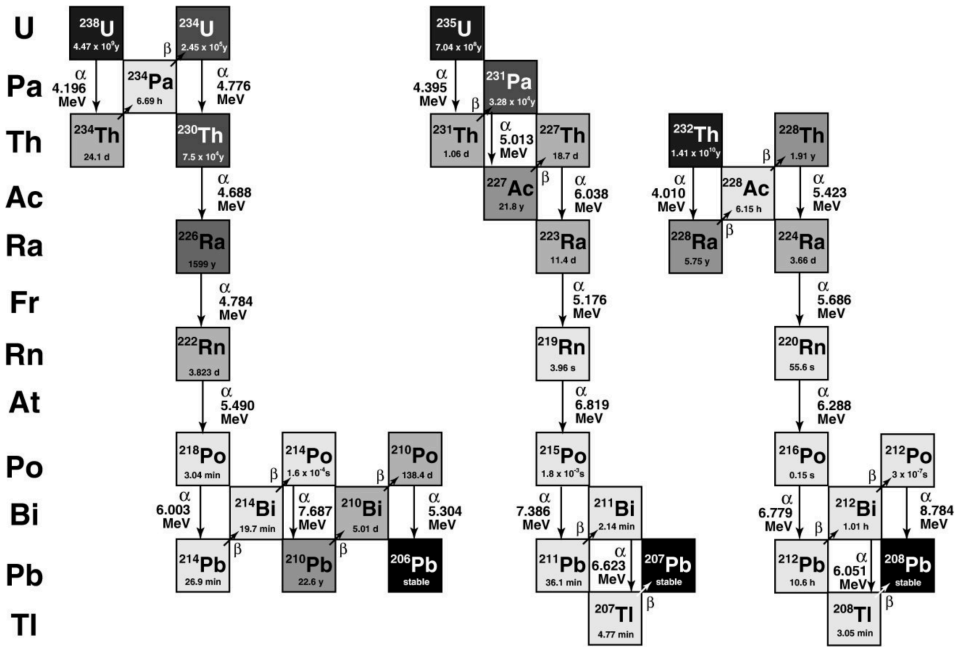

Figure 1.5 *The decay chains of the three parent nuclides ^{238}U, ^{235}U and ^{232}Th including their half-lives (Bourdon et al., 2003b).*

number of atoms of a certain nuclide that undergo decay per time unit (Bourdon et al., 2003b). The activity ratio equals 1 when the production rate is the same as the decay rate (Bourdon et al., 2003b). This state is referred to as secular equilibrium and the isotope ratios remain at unity. In a closed system, a state of secular equilibrium exists after about five half-lives of the longest-lived daughter isotope, in which the activities of all nuclides are the same (Bourdon et al., 2003b). During geological processes (e.g. phase change, partial melting or crystallisation), fractionation between the parent and daughter isotopes along a decay chain leads to a state of disequilibrium which is a non-steady state condition caused by natural processes in which the relative abundancies of the intermediate nuclides are no longer proportional to their decay constants (Bourdon et al., 2003b). The different half-lives of isotopes along the decay chains allow to determine processes at different geological timescales. The isotope ratios of ^{238}U-^{230}Th and ^{226}Ra-^{230}Th with half-lives of 75 ka for ^{230}Th and 1.6 ka for ^{226}Ra have half-lives comparable to the timescales of mantle melting and melt transport (Bourdon et al., 2003a). For examining fractionation processes like melting or fluid addition, the activity ratios are taken for identifying fractionation by their deviation from the secular equilibrium ($A_i = 1$) (Bourdon et al.,

2003a). To show the extent of radioactive equilibrium, an equiline diagram (Figure 1.6) is displayed in which the excess of one isotope over the other causes derivation from the equiline (Condomines et al., 2003).

Generally, the deep solid mantle has material residence times exceeding the half-lives of the commonly used daughter isotopes and shows therefore secular equilibrium throughout all decay chains prior to melting (Lundstrom, 2003b). In contrast, the process of melting is influenced mainly by two phases: a melt and the residual solid. These two phases differ in their viscosities and therefore in their relatively residence times with the magma ascending through the crust. This influences the U-series disequilibria by element partitioning in either the solid or melt phase and the respective flow rate of the phase (McKenzie, 1985). The ^{230}Th-^{238}U system is highly sensible to changes in the melting mineral assemblage allowing to constrain

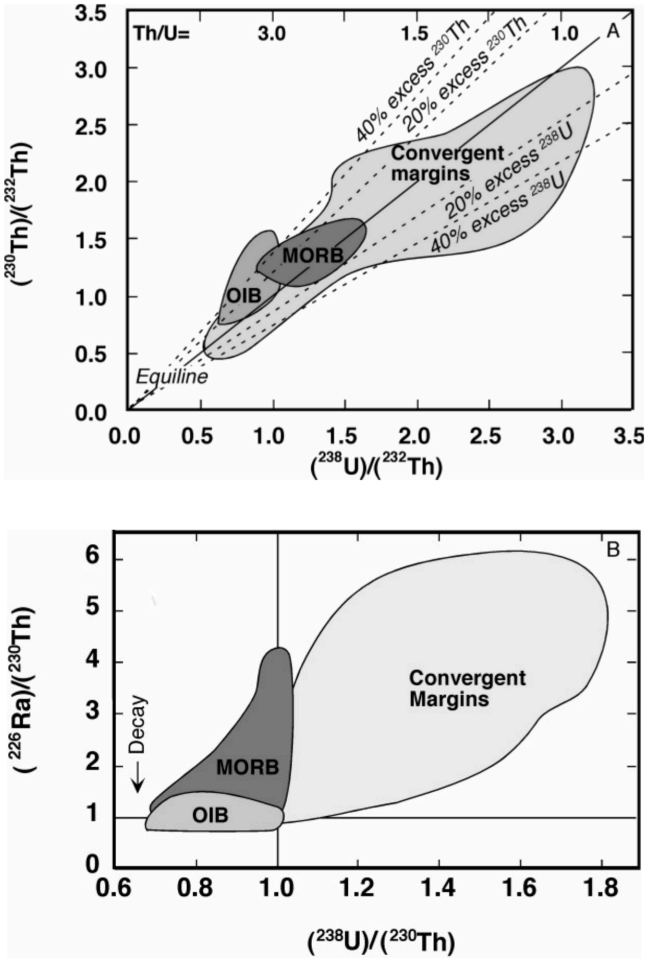

Figure 1.6 *Typical U-series disequilibria data differences along MORs, OIBs and convergent margins from Lundstrom (2003b) with a) (^{230}Th)/(^{232}Th) versus (^{238}U)/(^{232}Th) and calculated excesses in % and b) (^{226}Ra)/(^{230}Th) versus (^{238}U)/(^{230}Th) showing highest ^{226}Ra excesses along convergent margins. Lines display equilines where the samples are in secular equilibrium (=1), i.e. no excess of one isotope (or ratio) over the other exists.*

the depth of melting. Decompressional melting along MOR is commonly associated with ^{230}Th excesses (($^{238}U/^{230}Th$)<1) (Figure 1.6) due to melting at depths where residual garnet is present and Al-clinopyroxene are stable, and thus Th is more incompatible, leading to ^{230}Th excess in the melt especially due to ingrowth during dynamic melting (Blundy and Wood, 2003).

Under oxidizing circumstances like commonly observed in the arc environment (Arculus, 1994; Turner and Hawkesworth, 1997; Wood et al., 1990), U in its oxidation state U^{6+} is more fluid mobile than Th and will behave more incompatible even under normal adiabatic decompression melting. In subduction zones, the overlying mantle wedge is enriched in U derived from the down-going slab via fluids (Bourdon et al., 2003a; Turner et al., 2003a). This is commonly displayed by comparing the activity ratios of ^{238}U and ^{230}Th by plotting ($^{230}U/^{232}Th$) versus ($^{238}U/^{232}Th$) with the one to one equiline (Figure 1.6) showing the same activities for both isotope ratios (Lundstrom, 2003b). This results in ^{238}U excess (Figure 1.5) over ^{230}Th (i.e. ($^{238}U/^{230}Th$)>1) in arc lavas. Radium behaves similar to Ba and is also fluid mobile, but decays to secular equilibrium after 8 ka. Here, (^{226}Ra)/(^{230}Th) is plotted versus (^{238}U)/(^{230}Th) (Figure 1.6). Therefore, fluid-addition evident from ^{226}Ra excesses (Figure 1.6) over ^{230}Th must be quite recent when disequilibrium caused by seawater alteration can be excluded ($^{234}U/^{238}U$ = 1) (Turner et al., 2003a).

Using U-series for distinguishing decompressional from fluid fluxed melting, the impact of the arc and backarc spreading on the magma genesis in these systems can be deciphered.

2 METHODS AND DATA

2.1 PRE-EXISTING DATA, SAMPLE SELECTION AND SAMPLING

The Tonga-Kermadec island arc and Lau Basin backarc system has been studied extensively previously. Thus, a reference dataset (Appendix electronical datasheet) including published data from the northern Lau Spreading Centres southward to the VFR and from arc islands like Tafahi and Niuatoputapu located at the northern Tonga Arc southward to Clark volcano close to New Zealand was compiled. This dataset was used to provide a geochemical reference frame of the region and to discuss the new samples in their geochemical and geological context. This dataset was compiled from about 90 publications of the last 30 years and the data were arranged according to their sampling localities along the N-S extending Lau Basin spreading centres and filtered for data quality. Data quality was assessed by comparing the accuracy and reproducibility of available standard analyses. Exclusively data from peer-reviewed international publication were considered.

A data subset was compiled for each chapter depending on the specific topic: Chapter 4 focuses on the northern part of the Lau Basin and related arc volcanoes. Chapter 5 focuses on the southern Tonga region and the Uranium series isotope system in combination with new H_2O data. Here, the data subset includes all published Uranium series data from the region along with other geochemical data including major and trace element analyses of the same samples. Full references for the literature data are provided in the respective chapters.

2.1.1 Sampling of the NELSC (Chapter 3)

Samples of the NELSC, DR and the southernmost seamounts were collected during research cruise SO263 *TongaRift* with the German research vessel R/V *Sonne* in June 2018 (Haase et al., 2018). The cruise focused on sampling the northern Lau Basin aiming to further investigate the magmatic, hydrothermal and tectonic processes in this region focussing on the different

magmatic settings, namely the Niua and Niuatahi volcanoes, the DR and the NELSC. For the purpose of this work, the samples from the axis and off-axis of the NELSC, the seamounts located south of the NELSC and the DR, located between the reararc volcano Niuatahi and the NELSC, were analysed for geochemical purposes. The sampling of the DR, off-axis cones and southernmost seamounts was carried out by TV-guided grab from the GEOMAR Helmholtz-Zentrum für Ozeanforschung Kiel, that allowed sampling with a visual control. The Maka hydrothermal field located within the NELSC was sampled by the MARUM ROV QUEST 4000, a Remotely Operated Vehicle equipped with different tools for collecting samples from the seafloor. Most of the NELSC samples were collected by a wax corer. It is equipped with a heavy weight being lowered to the seafloor with the aim to hit the seafloor vertically to sample fresh volcanic glasses along ridge axes.

A total of 57 samples were analysed from the region along the NELSC and DR, six whole rocks and 51 fresh volcanic glasses. The samples were analysed for major and trace elements, Sr-Nd-Pb isotopes and water concentrations with the methods described below.

2.1.2 Sample selection of the VFR (Chapter 4)

There are several publications dealing with the large-scale magmatic evolution based on U-series along the N-S axes of the Lau Basin, but a small-scale E-W transect across the spreading axis has not been investigated in detail yet. Therefore, samples on an E-W transect across the VFR in proximity to the arc in the southern Kermadec region were chosen. The samples of the southern tip of the VFR were collected during the R/V *Sonne* cruises SO67 and SO167 in 1990 and 2002, respectively.

Seven samples along this transect were selected for new analyses of trace element (at Macquarie University), U-series and water analysis. Major element and Sr-Nd-Pb isotopic analyses of these samples were previously published by Fretzdorff et al. (2006) and Haase et al. (2009) (Appendix Table A7).

2.2 SAMPLE PREPARATION AND MACHINE SETTINGS

Here, the sample preparation for the different measurement methods undertaken by myself are presented in detail. Further details are given in the relevant chapters. Contribution and help provided by others in terms of introduction to the chemistry and machine handling is acknowledged in each chapter and in the acknowledgements.

2.2.1 Major element measurements

2.2.1.1 Electron microprobe analyses on volcanic glasses

Major element data were measured on fresh volcanic glasses using a JEOL JXA 8200 Superprobe electron microprobe (EMP) at the GeoZentrum Nordbayern (GZN), Friedrich-Alexander-Universität (FAU) Erlangen-Nürnberg. The handpicked glass chip samples were embedded into discs. Each disc had 18 pre-drilled holes and for each sample three to four glass chips were filled into one hole and before filling the holes with epoxy resin. After removing the dried discs from the metal plate, the disc bottoms were polished with different grain sized sandpapers and ¼ µm sized diamond paste on a velvet polishing plate until the glass chips were scratch-free. After cleaning the discs in isopropanol, they were coated with C and inserted into the machine. Standards used for element calibration were VG-A99 for Ti, Si, Al, Ca, Mg and Fe, VG-568 for K, Scapolite I for Na and Cl, chalcopyrite for S, rhodonite for Mn and fluorapatite for P (Beier et al., 2018). The instrument was operated using 15 kV, 15 nA with a beam diameter of 10 µm. For the glasses three individual analysis points were averaged for each sample.

2.2.1.2 Spectro XEPOS He X-ray fluorescence spectrometer on whole rocks

Major element data of whole rock samples were measured with a Spectro XEPOS He X-ray fluorescence (XRF) spectrometer at the GZN, FAU Erlangen-Nürnberg. For XRF sample preparation, the powdered samples were dried at 105°C. Then, 1 g of dried sample powder was homogenously mixed with 4.83 g of lithium tetraborate and 230 mg of di-iodpentoxide and

filled in platinum pots. The mixture was then fused to homogenous glass beads using an OXIFLUX burner with five flames of different temperature (450, 550, 650, 950 and 1050°C) and then rapidly cooled down by a cooling fan to generate a glass disc.

To determine the loss on ignition (LOI), 1.0006 (±0.0006) g of the dried sample powder was filled in a pre-heated porcelain pot and left in the oven for 12 h at 1050°C. The LOI was calculated by the weight difference due to degassing of volatiles like H_2O, organic C, Cl and F by the weight of the filled pot before and after the glow process.

Accuracy and precision (Appendix A3) of the measurements were determined by multiple measurements of international rock standards BE-N and GA (Haase et al., 2016).

2.2.2 Trace element measurements

2.2.2.1 Laser ablation ICP-MS on volcanic glasses at the GeoZentrum Nordbayern

Trace elements on volcanic glasses were measured the GZN, FAU Erlangen-Nürnberg by laser ablation inductively coupled plasma mass spectrometry (LA-ICP-MS) at using an Analyte Excite 193 nm laser (Teledyne Photon Machines) coupled to an Agilent 7500c ICP-MS at the GZN, FAU Erlangen-Nürnberg. As parameters of the ablation pattern, single spots were chosen with 20 Hz repetition rate and a 35 µm crater size in diameter. For the measurements, the cleaned electron microprobe discs were used taking the SiO_2 contents previously determined on the same samples as internal standards. External calibration was performed using the NIST SRM 612 glass standard. The international rock standard BCR-2G was measured to determine accuracy and reproducibility (Appendix A5). The trace element concentrations were calculated via GLITTER (Version 4.4.4, Online Interactive Data Reduction for LA-ICPMS, Macquarie Research Ltd.).

2.2.2.2 Laser ablation ICP-MS on volcanic glasses at the Macquarie University

Trace element concentrations on volcanic glasses were analysed using the LA-ICP-MS using an Agilent 7700× quadrupole ICP-MS coupled with a Photon Machines Excite Analyte 193 nm excimer laser ablation system with HelEx sample cell at Macquarie GeoAnalytical (MQGA), Macquarie University, Sydney. A laser beam of 65 µm spot size and a measurement time of 120s with a repetition rate of 5 Hz was used to analyse the volcanic glasses. NIST-610 glass standards were analysed to correct the machine drift. The NIST-610 standard was used for an external calibration of relative element sensitivities and ^{43}Ca data for internal calibration. For examining the accuracy and reproducibility (Appendix A5), the basaltic reference material BCR-2G was used. The trace element concentrations were calculated via GLITTER (Online Interactive Data Reduction for LA-ICPMS, Macquarie Research Ltd.).

2.2.2.3 Comparison of laser ablation ICP-MS on volcanic glasses

The comparability of the laser ablation ICP-MS data on the volcanic glasses over a range of time and at the different laboratories was guaranteed by comparing the accuracy from the international rock standard BCR-2G that was analysed at both locations (Appendix Table 5).

2.2.3 Isotope analyses

For isotope analyses, the volcanic glasses were handpicked under a binocular microscope and between 50 and 100 mg of each sample was weighed in a clean Teflon beaker. Before dissolution for Sr-Nd-Pb isotope analyses, the glass samples were leached in a solution mixed from 25% H_2O_2, 25% 2.5M HCl and 50% Milli-Q (MQ) H_2O for 10 min at room temperature. Afterwards, the samples were ultra-sonicated for 10 min at room temperature and rinsed with MQ water for at least four times. For sample dissolution, each sample was covered in 15 drops of 15M HNO_3 and 25 drops of 12M HF and the sealed beakers were left on the hotplate at 130°C for at least 48 hours. Afterwards, the samples were evaporated to near dryness before adding 20 drops of 15M HNO_3, evaporating the solution and redissolving in 30 drops of 6M

HCl. The samples were evaporated to complete dryness at 135°C and left on the hotplate for at least 1 hour in 30 drops of 1M HCl at ~80°C, and ultra-sonicated for 10 min. The samples were transferred into 2 ml centrifuge tubes and centrifuged for 10 min at 3000 rpm. All acids used for sample dissolution were double-distilled in Teflon.

2.2.3.1 Pb isotopes

To avoid contamination and ensure high quality, low blank measurements, only double-distilled reagents in dropper bottles were used. Lead columns were prepared from single-use 1 ml pipette-tips and a porous polypropylene frit and filled with 100 µl Eichrom Sr spec resin. The columns were cleaned with 2 reservoir volume (rv) loads of single distilled 6M HCl, 1 rv MQ, 2 rv double distilled 6M HCl and 1 rv 1M HCl. The centrifuged sample in 30 drops 1M HCl was added to the columns and directly collected in new Teflon beaker for Sr and REE, followed by washing the remaining Sr (not collected) through the resin by adding 15 drops of 1M HCl three times. The Pb was then collected by adding 4x20 drops of 6M HCl. The Pb beakers were cleaned with 6M HCl and rinsed with MQ. The samples were evaporated at 100°C and re-dissolved in 15 drops 1M HCl. The second Pb pass commenced with cleaning the columns with 2 rv MQ. After preconditioning the columns by adding 1 rv 1M HCl, the samples were added making sure to collect the complete sample by scratching the pipette tip carefully along the bottom of the beaker. In a next step, five times 15 drops of 1M HCl were added before collecting the Pb by adding four times 20 drops of 6M HCl. The Pb beakers were cleaned between the passes by adding single distilled 6M HCl before rinsing the beaker with MQ. The Pb samples were evaporated and treated with one drop of 15M HNO_3, immediately evaporating to dryness at 150°C to remove organics. Then 2 ml 2% HNO_3 was added and the sealed beaker left on the hotplate overnight. Typical blank for Pb for the entire procedure was 20-30 pg.

In a next step, the samples were prepared for machine measurement. Before spiking, the ^{208}Pb intensity in [V] of each sample was identified. The samples were analysed on a Thermo Fisher

Neptune multicollector (MC) ICP-MS in static mode at the GZN, FAU Erlangen-Nürnberg. Ten µl of the sample solution were diluted with 2% HNO_3 to 1 ml and analysed for ^{208}Pb intensity. Afterwards, the samples were diluted in 2% HNO_3 for an intensity of 5 to 8V (dependent on machine tuning) in a total volume of 4 ml. About 2 ml of the solution was added into a new vessel and spiked with about 12 µl double spike ($^{207}Pb/^{204}Pb$ = 0.8135) to get a $^{208}Pb/^{204}Pb$ ratio of ~1.

The spiked and unspiked sample sets were introduced into the MC-ICP-MS via a Cetac Aridus desolvating nebuliser. Potential interferences of ^{204}Hg were corrected by monitoring ^{202}Hg. The Pb isotope data were corrected for in-run mass fractionation related drift by normalising to the mean measured $^{208}Pb/^{206}Pb$ ratio using an exponential fractionation correction. In a final step, the spiked and unspiked measurements were combined offline by an exponential mass fractionation correction using the iterative method of Compston and Oversby (1969).

2.2.3.2 Sr-Nd isotopes

For Sr- and Nd columns, the Sr-cut derived from the first Pb-column step was introduced into several columns to separate Sr, REE and Nd. In a first step, columns prepared with 8 ml cationic resin (Biorad 50W-X8) and conditioned with 8 ml 1M HCl+0.1M HF. The samples were loaded into the columns in 2 ml 1M HCl+0.1M HF and washed with 6 ml 1M HCl+0.1M HF to remove Hf, Ti and Zr. In a next step, 26 ml of 2.5M HCl were washed through the columns to remove most major elements as well as Rb, and Sr was collected with another 12 ml 2.5M HCl. Then, 10 ml 2.5M HCl were added to the columns before adding 4 ml 6M HCl. The REE were then collected in 10 ml 6M HCl. For cleaning the resin, two times 20 ml 6M HCl followed by 20 ml MQ were added.

For separating Nd from the REE, 1.5 ml of Eichrom LN spec resin was used. The columns were ultra-sonicated for 10 min to homogenise the resin. After preconditioning the resin with 5 ml 0.25M HCl, the samples were loaded in 0.5 ml 0.25 HCl. The beakers were rinsed twice

with 0.5 ml 0.25M HCl which was added to the columns to guarantee that no sample was left in the beakers. Then, the columns were washed by adding 6 ml 0.25 HCl to remove La, Pr and most of the Ce, and Nd was collected by the addition of 12 ml 0.25M HCl. Before storing the columns after usage, they were cleaned with 3 rv 6M HCl and 1 rv MQ.

In a last step, Sr was separated from remaining Ca by using the Sr spec columns from the Pb separation. It was made sure, that each column was used for the same sample as in the Pb-method. Previously, the sample was dissolved in 0.5 ml 3.5M HNO_3 was put on the hotplate at ~100°C for 1 h. First, the resin was cleaned by 2 rv MQ and preconditioned by 1 rv 3.5M HNO_3. After loading the sample, the columns were washed by adding 1 rv of 3.5M HNO_3 twice. Afterwards, Sr was collected by 2 rv MQ.

Strontium and Nd were analysed using a ThermoFinnigan Triton® thermal ionization multicollector mass spectrometer (TIMS) in static mode at the GZN, FAU Erlangen-Nürnberg. For preparing the samples for the machine, the Sr samples were dissolved in 3 µl 1M H_3PO_4 and ultra-sonicated for 10 min. The samples were then loaded on Ta filaments by placing the outgassed filaments in the loading device and adding the sample solution on the filament centre. By carefully elevating the current to 1.5 A, the samples dried slowly and turned black. To evaporate the phosphoric acid, the current was turned up to ~2.3 A until the filament glowed red. Measured $^{87}Sr/^{86}Sr$ ratios were corrected for ^{87}Rb interference using the measured ^{85}Rb intensity and an $^{85}Rb/^{87}Rb$ value of 0.386. Instrumental mass fractionation was corrected assuming an $^{86}Sr/^{88}Sr$ ratio of 0.71194 (Romer et al., 2018).

The Nd samples were dissolved in 3 µl 0.1M H_3PO_4 and loaded onto double Ta filaments. The loading procedure is comparable to the Sr-loading but the current for fuming off the phosphoric acid had to be as low as the filaments did not glow. Correction for mass fractionation assumes a $^{146}Nd/^{144}Nd$ value of 0.7219 (Romer et al., 2018).

2.2.3.3 U-Th-Ra isotopes

Uranium-series isotopes were analysed on fresh, hand-picked unaltered volcanic glass samples which were first washed in MQ water five times for 10 minutes each and then leached in five steps to avoid seawater contamination. Following the leaching technique by K. Sims (personal communication), we ultra-sonicated the samples in distilled acetone, MQ water, 0.1M oxalic acid + 2% H_2O_2, 0.1M HCl + 2% H_2O_2, MQ water and distilled acetone and let the samples thoroughly dry before examining them under the binocular microscope again to check. Any samples that still showed little altered rims or filled bubbles were separated. In a next step, the samples were weighed and spiked at Macquarie University with 1 drop of ^{236}U-^{229}Th spike and 0.8 g of the ^{228}Ra spike. The sample-spike mixture was then dissolved in a mixture of ~1.5 to 2 ml concentrated HNO_3 and 2.5 ml concentrated HF and left on the hotplate at 180° overnight before drying it down at 130°C. In a next step, 6 ml 6M HCl saturated in boric salts was added and left at 120°C overnight. After drying this down, we covered the samples in 6M HCl and heated it up to 120°C for at least one hour to check if the samples became translucent, or if fluoric salts were left. To change the solution into loading acid, we added a few drops of concentrated HNO_3 before drying it down again and added 5 ml of 7N HNO_3, heating it up to 120°C for at least 2 h. If there were any residues left, the sample was re-digested again. After drying it down, a splash of concentrated HNO_3 was added again, dried down and the loading volume of 5 ml (for 0.2 g of sample) of 7M HNO_3 added and heated at 100°C overnight. As a last step, the samples were centrifuged for 5 min.

The U-Th columns were prepared with 4 ml AG1-x8 anionic resin which was washed in 4 ml MQ H_2O, 6 ml 7M HNO_3, 6 ml 6M HCl and 18 ml 0.2M HNO_3. After preconditioning the columns with 12 ml 7M HNO_3, the sample was added and collected and set aside for further processing to extract Ra. Sixteen ml 7M HNO_3 (for 0.2 g of sample) was added and also collected for Ra. The Ra cut was dried down. In a next step, 4 ml of 6M HCl was added, followed by another 4 ml of 6M HCl which was collected for Th and dried down. Uranium was collected by adding 7

ml 0.2M HNO_3 and dried down. The Th and U cuts were dissolved in 2 ml 2% HNO_3, put on a hotplate at 100°C for at least 1 hour ready for analysis.

To prepare the Ra cut for the following columns, the sample was covered with 6M HCl and dried down twice before adding 4 ml 2.5M HCl as loading volume. The first Ra column contains 8 ml AG50-Wx8 cationic resin which was cleaned with 8 ml 7M HNO_3, followed by 24 ml 6M HCl and 8 ml MQ water. To precondition, 6 ml 2.5M HCl are added twice. After loading the samples, the beakers were rinsed with 2 ml 2.5M HCl which was added to the columns after the samples went completely through. The columns were eluted with 28 ml of 2.5M HCl, 12 ml 2.5M HCl and 6 ml 3.75M HNO_3. Ra was collected after adding another 10 ml 3.75M HNO_3 and dried down. In a next step, this process was repeated with a smaller column. Covering the sample in 6M HCl and drying it down twice was followed by adding the loading volume of 0.5 ml 2.5M HCl. The columns were prepared with 0.5 ml AG50-Wx8 cationic resin which was washed with 2 ml 7M HNO_3, 2 ml 6M HCl and 2 ml MQ. For preconditioning, 1.5 ml 2.5M HCl was added before loading the sample. Again, the beaker was rinsed with 2.5M HCl (1 ml). The column was eluted with 2 ml + 2 ml + 1 ml 2.5M HCl before Ra was collected with 2 ml + 1 ml 3.75M HNO_3. After drying down the Ra cut, 100 µl 0.1M HNO_3 was added to the sample while the beaker was still warm. The next column was filled with 150 µl LN-spec resin which was washed in 500 µl 0.1M HNO_3 and preconditioned by repeating this step. After loading and re-collecting the sample in one step, 500 µl 0.1M HNO_3 were added and collected twice. The cut was dried down and 50 µl 3M HNO_3 were added, again when the beakers were still warm. The next column was prepared with 150 µl Sr-spec resin which was washed with 600 µl 0.5M HNO_3 and preconditioned by adding 600 µl 3M HNO_3. After loading the sample, it was eluted with 150 µl 3M HNO_3. In a last step, Ra was collected after adding 550 µl 3M HNO_3 which was dried down and ready for analysis.

The samples were analysed at the Macquarie GeoAnalytical facility (MQGA) at Macquarie University, Sydney, Australia. The U and Th cuts were analysed on a Nu Instruments® MC-

ICP-MS following the method described in Dosseto et al. (2006), Heyworth et al. (2007) and McGee et al. (2011). Separate methods were used to analyse U and Th (^{234}U and ^{236}U), and (^{229}Th and ^{230}Th) due to these low abundances requiring the central SEM detector which is situated behind an RPQ (energy) filter. For U analyses, the New Brunswick Laboratory (NBL) synthetic standards U010 and U005a were analysed at regular intervals to assess the robustness of instrumental corrections and to monitor drift. For Th analyses, a standard-sample bracketing procedure was used for each sample bracketing the sample with the Th 'U' standard solution and values checked independently with the Th'A' solution; a linear tail correction for the ^{232}Th tail on ^{230}Th was applied (Sims et al., 2008a).

The Ra cuts were analysed with a ThermoFinnigan Triton® TIMS at MQGA after being loaded onto degassed Re filaments using a Ta-HF-H_3PO_4 solution to activate the Ra. The filament loading process was like the one for Sr-Nd. Measurements of the ^{228}Ra/^{226}Ra ratios were analysed in the dynamic ion counting mode. To assess accuracy and precision of the whole procedure from weighing to analysis for U-Th-Ra isotopes the USGS rock standard BCR-2 was processed with the samples, and these data are presented in the Appendix and compared to the values in Scott et al., 2019. Typical blanks for U and Th are 100 and 50 pg, respectively, which are negligible compares to the amount of sample analysed.

2.2.4 Water measurements

Water measurements of the transect samples were undertaken at the Australian National University (ANU), Canberra, Australia on the sensitive high resolution ion microprobe – stable isotope (SHRIMP-SI). The handpicked glass chips were embedded in synthetic resin, polished and carefully removed from the resin by acetone and a hand-drill to embed the polished samples into aluminium holders in In (Appendix Figure A7). The mounts were coated with Au and analysed for $^{16}O^-$ and $^{16}O^1H^-$ with the method described in Turner et al. (2015) finding measurement spots avoiding cracks and inclusions in the glasses. Internal basaltic glass standards ND61, ND70 and 24.1 (Turner et al., 2015) were used to determine the

reproducibility and accuracy (Appendix A6). The sample water data were calculated by the sensitivity factor given by the standard analyses and the sample measurements.

3 MELTING AND MANTLE FLOW ALONG THE NORTH-EAST LAU SPREADING CENTRE

M.V. Schoenhofen[1, 2], C. Beier[1, 3], K.M. Haase[1], P.A. Brandl[4], R.H.W. Romer[1], M. Regelous[1], K. Rubin[5] and S. Turner[2]

[1]*GeoZentrum Nordbayern, Friedrich-Alexander-Universität (FAU) Erlangen-Nürnberg, Schlossgarten 5, 91054 Erlangen, Germany*

[2]*Department of Earth and Planetary Sciences, Macquarie University, Sydney NSW 2109, Australia;*

[3]*Department of Geosciences and Geography, University of Helsinki, PO Box 64, FIN-00014 Helsinki, Finland;*

[4]*GEOMAR Helmholtz Centre for Ocean Research Kiel, Wischhofstr. 1-3, 24148 Kiel, Germany;*

[5]*Hawaii Centre for Volcanology, Department of Geology and Geophysics, University of Hawaii, Honolulu, HI 96822, USA.*

3.1 ABSTRACT

The transport and melting of mantle material in the backarc spreading centres of subduction systems is a highly dynamic process that is not well understood. New major and trace elements and Sr, Nd and Pb isotope data combined with new H_2O data from the North-East Lau Spreading Centre (NELSC), the southernmost seamounts and the Diagonal Ridge (DR) yield new insights into the connection between the reararc and backarc in the tectonically highly active northern Lau Basin. Major and trace elements show that the southernmost seamounts are genetically connected to the NELSC and that the spreading continues towards the south. The radiogenic isotopes show that the NELSC is influenced by mixing of an enriched Samoa-like OIB derived by the plume further north and a depleted MORB endmember. An expected gradual decrease of the Samoa-like mantle source signatures towards the south is not evident from the new data. Varying degrees of enrichment along the NELSC show that the mantle source in the northeastern Lau Basin area is highly heterogeneous on a scale of few kilometres. The DR as the transition zone between the reararc and backarc has an OIB-like source signature derived from the subducted Louisville Seamount Chain (LSC) which was previously proposed to be restricted to the arcfront volcanoes Niuatoputapu and Tafahi. In spite of being formed in the vicinity of the DR, the enriched source signature is not detected along the NELSC. Thus, we can conclude, that there is no extensive exchange between the reararc and the backarc in this region.

3.2 INTRODUCTION

Lavas erupted at backarc spreading centres have variable compositions ranging from depleted mid-ocean ridge basalts (D-MORB) to backarc basin basalts (BABB) with enriched MORB (E-MORB) signature closer to the subduction zone (O'Neill, 2016). The chemical and isotopic compositions of BABBs reflect the composition of the mantle in the arc-backarc region and contributions from the igneous and sedimentary subducting slab including hydrous fluids and

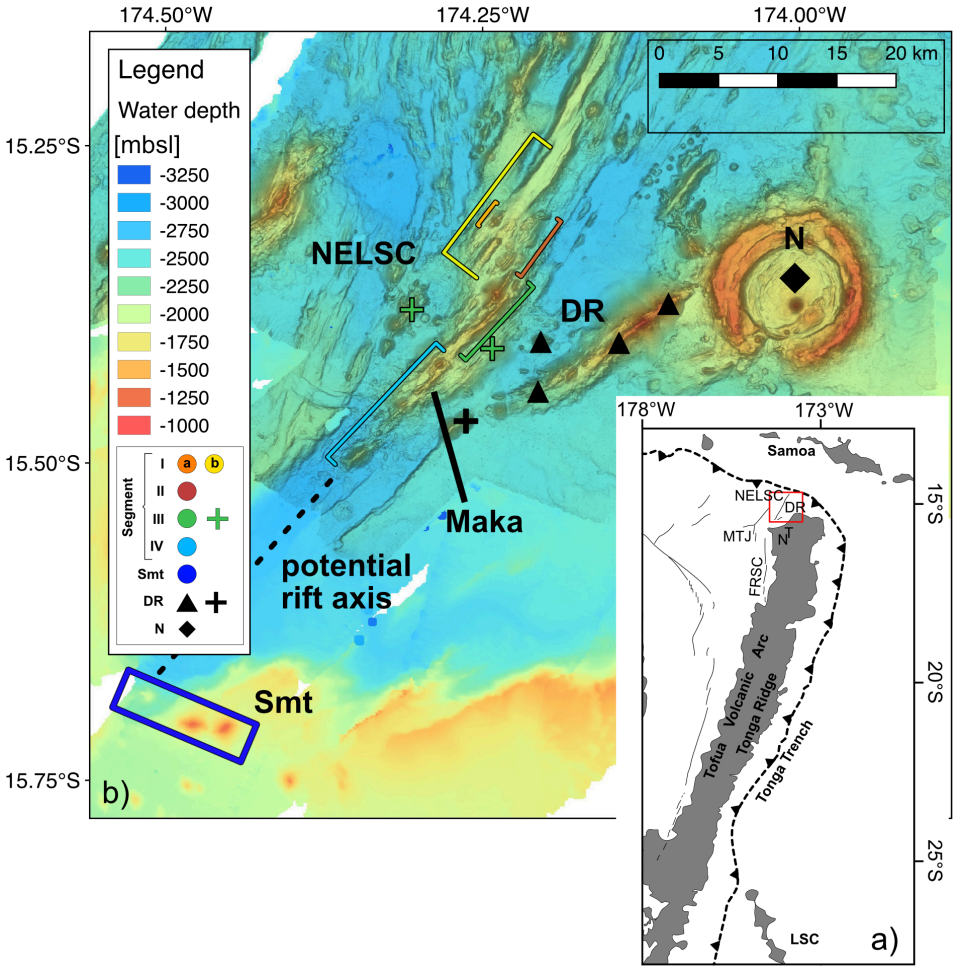

Figure 3.1 *Overview map of the working area showing a) the Tofua Volcanic Arc with Niuatoputapu (N) and Tafahi (T), the inactive Tonga Ridge following in the east and Lau basin with the location of the NELSC and the DR (in red), the Mangatolu Triple Junction (MTJ), the Fonualei Ridge Spreading Centre (FRSC) and the Louisville Seamount Chain (LSC) in the south and b) the sampling area from the SO263 cruise with the division of the NELSC into segments based on ocean floor morphology indicated by the coloured brackets. The NELSC samples are divided into five segments highlighted by different colours dependent on their location on the ridge segments. Crosses symbol off-axis, black triangles for DR sample locations, respectively. Niuatahi is marked with a black diamond used for literature data from this location in further figures. The assumed rift axis continuing towards the southern seamounts is highlighted by the dashed line.*

melts to varying degrees. Assimilation-fractional crystallisation (AFC) processes in the crust add additional complexity to the composition of the lavas (Kendrick et al., 2014; Pearce and Stern, 2006a). Generally, the degree of subduction zone influence in backarcs strongly depends on the proximity to the arc (Pearce and Stern, 2006a). The addition of unique subduction-related geochemical tracers to the melting regime underneath backarc spreading centres reflects the contribution of fluids, melts and mantle from the subducting slab to the

mantle wedge. The extent to which the melting regime of backarc spreading centres may be influenced by fluids ascending from the subducting slab several tens to hundreds of kilometres from the active island arc however, remains unsolved and may variably be explained by melting of remnant arc mantle exposed by slab rollback (e.g., Beier et al. (2017); Heuret and Lallemand (2005); Nakakuki and Mura (2013)), a heterogeneous mantle from complex reorganisation of the subduction zone geodynamics (e.g., Sinton et al. (2003), Beier et al. (2010)) or by overlapping of the melting zones between the arc and backarc introducing melts from the arc to the backarc spreading axis melting regime (e.g., Wei et al. (2015)).

The NELSC behind the northern Tongan arc and the associated Lau Basin reflect extensional stress causing the formation of several different spreading centres in a relatively small area (Figure 3.1). The extreme extension in the backarc causes abundant volcanism that allows to trace the different source components and mixing processes in the upper mantle. The NELSC has been mainly studied for the frequent hydrothermal activity in this region (Baker et al., 2019; Kim et al., 2009), and thus relatively little is known about the magma compositions and different processes influencing the melting regime in this region. The northern region of the NELSC along with the DR extending from the Niuatahi reararc volcano towards the spreading centre and the MTJ (Mangatolu Triple Junction) is situated sub-orthogonal to the active arc, i.e. distance above the slab increases with increasing distance from the arc (Hayes et al., 2012). This makes the area of the NELSC ideally suited to investigate the changing influence and impact of the subducting slab to the backarc melting regime. We propose that the DR represents the remnant connection between the reararc and the backarc and can therefore track the gradual compositional changes between these two settings.

Here, we present new major and trace element as well as Sr-Nd-Pb isotope compositions of fresh volcanic glasses and whole rocks from the NELSC area and the NE-SW striking DR located between Niuatahi and the NELSC, along with literature data from Niuatahi volcano, a large submarine reararc volcanic edifice, geochemically comparable to the arc, and the

Fonualei Ridge Spreading Centre (FRSC) and MTJ, both of which represent the backarc spreading volcanism. We focus on the processes influencing the magmas in this area by comparing the degree of subduction zone influence, mantle wedge depletion and partial melting at the different sites with respect to their geodynamic environment. Based on geochemical observations, we decipher the melt and fluid flow in this area to indicate the interaction between tectonic structures and melting underneath backarc spreading centres. We can show that the backarc melting regime shows no systematic changes with distance to the arc suggesting that the mantle heterogeneity is preserved even at higher spreading rates leading to higher degrees of melting in the northernmost Lau Basin.

3.3 GEOLOGICAL BACKGROUND

3.3.1 The northern Lau Basin

The Tonga-Kermadec subduction system is located in the SW Pacific north of New Zealand where the Pacific Plate is subducted underneath the Indo-Australian Plate. The active arc has a length of ~2800 km with the Tongan arc extending some 1200 km north of the intersection with the LSC at ~26°S. The subduction rate along the Tonga-Kermadec Arc increases from S to N from 164 mm/yr in the central Tongan arc up to 240 mm/yr (Bevis et al., 1995). Generally, few active volcanoes occur in the arc front of the northern Tonga region due to the spreading of the Fonualei Ridge in the Lau Basin capturing the slab flux leading to a volcanic shut down of the adjacent arc (Hawkins, 1995; Keller et al., 2008). The closest arc-related edifice in our working area is the large Niuatahi reararc-volcano (formerly Volcano O) that lies some 15 km east of the NELSC (Park et al., 2015). Niuatahi has a large caldera with 8 km diameter and is surrounded by ~640 km^2 of dacitic lava flows (Embley and Rubin, 2018).

The Lau Basin started opening 5.5 to 6 Ma due to the southward-directed movement of the LSC along the Tonga Arc (Hawkins, 1995; Ruellan et al., 2003). To the north the Lau Basin is bounded by the Fiji fracture zone and the Tonga Trench with a relatively shallow slab

subducting beneath the area due to plate flexure of the Pacific Plate at the northern end of the subduction zone (Hamburger et al., 1988; Millen and Hamburger, 1998). Complex tectonic processes resulted in the building of several spreading axes that exist in the northern Lau backarc basin. In this region, the NELSC represents the north-eastern extension of the FRSC and MTJ (previously King's Triple Junction; Figure 3.1a). The tectonic kinematics in the northern Lau Basin are dominated by arc-parallel extending forces induced by slab rollback in a SE direction and a strike-slip movement due to the asymmetric rollback along the northern edge of the basin towards the south (Anderson et al., 2020). The northern Lau Basin was first (>1 Ma) dominated by right-lateral shear stress where the spreading centres like the NELSC are directed (sub-)parallel to the maximum horizontal stress of the area in N and NNE arc-parallel directions (Anderson et al., 2020; Baxter et al., 2020). The NELSC is an irregular ridge between ~3.5 to 10 km broad (Anderson et al., 2020). The northernmost part of the ridge shows an elongated appearance with lava flows, becoming flatter and narrower in the central part and strongly segmented and more elevated in the southern part. Recent models imply spreading rates between decreasing from 42 mm/yr in the north to 30 mm/yr in the south of the NELSC (Baker et al., 2019; Sleeper et al., 2016). The southern tip of the NELSC propagates to the south into older crust where several seamounts are located ~20 km from the tip. Baxter et al. (2020) show that the crustal thickness of ~25 km in this part of the basin makes an exact localisation of the current rift tips difficult. Therefore, the seamounts are located just south of NELSC, in a region where the NELSC assemblage, two escarpments and large volcanic ridges of the FRSC converge (Anderson et al., 2020) and may display the initial southward movement of the spreading axis. This is supported by the fact, that continuing spreading is assumed to merge the NELSC and FRSC in the future (Baxter et al., 2020). Water depths of the study section of the NELSC range from 1259 meters below sea level (mbsl) at the southernmost seamounts up to 2280 mbsl at the southern part of the NELSC. In general, the NELSC ranges from 1400 to 1900 mbsl (Haase et al., 2018). The stress field around the NELSC is dominated by a right lateral strike slip zone to the west and an extensional zone to the east (Baxter et al.,

2020). The extension which is oblique to the hinge-rollback, favoured the opening of large volcanic ridges with normal faulting (Anderson et al., 2020). The DR is a ENE-trending ~20 km long and up to 7 km broad ridge reaching east from the southern part of the NELSC towards Niuatahi (Anderson et al., 2020). Water depths range from ~1400 to 2250 mbsl (Haase et al., 2018). More recently, the stress-field of the area re-oriented due to the collision with the Capricorn Seamount due to subduction (Anderson et al., 2020). This anticlockwise rotation caused spreading along a more northward directed axis close to the arc, e.g. along the FRSC and also enhances the spreading at both ends of the NELSC (Anderson et al., 2020).

The NE Lau Basin has long been known for the abundance of boninitic lavas, i.e. mafic rocks with relatively high MgO and low TiO_2 contents at intermediate SiO_2 (Le Bas, 2000), that were sampled in the forearc and reararc (Cooper et al., 2010; Falloon et al., 2007; Resing et al., 2011) but that also occur along the FRSC (Danyushevsky et al., 1995; Escrig et al., 2012). Previous work on the FRSC has shown a change of mantle source domains south of the MTJ (Figure 3.1) between relatively enriched signatures in the north and depleted, more arc-like magma compositions further south along the FRSC (Keller et al., 2008). Escrig et al. (2012) pointed out that many FRSC lavas have a boninitic signature which they explained to be a result of the combination of large subduction input, extreme mantle depletion and high degrees of partial melting. The boninitic magmas are suggested to have formed by melting of anomalously hot highly refractory plume mantle, possibly from Samoa, that was re-enriched by melts similar to OIB compisition and by slab fluids and melts (Danyushevsky et al., 1995; Falloon et al., 2007).

3.3.2 Hotspot Tracks influencing the northern Lau Basin

The Samoa hotspot track is located about 100 km north of the Tonga Trench parallel to the Lau Basin border (Price et al., 2014) and has been active for >100 Ma (Koppers et al., 2003). The Samoa plume shows low $^{3}He/^{4}He$ ratios and four different groups can be identified as the four mantle endmembers; HIMU (high $\mu=^{238}U/^{206}Pb$ along with high Pb isotopic ratios and low

Sr isotopic ratios), EM I (enriched mantle 1 with high Sr isotopic ratios, low Nd isotopic ratios and low Pb isotopic ratios), EM II (enriched mantle 2 with maximum Sr isotopic ratios and high Pb isotopic ratios) and DM (depleted mantle with highest Nd isotopic ratios and lowest Sr and Pb isotopic ratios) (Jackson et al., 2014). These four low He isotope endmembers ($R/R_a \leq 8$) are hosted in a high He matrix and mixing takes place leading to R/R_a (ratio to atmosphere)=20 - 33.8 observed in the Samoa lavas (Jackson et al., 2014). It is suggested, that a residue of the Samoa plume is located beneath the lithosphere of the hot spot track north of the Lau Basin (Price et al., 2017). The Samoa mantle material has been introduced to the northern Lau Basin by toroidal flow around the edge of the subducting slab for ~4 Ma (Price et al., 2016; Price et al., 2014; Price et al., 2017). The northern Lau Basin generally shows elevated upper mantle temperatures of ~1450 °C attributed to a combination of Samoan influence from the north and slab rollback (Wiens et al., 2006). The He isotopes of the lavas from the NELSC ($R/R_a=8.6$) as well as those from the MTJ ($R/R_a<8.0$) are typical for those in the upper mantle (Lupton et al., 2015; Tian et al., 2011). Thus, whereas high $^3He/^4He$ ratios $R/R_a>10$ in NW Lau Basin lavas indicate inflow of deep mantle plume material possibly from Samoa, He isotope ratios $R/R_a<9$ observed in the NE Lau Basin do not indicate this influence (Lupton et al., 2015).

The LSC is located on the Pacific Plate, ~4200 km long and consists of an age-progressive chain of seamounts and guyots with ages between 1.11 and 80 Ma (Beier et al., 2011). Today, the chain intersects the Tonga-Kermadec Arc at ~25.4°S whereas it started to be subducted beneath the northern Tonga Trench around 4 Ma along with the onset of the backarc opening at the northern Lau Basin (Ruellan et al., 2003; Timm et al., 2013; Turner et al., 1997). Influence of the LSC along the northern Tonga Arc at the volcanic islands Tafahi and Niuatoputapu has been proposed previously (Beier et al., 2017). Despite its present location 1000 km to the south, the geochemical signatures of the LSC can still be found in present day arc lavas. Beier et al. (2017) propose a reactivation of the component stored in the lithosphere by lithosphere thinning due to fast slab rollback at the northern part of the arc. The Louisville

component seen in the northern Tonga Arc is derived from subduction of the altered subducted basalts (Beier et al., 2017; Turner and Hawkesworth, 1997). Geochemically, the Louisville component is characterized by high Nb/Ta and high $^{206}Pb/^{204}Pb$ and highly negative Ce-anomalies showing high Ba/Th ratios (Beier et al., 2017).

3.4 SAMPLING AND METHODS

Here, we provide new geochemical data on new submarine samples from the NELSC and the associated DR that were recovered during R/V *Sonne* cruise SO263 TongaRift in July 2018 (Haase et al., 2018). The DR was sampled by TV-guided grab (TVG) from the GEOMAR Helmholtz Centre for Ocean Research Kiel (5 samples). Forty-seven samples from the NELSC including some from the Maka hydrothermal field (Haase et al., 2018) were taken by wax-corer and ROV MARUM QUEST. Several off-axis seamounts and three volcanoes at the southern tip of the NELSC were also sampled using the TVG (Figure 3.1). We analysed 57 samples from the vicinity of the NELSC, 6 of which are whole rocks from the southernmost seamounts (Figure 3.1) and the remaining samples are fresh volcanic glasses (n=51). Based on the bathymetry and the segmentation, we divided the sampled southern part of the NELSC into distinct volcanic ridges forming individual overlapping segments (Fig. 3.1). Segment Ia is a single cone separated from Segment Ib based on both bathymetry and geochemistry. The off-axis samples are shown with different symbols (crosses) but colour-coding is done depending to their segment affiliation.

Major element data (Appendix A1) were measured on fresh volcanic glasses using a JEOL JXA 8200 Superprobe electron microprobe at the GeoZentrum Nordbayern (GZN), Friedrich-Alexander- Universität (FAU) Erlangen-Nürnberg. Multiple individual points on each glass sample on up to four glass chips were measured and the data was averaged. The instrument was operated using 15 kV, 15 nA with a beam diameter of 10 µm. Further information is

provided in Chapter 2.2 of this thesis and in Brandl et al. (2012) and Freund et al. (2013), standards are available in Beier et al. (2018) and the Appendix A4 of this thesis.

Major element data of whole rock samples from the southernmost seamounts were measured with a Spectro XEPOS He X-ray fluorescence spectrometer at the GZN, FAU Erlangen-Nürnberg using the method described in Freund et al. (2013). Accuracy and precision of the measurements were determined by multiple measurements of international rock standards BE-N and GA. The accuracy is generally better than 3% (BE-N) and 6% (GA) and for P_2O_5 better than 15% and 30% (Appendix A4). The precision is better than 1.7% and 1%, respectively. The Cl/K ratios of the glasses range from 0.13 to 0.37 indicating that assimilation of seawater altered wall rocks did not affect the samples except for one sample (111TVG-08) which has an elevated ratio of 1.44 indicating seawater alteration. Whole rock samples from the NELSC have a loss of ignition (LOI) of <0.03 wt.% (Appendix A1), but DR samples show elevated values of 0.66 up to 5.22 wt.% indicating seawater alteration (Appendix A1).

Trace elements on the volcanic glasses were measured by laser ablation ICP-MS at the GZN using an Analyte Excite 193 nm laser (Teledyne Photon Machines) coupled to an Agilent 7500c ICP-MS at the GZN, FAU Erlangen-Nürnberg (Woelki et al., 2019). Repeated analyses of the basaltic rock standard BCR-2G (n = 3) yield an accuracy of <10 % for all elements (except Li < 14.33 % and Zn < 35 %) and a reproducibility of <6 % for all elements (except for As, Yb < 7 %; Li, Ag, Ta, Bi < 12%). For further information also see Appendix A5.

Selected samples from the different settings were leached and processed based on the methods described in Romer et al. (2018) and Romer et al. (2019) and measured for their Sr-Nd-Pb isotope ratios at the GZN, FAU Erlangen-Nürnberg. The Sr and Nd isotope compositions were analysed using a Thermo Fisher Triton thermal ionization mass spectrometer (TIMS) in static mode and double spiked Pb isotopes using a Thermo Fisher Neptune multicollector ICP MS in static mode. Strontium isotope measurements were

corrected for mass fractionation with $^{88}Sr/^{86}Sr = 0.1194$ with mass 85 to correct the contribution of ^{87}Rb to ^{87}Sr. Neodymium isotope data were corrected for mass fractionation using $^{146}Nd/^{144}Nd = 0.7219$. The standard NBS987 measurements (n=3) show $^{87}Sr/^{86}Sr = 0.710270 \pm 0.000005$ (2σ), and the Erlangen Nd standard (n=4) gave $^{143}Nd/^{144}Nd = 0.511541 \pm 0.000007$ (2σ). The Nd isotope ratios correspond to a value of 0.511850 for the La Jolla Nd isotope standard. The Sr isotope compositions of the samples were corrected to the NBS987 = 0.710250. Lead isotope measurements were corrected using a long-term NBS981 $^{206}Pb/^{204}Pb$, $^{207}Pb/^{204}Pb$ and $^{208}Pb/^{204}Pb$ standard measurements of 16.9410, 15.4993 and 36.7244, respectively. Lead blanks are <40 pg. For further information see Appendix A7.

Water data were analysed for selected glass samples at the Australian National University (ANU), Canberra, Australia on the sensitive high resolution ion microprobe – stable isotope (SHRIMP-SI). The handpicked glass chips were analysed for $^{16}O^-$ and $^{16}O^1H^-$ together with internal basaltic glass standards ND61, ND70 and 24.1 (Turner et al., 2015) to determine the reproducibility and accuracy (see Appendix A6).

3.5 RESULTS

3.5.1 Petrographic description of the samples

The NELSC was sampled by wax corer where 21 fresh unaltered glass samples were recovered from the ridge axis. These glasses are black, unaltered chips and in samples SO263 108VSR-01 and SO263 109VSR-01 the glass chips were surrounded by (pumiceous) sediment. The whole rocks appear basaltic, e.g., SO263 117TVG-01 has abundant <2 mm plagioclase and olivine and <4 mm clinopyroxene. The <5 mm vesicles are rounded and regularly distributed (<30%) in the matrix and glass crust. The two samples from SO263 120TVG are fresh, angular basaltic lava vesicle-bearing pieces with smaller (<1 mm) plagioclase and clinopyroxene.

From the off-axis sample locations (~1.6 to 4.7 km distant from the NELSC), a brownish-black sediment-appearing sample consisting of small glass chips (SO263 119TVG-01) and a <50% vesicle bearing fresh, angular basalt with a MnOOH-coated glassy crust (SO263 118TVG-01) were recovered (Haase et al., 2018).

The basaltic whole rocks from the five southernmost seamounts are porphyritic with up to 60% vesicularity. Plagioclase (<2 mm) and clinopyroxene are common (<4 mm), whereas olivine crystals are rare except for one picritic sample (SO263 124TVG-03). Two basalt samples have glass rims thick enough for geochemical analysis (Haase et al., 2018).

The whole rock samples from the DR show a large variety of alteration from highly altered with MnOOH or FeOOH coating to fresh and angular pieces of lava. Most samples show a fine, grey to black groundmass with up to 5% plagioclase (0.1 to 3 mm) and clinopyroxenes (<2 mm). The sample SO263 111TVG-06 also shows ~2% olivine crystals (<2 mm). Vesicle contents in the whole rocks range up to ~30%. Two dacitic pumices analysed for this thesis, vary in their vesicularity. One is quite dense with <30% of <4cm sized vesicles (SO263 114TVG-01) while the other shows up to 60% vesicles and clinopyroxene crystals <2 mm (SO263 112TVG-01). Both contain some <3 mm sized plagioclase (<3%).

3.5.2 Geochemical compositions

The samples are grouped based on the NELSC Segments defined in the bathymetric map (Fig. 3.1). The general trend of the samples reaches from basaltic to rhyolitic samples (Fig. 3.2a) with the NELSC displaying a relatively small range from basalts to basaltic-andesites. The southernmost seamounts are basaltic in composition. In contrast, the DR shows large differences throughout the whole compositional range. Generally, the rhyolitic samples are pumices, while the dacites are lava blocks with glass available. All ranges for the segments, seamounts and the DR are presented in Table 3.1. Samples from the NELSC range from 3.8

to 7.9 wt.% MgO (Figure 3.2; Table 3.1) and all NELSC samples broadly display comparable trends in their major elements. The lavas of the three seamounts further south lie at the most

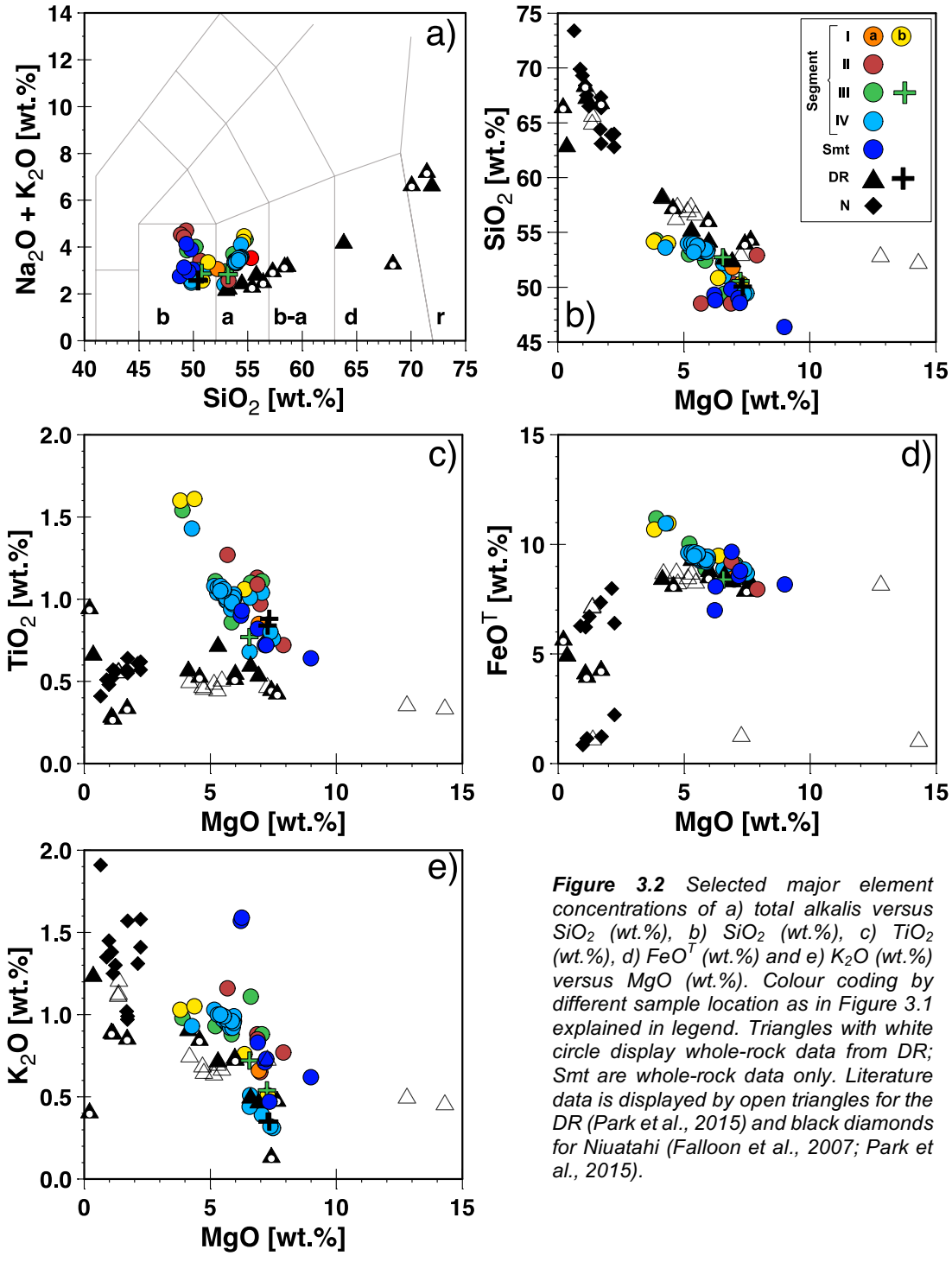

Figure 3.2 *Selected major element concentrations of a) total alkalis versus SiO_2 (wt.%), b) SiO_2 (wt.%), c) TiO_2 (wt.%), d) FeO^T (wt.%) and e) K_2O (wt.%) versus MgO (wt.%). Colour coding by different sample location as in Figure 3.1 explained in legend. Triangles with white circle display whole-rock data from DR; Smt are whole-rock data only. Literature data is displayed by open triangles for the DR (Park et al., 2015) and black diamonds for Niuatahi (Falloon et al., 2007; Park et al., 2015).*

and K_2O contents increase with decreasing MgO in the NELSC and seamount samples. The least evolved NELSC basalts with 8 wt.% MgO contains ~0.7 wt.% TiO_2 (Figure 3.2c) whereas K_2O in the primitive NELSC basalts ranges from 0.3 to 0.8 wt.% (Figure 3.2e). The highest K_2O contents and K_2O/TiO_2 ratios occur in Segments II and III samples and some from the seamounts whereas lavas from Segments I and IV generally have lower K_2O and K_2O/TiO_2 at a given MgO (Figures 3.2). The most primitive DR rocks have SiO_2 contents >52 wt.%, with the off-axis samples belonging to the DR reaching down to ~50 wt.% SiO_2 (Figure 3.2b) and all DR samples have TiO_2 concentrations below 1.0 wt.% and lie on a trend of constant TiO_2 with MgO (Figure 3.2c). The mafic samples have similar FeO^T compared to those of the NELSC but the more evolved DR rocks lie on a decreasing FeO^T trend with decreasing MgO (Figure 3.2d). The K_2O contents of the DR lavas overlap with the NELSC samples but are relatively low compared to the lavas from the axis (Figure 3.2e). The K_2O/TiO_2 ratios of the DR samples are generally higher than those of the NELSC lavas reflecting the low TiO_2.

The N-MORB normalised trace element abundances (Gale et al., 2013) of the different lavas show significant differences (Figure 3.3). The majority of the segments show a negative Nb-Ta trough relative to the other incompatible elements. Most Segment II and some Segment III samples do not show this negative Nb-Ta anomaly but are highly enriched in high large ion lithophile elements (LILE) comparable to the OIB components of Samoa and LSC. Lavas from the other segments as well as those from the seamounts and DR show strong enrichments of

	SI	SII	SIII	SIV	Smt	DR
(wt. %)						
MgO	3.81-7.28	5.68-7.90	3.90-7.25	4.27-7.49	6.21-8.99	0.22-7.65
SiO_2	50.3-54.2	48.5-52.9	48.7-54.3	49.4-54.0	46.4-49.8	50.0-68.4
TiO_2	0.74-1.61	0.72-1.27	0.77-1.54	0.68-1.43	0.64-0.93	0.28-0.94
FeO*	8.44-10.97	7.95-9.38	8.39-12.0	8.68-11.0	6.99-9.66	3.99-9.41
Na_2O	2.03-3.40	1.79-3.52	2.06-3.31	1.94-3.14	2.01-2.50	1.71-5.93
K_2O	0.51-1.05	0.65-1.16	0.54-1.11	0.31-1.03	0.47-1.59	0.14-1.24

Table 3.1 *Ranges of major element composition of each NELSC segment (I-IV), the southern seamounts (Smt) and the DR.*

fluid-mobile elements such as K, Pb, Sr, and U relative to the other highly incompatible, immobile elements (e.g., Nb or La).

The basalts from Segments I and II have the highest $(La/Sm)_N$ whereas the Segment III lavas are more variable ranging from 1.0 to 4.2 (Figure 3.4a). The seamount samples as well as the off-axis lavas lie between 1 and 2 in $(La/Sm)_N$. In a plot of $(La/Sm)_N$ versus Ce/Pb (Figure 3.4a)

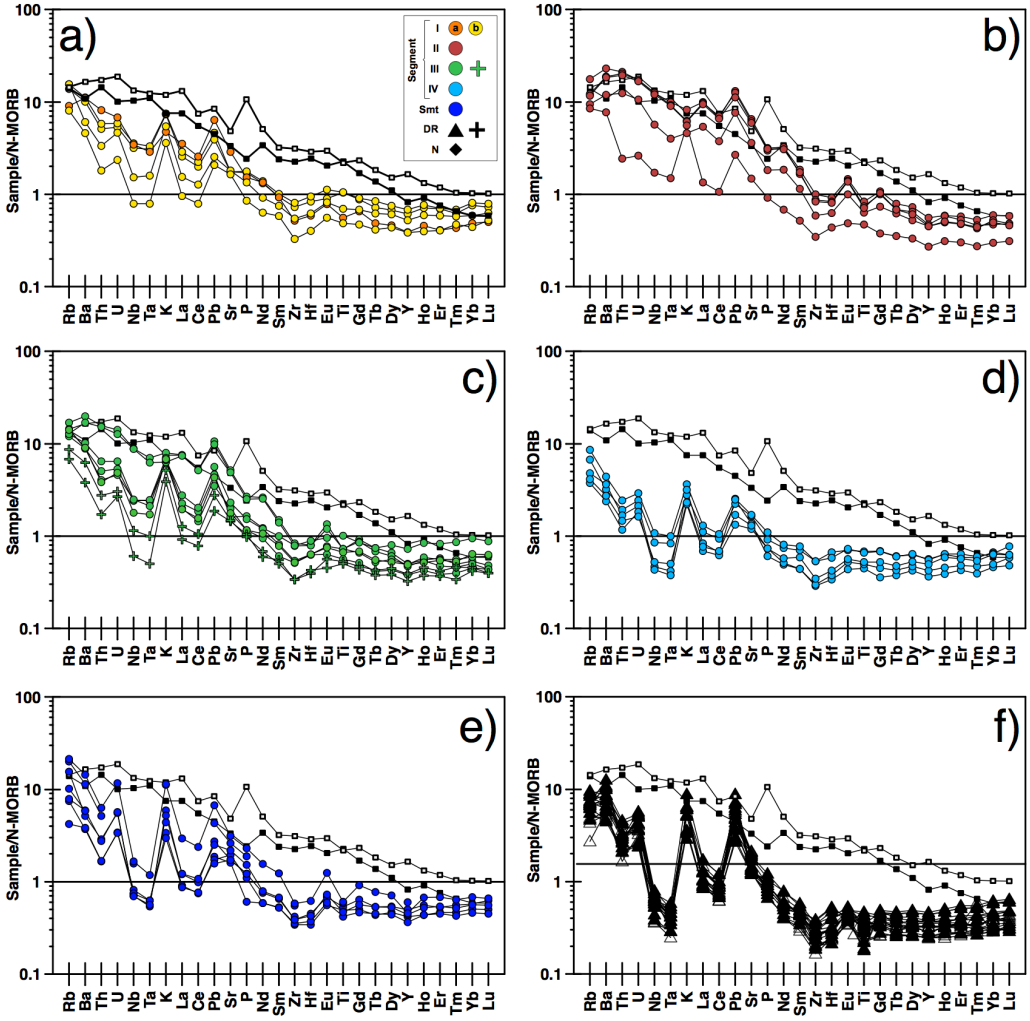

Figure 3.3 *Normal mid-ocean ridge basalt (N-MORB) normalised (Gale et al., 3013) incompatible element patterns for the different sample locations and NELSC segments of the new samples from the NELSC indicating large similarities between the different locations except along Segment I to III. Colour coding like in Figure 2. Literature data is displayed by blank triangles for the DR (Park et al., 2015). Samoa average (black squares) for comparison with data from (Hart and Jackson, 2014; Horan et al., 2018; Jackson et al., 2014; Jackson and Carlson, 2012; Jackson and Hart, 2006; Jackson et al., 2010; Jackson et al., 2007a; Jackson et al., 2008; Jackson et al., 2007b; Jackson and Shirey, 2011; Kendrick et al., 2015; König et al., 2011; Konter and Jackson, 2012; Konter et al., 2016; McDougall, 2010; Price et al., 2014; Reinhard et al., 2019; Salters et al., 2011; Sims et al., 2008b; Workman et al., 2004; Workman et al., 2006) and LSC average (blank squares) by Beier et al. (2011).*

NELSC lavas display a large range in $(La/Sm)_N$ but have relatively homogenous Ce/Pb ratios. Lavas from the DR and from the northern part of the NELSC extend to higher Ce/Pb at relatively constant $(La/Sm)_N$. The high $(La/Sm)_N$ samples are all from the NELSC with Segments IV and V and off-axis samples display the lowest ratios. A negative correlation of Ba/Nb with Nb/La (Figure 3.4b) is observed, with the highest Ba/Nb ratios from the DR and Niuatahi volcanos trending towards the lowest ratios at Segment II. Niobium/Ta ratios (Figure 3.4c) vary from 14. 5 to 21.5 with the highest ratios at Segment II and III, while the new DR samples range from 17.2 up to 35.7. Niuatahi literature samples (Falloon et al., 2007; Park et al., 2015) display a range between 13.7 and 20.7. Barium/Th shows a large variation along the NELSC from 72.3 to 246.06 with the Segment II samples defining both the lowest and highest values (Figure 3.4). The new DR data generally range between 155 and 361 while the literature data (Falloon et al., 2014; Park et al., 2015) range from 181 to 190 with one outlier at 271 for the DR and from 154 to 197 at Niuatahi. Niobium/Yb (Figure 3.4d, f) ratios vary from ~1 to 5 at most segments while some samples from Segments I-III range from 5 to 30. All DR and Niuatahi samples have ratios <5. Barium/La versus La/Yb shows a bimodal distribution with the highest Ba/La and lowest La/Yb at the DR and the highest ratios at Segment II (Figure 3.4e). Most samples are situated between these extremes with Ba/La 10-30 and La/Yb <6. Ce/Ce* (Figure 3.5a) The Ce/Ce* displays ratios >1 for the NELSC samples and <1 for most Niuatahi and DR samples (Figure 5).

3.5.3 Radiogenic isotope compositions

Strontium and Nd isotope compositions (Figure 3.6a) along the NELSC range from 0.70318 to 0.70406 and 0.51275 to 0.51230, respectively. Off-axis lavas and the southernmost seamount samples lie within this range, while DR samples are displaced to higher Sr isotope ratios at a given Nd isotope ratio of ~0.5129, respectively. Lead isotopes have $^{206}Pb/^{204}Pb$ isotope ratios

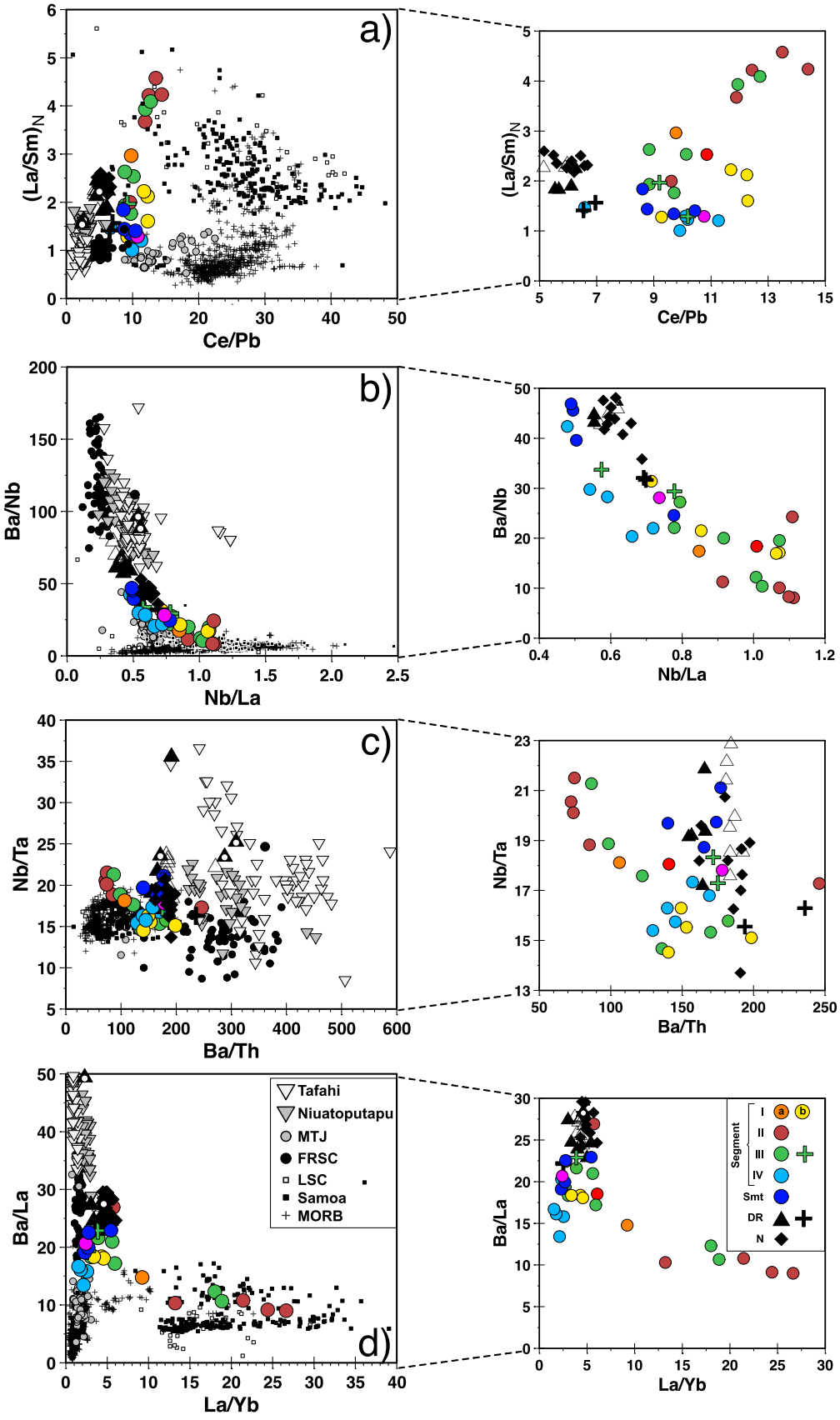
a)
(La/Sm)N
Ce/Pb
b)
Ba/Nb
Nb/La
c)
Nb/Ta
Ba/Th
d)
Ba/La
La/Yb
Tafahi
Niuatoputapu
MTJ
FRSC
LSC
Samoa
MORB
Segment
I
II
III
IV
Smt
DR
N

Figure 3.4

Figure 3.4 (continued) *Selected trace element variations of the NELSC area including selected data from proximal backarc and arc edifices with a) $(La/Sm)_N$ versus Ce/Pb, b) Ba/Nb versus Nb/La, c) Nb/Ta versus Ba/Th, and d) Ba/La versus La/Yb. Colour coding by different sample location as in Figure 3.2. For better overview, detailed plots of the NELSC area only at the right. Niuatahi and DR data from Falloon et al. (2007) and Park et al. (2015). References for literature data as follow: FSC (Caulfield et al., 2012; Dale et al., 2012; Danyushevsky et al., 1993; Dril et al., 1997; Escrig et al., 2012; Falloon et al., 1992; Falloon et al., 2007; Hahm et al., 2012; Honda et al., 1993; Keller et al., 2008; Kent et al., 2002; Layne et al., 2009; Pearce et al., 2007; Tian et al., 2011), MTJ (Dale et al., 2012; Escrig et al., 2012; Keller et al., 2008); Niuatoputapu: (Bourdon et al., 1999; Ewart et al., 1977; Ewart et al., 1998; Ewart and Hawkesworth, 1987; Turner et al., 2000; Turner and Hawkesworth, 1997; Wendt et al., 1997); Tafahi (Ewart et al., 1977; Ewart et al., 1994a; Ewart et al., 1998; Ewart and Hawkesworth, 1987; Pearce et al., 2007; Regelous et al., 1997; Stolz et al., 1996; Turner et al., 2000; Turner and Foden, 2001; Turner and Hawkesworth, 1997; Wendt et al., 1997); MORB (Jenner and O'Neill, 2012); LSC, Niuatoputapu and Tafahi data are from Beier et al. (2011) and Beier et al. (2017).*

from 18.68 to 19.22 (Figure 3.6), $^{207}Pb/^{204}Pb$ from 15.62 to 15.63 (Figure 3.6d) and $^{208}Pb/^{204}Pb$ from 38.54 to 39.18 (Figure 3.6e). DR data have the highest $^{206}Pb/^{204}Pb$ ratios but comparablylower $^{207}Pb/^{204}Pb$ and $^{208}Pb/^{204}Pb$. In Ce/Pb versus $^{206}Pb/^{204}Pb$ lavas from DR (Figure 3.4a, 3.7b) display a large variability in Ce/Pb but relatively constant $^{206}Pb/^{204}Pb$ of ~19.4 whereas NELSC lavas plot close to the range of oceanic intraplate lavas from Samoa with relatively low Ce/Pb at variable $^{206}Pb/^{204}Pb$. The NELSC samples display a negative correlation of $^{143}Nd/^{144}Nd$ versus Th/Nd (Figure 7a), DR samples have relatively constant Nd isotope ratios and Th/Nd ratios deviating to higher Th/Nd than the NESLC samples.

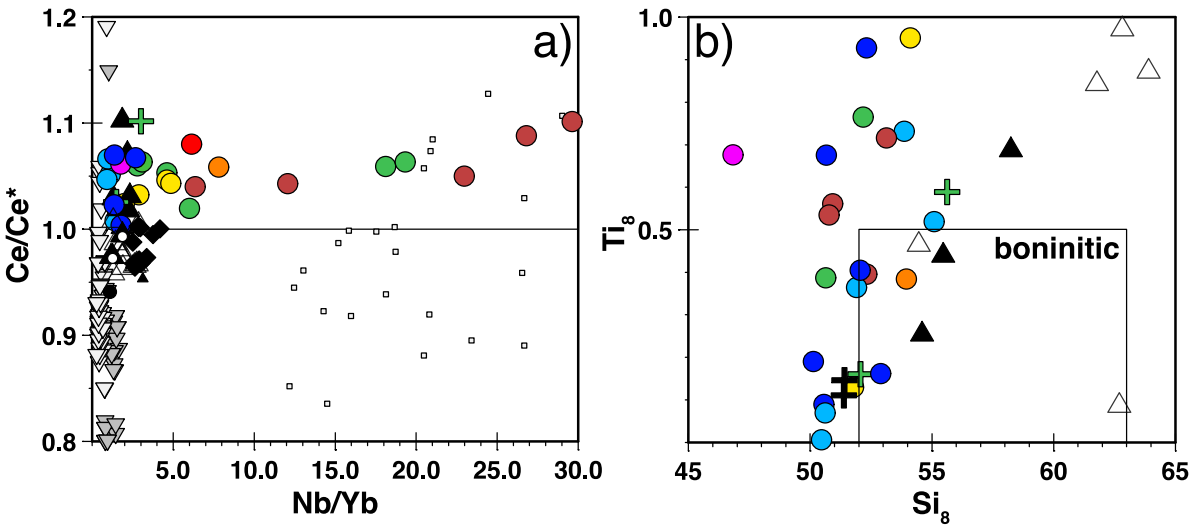

Figure 3.5 *Trace element plots of a) Ce/Ce* versus Nb/Yb showing positive and negative Ce-anomalies (unequal 1) from the NELSC area along with Tafahi, Niuatoputapu and the LSC (Beier et al. (2011) and Beier et al. (2017)) and b) differentiation-corrected TiO_2 and SiO_2 for 8 wt.% MgO showing boninitic affinities of samples with MgO >4 wt.% in the NELSC area after the boninitic discrimination diagram by Pearce and Reagan (2019). Colour coding by different sample location as in Figure 3.2.*

3.5.4 Water compositions

Water data (Figure 8) display a small range from 1.11 (±0.03) to 1.48 (±0.02) wt.% H_2O along the NELSC including the southernmost seamounts. One off-axis sample is slightly lower with 0.96 wt.% H_2O but the 2σ error of 1.26 is too large to take it into account for the average range. In contrast, one basaltic-andesitic DR sample (SO263 112TVG-03) displays 0.6 (±0.15) wt.% H_2O (Appendix A1).

3.6 DISCUSSION

Previous studies have concluded that numerous enriched and depleted components influence the magma compositions in the northern Lau Basin (Falloon et al., 2007; Price et al., 2016) the exact spatial distribution of which remains sparsely investigated and is the focus of this work.

The mantle in the Lau Basin consists of two domains: the Pacific mantle dominated prior to the initiation of backarc spreading due to slab rollback and the Indian mantle influencing magmas after initiation of spreading (Hergt and Woodhead, 2007). The present-day composition of the mantle underneath the Tongan arc has Indian MORB isotopic signatures but enriched Samoan plume mantle flows into the Lau Basin from the north adding a significant contribution of enriched mantle (Falloon et al., 2007; Pearce et al., 2007; Price et al., 2016). The peculiar OIB-type Nb-enrichment in many lavas from the NE Lau Basin has been suggested to reflect contribution from Samoan plume mantle (Falloon et al., 2007). Alternatively, subducted and reactivated oceanic intraplate material from the LSC may influence the magmas of the northern Tongan islands of Niuatoputapu and Tafahi (Beier et al., 2017; Turner and Hawkesworth, 1998) also causing an enrichment of Nb and Ta. The radiogenic isotope and incompatible element ratios of our samples indicate three distinct endmembers that are required to explain the observed mixing trends in all samples discussed here, the origin of which we will discuss in more detail below (Figures 3.6).

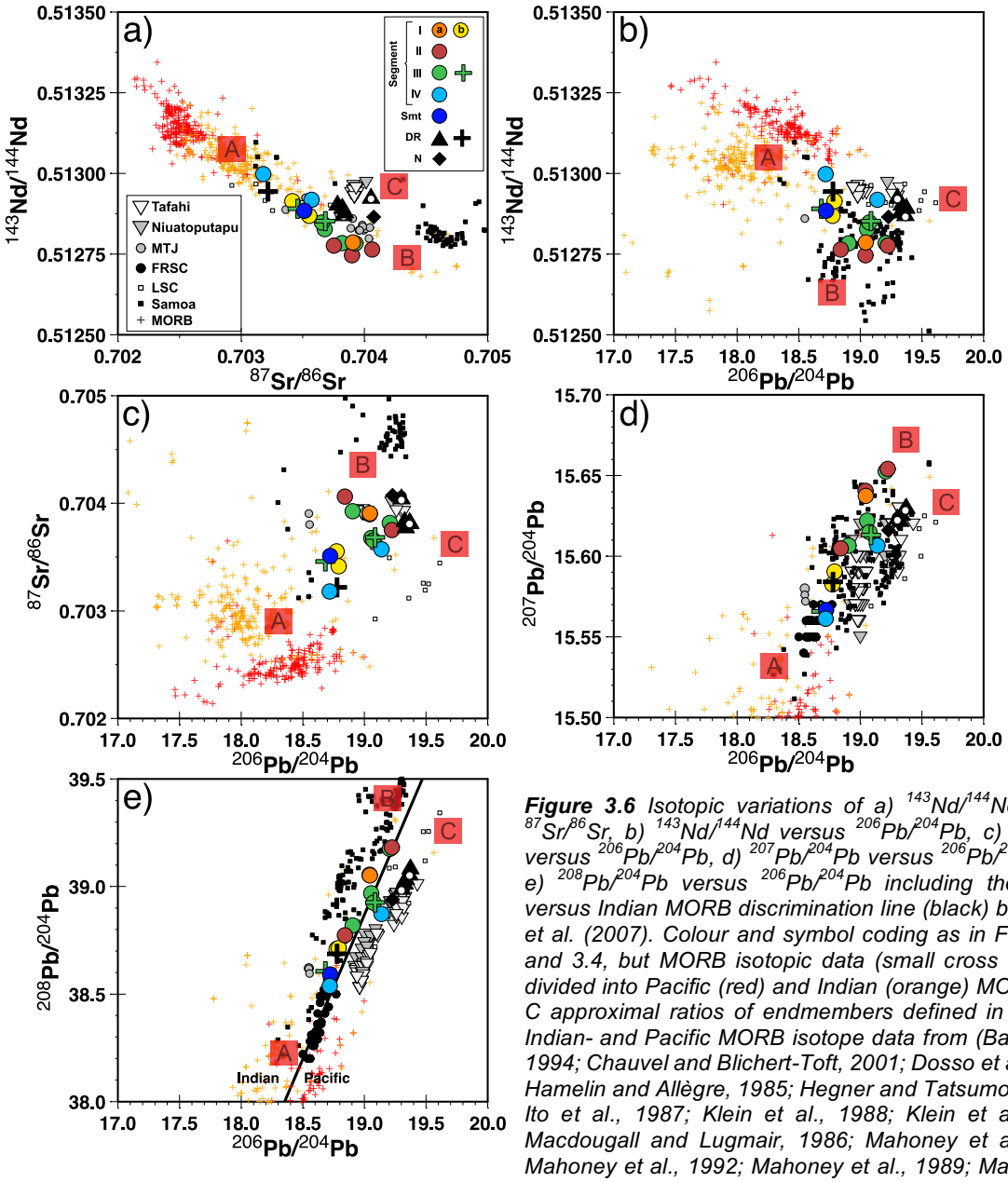

Figure 3.6 *Isotopic variations of a) $^{143}Nd/^{144}Nd$ versus $^{87}Sr/^{86}Sr$, b) $^{143}Nd/^{144}Nd$ versus $^{206}Pb/^{204}Pb$, c) $^{87}Sr/^{86}Sr$ versus $^{206}Pb/^{204}Pb$, d) $^{207}Pb/^{204}Pb$ versus $^{206}Pb/^{204}Pb$ and e) $^{208}Pb/^{204}Pb$ versus $^{206}Pb/^{204}Pb$ including the Pacific versus Indian MORB discrimination line (black) by Pearce et al. (2007). Colour and symbol coding as in Figure 3.2 and 3.4, but MORB isotopic data (small cross symbols) divided into Pacific (red) and Indian (orange) MORB. A to C approximal ratios of endmembers defined in the text. Indian- and Pacific MORB isotope data from (Bach et al., 1994; Chauvel and Blichert-Toft, 2001; Dosso et al., 1988; Hamelin and Allègre, 1985; Hegner and Tatsumoto, 1987; Ito et al., 1987; Klein et al., 1988; Klein et al., 1991; Macdougall and Lugmair, 1986; Mahoney et al., 2002; Mahoney et al., 1992; Mahoney et al., 1989; Mahoney et al., 1994; Michard et al., 1986; Newsom et al., 1986; Price et al., 1986; Pyle et al., 1992; Rehkaemper and Hofmann, 1997; Salters and White, 1998; Vlastelic et al., 1999; Wendt et al., 1999; White et al., 1987).*

The variation of incompatible element and isotope ratios along the NELSC indicate variable magma sources contributing to the distinct NELSC segments at a small spatial scale. The radiogenic isotope ratios (Figures 3.6) indicate three mixing endmembers affecting magmas along the NELSC and in the surrounding area: Endmember A with relatively high $^{143}Nd/^{144}Nd$ ratios of up to 0.5130 and low $^{87}Sr/^{86}Sr$ and Pb isotope ratios comparable to MORB,

endmember B with radiogenic Pb isotopes ($^{206}Pb/^{204}Pb$ >19.2) but low $^{143}Nd/^{144}Nd$, and endmember C with high Pb and intermediate Sr and Nd isotope ratios.

3.6.1 The variation of mantle depletion in the northern Lau Basin

Previous studies have shown that the TiO_2 contents in the magmas in the northern Lau Basin and the FRSC vary and primitive melts have variable SiO_2 contents resembling boninites (Cooper et al., 2010; Escrig et al., 2012; Keller et al., 2008). These authors suggested that a boundary between the less depleted mantle in the north and highly depleted mantle in the south is situated directly south of the MTJ (Figure 3.1). Our new data from the NELSC confirm this model because all lavas from the spreading axis as well as those from the seamounts at the propagating tip have relatively high TiO_2 and are basaltic with relatively low SiO_2 contents (Figure 3.2). The depleted endmember A is defined by high $^{143}Nd/^{144}Nd$ of 0.5130 and low $^{87}Sr/^{86}Sr$ and Pb isotope ratios and is highly comparable to MORB as defined by Jenner and O'Neill (2012). Endmember A has low Nb/Yb <1, but intermediate Ce/Pb ~12, Ba/Nb ~20 and $(La/Sm)_N$ ~1 (Figures 3.4 and 3.6) and thus indicates little influence of a slab component enriched in fluid-mobile elements like Pb and Ba. Samples especially from from Segment IV and the southernmost seamounts define this particular end of the isotopic trends. N-MORB normalised incompatible element patterns (Figure 3.3) show positive K and Pb anomalies, LILE (e.g. Rb, K, Sr), depleted HREE and negative Nb-Ta anomalies indicating addition of a fluid-related slab component to a variably depleted mantle. However, lavas and volcanic glasses especially from the DR and Niuatahi have clear boninitic affinities, i.e. the mafic rocks are predominantly andesitic in composition with Ti_8 contents lower than 0.5 wt.% (Figure 3.5b). In this respect, the Niuatahi and DR lavas resemble those from the reararc volcano West Mata, close to Niuatahi a few km further north (Resing et al., 2011) suggesting that the abundant reararc volcanoes in the NE Lau Basin have a similarly depleted source.

The eruption of lavas with boninitic affinity at the reararc volcanoes Niuatahi, West Mata, and DR implies that the mantle beneath this region is harzburgitic with low Ti contents. Lupton et

al. (2015) found that the magmatic rocks of the NE Tonga Arc, the reararc volcanoes like Niuatahi, West Mata, and the FRSC have $^{3}He/^{4}He$ between 7.0 and 8.0 R/R_a, most likely due to a contributing enriched slab component. While the depleted mantle beneath the Tonga Plate appears to be affected by a slab component, more fertile mantle is flowing into the NELSC. Due to the large range of R/R_a of 8 up to 33.7 in Samoa (Jackson et al., 2005; Nebel et al., 2018), this option of a mantle-endmember is possible. The occurrence of various depleted and enriched endmembers existing in the upper mantle of the NE Lau Basin will be discussed in more detail below.

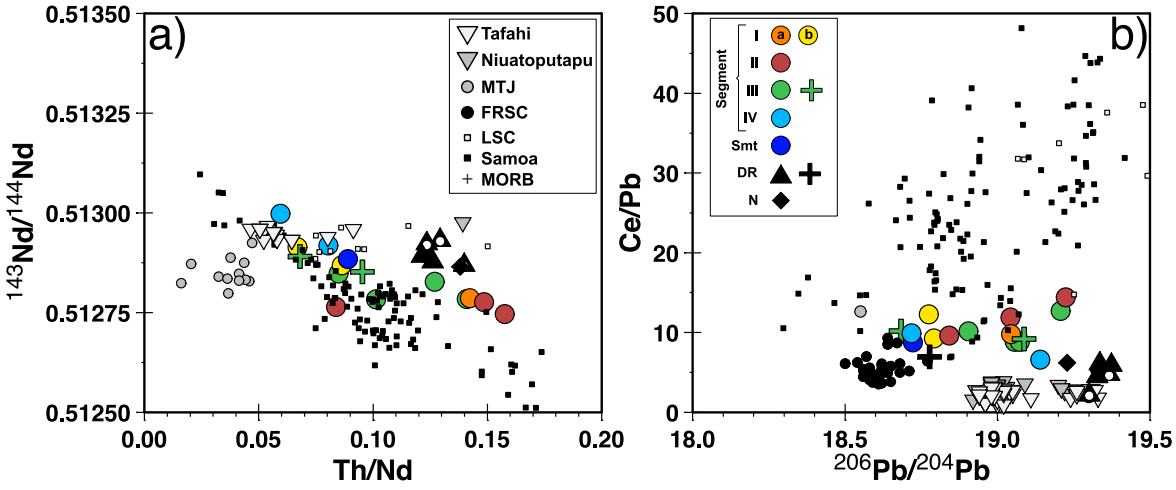

Figure 3.7 *Selected trace element ratios versus isotopes of a) Ce/Pb versus $^{206}Pb/^{204}Pb$ and b) $^{143}Nd/^{144}Nd$ compared to Th/Nd. Colour and symbol coding as in Figure. 3.2 and 3.4. Literature data as in Figure 3.4 and 3.6.*

3.6.2 Definition and origin of the mantle endmembers

Both trace elements (Figure 3.4) and isotopic ratios (Figure 3.6 and 3.7) indicate more enriched endmembers influencing the NELSC samples further north and at the DR. Also, in a plot of K_2O/TiO_2 versus H_2O/TiO_2 two main trends define the southernmost NELSC (Figure 3.8c), with one Segment I and two DR samples on the high H_2O, low K_2O branch and the other samples showing lower H_2O and higher K_2O. It must be noted that H_2O contents of the high K_2O/TiO_2

trend show degassing (Figure 3.8b), so we have to handle these contents as minimum values. In order to explain these two trends by simple mixing, Danyushevsky et al. (1993) state that at least three endmembers are required with the high- H_2O component derived from the subducting slab which is frequently observed along more complex or less established backarcs, e.g. the southernmost part of the NELSC including the seamounts.

3.6.2.1 Origin of the mantle endmember B

Endmember B has low $^{143}Nd/^{144}Nd$ of 0.51275, intermediate $^{87}Sr/^{86}Sr$ of 0.704 and high Pb isotope ratios (Figure 3.6) and is most clearly identified in Segment Ia, II and III basalts. This endmember is enriched, producing melts with $(La/Sm)_N$ >5, Nb/La >1 and high Ce/Pb ~15 but low Ba/Nb ~10 (Figures 3.4 and 3.7) compared to island arc lavas, reflecting an enriched mantle source resembling that of oceanic island basalts (OIB). Beside the OIB source, the relatively low Ba/Nb and high Ce/Pb of these enriched samples show little subduction influence, but the combination of negative Nb-Ta and high K imply that the entire mantle beneath the NELSC is affected by a subtle slab component (Figure 3.3).

The most common OIB signature in the northern Lau Basin is assumed to be derived from material influx from the Samoan hotspot in the north (e.g., Tian et al. (2011), Jenner et al. (2012)). Samoa data (Hart and Jackson, 2014; Horan et al., 2018; Jackson et al., 2014; Jackson and Carlson, 2012; Jackson and Hart, 2006; Jackson et al., 2010; Jackson et al., 2007a; Jackson et al., 2008; Jackson et al., 2007b; Jackson and Shirey, 2011; Kendrick et al., 2015; König et al., 2011; Konter and Jackson, 2012; Konter et al., 2016; McDougall, 2010; Price et al., 2014; Reinhard et al., 2019; Salters et al., 2011; Sims et al., 2008b; Workman et al., 2004; Workman et al., 2006) show a broad range of both Sr- and Nd-isotopes mainly varying from 0.705 to 0.710 and 0.5125 to 0.5129, respectively (Figure 3.6). Lead isotope data from Samoa range from ~18.5 to 19.3 in $^{206}Pb/^{204}Pb$ and ~15.5 to 15.7 in $^{207}Pb/^{204}Pb$. In $^{208}Pb/^{204}Pb$ vs. $^{206}Pb/^{204}Pb$ we observe two trends of the NELSC lavas with those comparable to Samoa showing slightly higher $^{208}Pb/^{204}Pb$ ranging from ~38.7 to 39.5 (Figure 3.6e). If

considering the radiogenic isotope ratios, Samoa could fit as a representative for endmember B. Also, we observe overlapping compositions between Samoan lavas and NELSC data with respect to their increased Sr, Nb, LREE, Pb, Th and U contents as well as their trace element ratios (Figure 3.4). Concluding, we propose that the enriched endmember B compositions are consistent with an OIB-like enrichment that may be the result of influx of material from the Samoa mantle plume due to higher $^{207}Pb/^{204}Pb$ and lower $^{143}Nd/^{144}Nd$ and enriched trace element compositions (Figure 3.6).

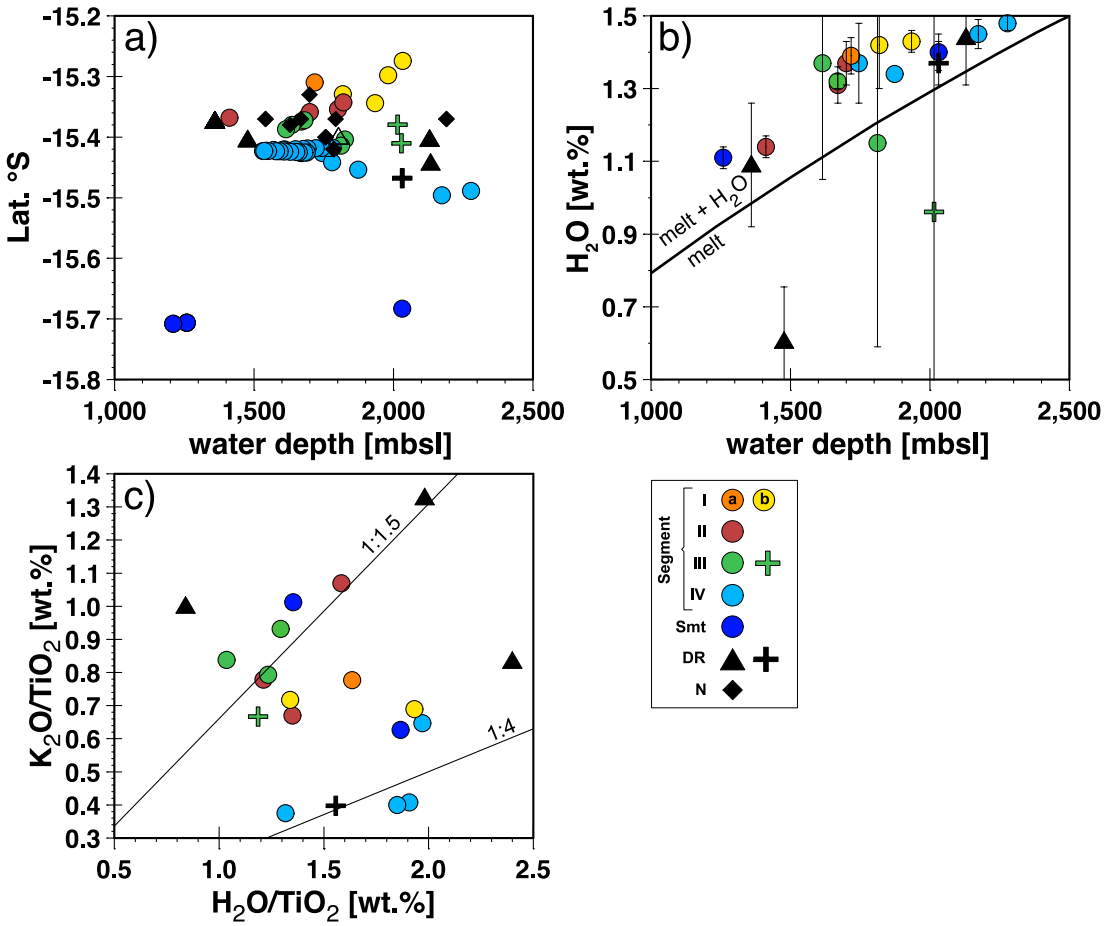

Figure 3.8 *Examined SO263 samples with a) latitudinal distribution and b) water contents in wt.% in comparison to water depth in mbsl (meters below sealevel). Water saturated curve for basaltic melts from Danyushevsky et al. (1993) indicating most lavas from the NELSC region are water saturated as plotting in the melt + H_2O field inferring a certain degree of degassing and c) showing K_2O/TiO_2 versus H_2O/TiO_2 indicating two trends of ratios around 1:1.5 and 1:4. The steepness of the slope indicates the degree of subduction influence (Danyushevsky et al., 1993).*

3.6.2.2 The origin of endmember C

Lead isotope signatures of the DR all lie on a narrow range comparable to, but slightly higher than those from Niuatahi volcano (Figure 3.6). Therefore, the very high Pb signature of the DR cannot be explained by direct source influence from a source underneath Niuatahi. The $^{206}Pb/^{204}Pb$ ratios are generally higher than at the NELSC except for one Niuatahi sample that shows the same ratio as the more alkaline samples from the NELSC (Figure 3.6). Both $^{207}Pb/^{204}Pb$ and $^{208}Pb/^{204}Pb$ of DR and Niuatahi are slightly lower than the highly radiogenic NELSC samples (Figure 3.6d, e). The southward gradients in Nb/La, $^{206}Pb/^{204}Pb$, and $^{143}Nd/^{144}Nd$ (Figures 3.4b and 3.6) indicates a southward-directed material transport from the NELSC towards the FRSC. However, the radiogenic isotopes show that no simple mixing relations exist between NELSC, MTJ and FRSC sources (Figure 3.6), also seen in $^{143}Nd/^{144}Nd$ versus Sm/Nd (not shown).

Endmember C has intermediate $^{143}Nd/^{144}Nd$ and $^{87}Sr/^{86}Sr$ of 0.5129 and 0.704 and relatively elevated Pb isotopes, respectively (Figure 3.6). This endmember also displays a strong slab component with low Ce/Pb of 2-6 and Nb/La <0.6 but high Ba/Nb >50 and $(La/Sm)_N$ >1.4 (Figure 3.4). The Pb-isotope ratios overlap with those from the LSC (Beier et al., 2011) (Figure 3.6). The Rurutu trend (Chauvel et al., 1997; Hanyu et al., 2013) from the Cook-Austral region shows even higher Pb isotope ratios extending the LSC trend, but do not fit in Sr-Nd space and therefore seems unlikely to represent the enriched source compositions of the DR. Therefore, the only regional compositional source to explain the isotopic variability along the DR are compositions derived from a material similar to that from the LSC. The general properties of the LSC lavas are high Nb/Ta and Nb/Zr ratios along with high Pb-ratios and strongly negative Ce-anomalies (Figure 5a) also seen in the northern Tonga Arc islands Niuatoputapu and Tafahi (Beier et al., 2017; Beier et al., 2011). Comparing our samples with those from Tafahi and Niuatoputapu, we observe Nb/Ta ratios of up to 35.71 along with Ba/Th ratios of <200 comparable to Tafahi data (Figure 3.4c). The Ce/Ce* (= $Ce_N/(La)_N^{0.5} \times (Pr)_N^{0.5}$)

along the DR (including literature data from Park et al., 2015) range from 0.96 to 1.10, while NELSC lavas are thoroughly dominated by ratios >1.00 up to 1.10 (Figure 5a). Even though these negative anomalies are not as extreme as those from Niuatoputapu or Tafahi ratios that reach as low as 0.6 or those of the LSC lavas (0.5), our samples tend towards more elevated Tafahi, Niuatoputapu and LSC lavas indicating that a LSC component may be present underneath the DR and Niuatahi and may not be restricted to the northern Tongan arc volcanoes as previously proposed (Beier et al., 2017; Timm et al., 2013).

3.6.3 Along-axis variation of the NELSC towards the southernmost seamounts

The northern and central lavas from the region of the NELSC, where Segments I, II and III overlap display an extreme compositional variability in source enrichment with $(La/Sm)_N$ ranging from 1.0 to 4.6, Nb/La from 0.4 to 1.1, and $^{206}Pb/^{204}Pb$ from 18.8 to 19.2 (Figures 3.4 and 3.6). While lavas from the FRSC and the MTJ show increasing Nb/La and $^{206}Pb/^{204}Pb$ combined with decreasing $^{143}Nd/^{144}Nd$ (Figures 3.4 and 3.6) towards the north, our NELSC samples indicate a large geochemical anomaly with all three endmembers contributing to the compositional range. A single sample (SO263 102VSR-01) along the NELSC shows DR-like major, trace element and isotope ratios. This sample is located at -15.45°S where the tip of the DR is closest to the NELSC, however, we do not observe abundant geochemical evidence for an extensive flow of melts from the DR towards the south of the NESLC. Other lavas from Segment III and those from Segment II are the most enriched in terms of incompatible elements and have high $^{206}Pb/^{204}Pb$ and the lowest $^{143}Nd/^{144}Nd$ implying influence by endmember B (Figure 3.6).

The southern NELSC lavas (Segment IV) and the southernmost seamounts have some of the lowest Pb and Sr isotope signatures and highest Nd isotopic ratios along the NELSC (Figure 3.6) indicating the MORB-like endmember mantle (endmember A; Figure 3.6) is less overprinted by subduction influence in this region. The three seamounts that were sampled ~30 km south from the southern tip of the NELSC are likely to represent continuing rifting

towards the FRSC and therefore young volcanism occurred at the rift tip (Anderson et al., 2020; Baxter et al., 2020; Haase et al., 2018). Two of the seamounts do not directly lie on the rift axis but erupted off-axis on older crust (Figure 3.1b). The trace element and isotope composition of the lavas from the three seamounts suggest that they are part of the NELSC magmatic system. For example, major element data show that the southernmost seamount samples lie on the fractionation trends of TiO_2 and SiO_2 versus MgO (all in wt.%) comparable to those from the NELSC. The most prominent differences occur in TiO_2 (Figure 3.2c) and FeO^T (Figure 3.2d) where the southern seamount samples lie on the trends with the NELSC showing a steep slope towards higher Fe and Ti contents with decreasing MgO. The southern lavas tend to elevated K_2O+ Na_2O (wt.%) at low SiO_2 contents (Figure 3.2a) which could indicate relatively lower degrees of partial melting compared to the rest of the NELSC magmas except from Segment II.

The southern tip of the NELSC lies at the greatest distance from the arc when considering the entire Lau Basin system and should show the smallest influence from the subducting slab. In general, the H_2O-flux from the down-going slab in the Tonga region occurs between 100 and 230 km depth (van Keken et al., 2011) and the slab depth beneath the NE Lau Basin is relatively shallow between 90 and 150 km (Hayes et al. (2012). Thus, some input from the subducting slab is likely in the NE Lau Basin and can explain the ubiquitous evidence for metasomatism of the mantle by hydrous slab-derived fluids. All NELSC lavas including the seamounts have typical arc-related incompatible element pattern (Figure 3.3) with negative Nb-Ta anomalies and relatively enriched LILE. Also, experiments by Hermann et al. (2006) and Spandler et al. (2007) showed Cs and Na as well as K, Rb, Ca and Sr are fluid mobile, while La, Th and Zr are immobile. The higher the fluid proportion of a mixture between fluids and a hydrous melt, the higher, e.g., Rb/La and K/La (Spandler et al., 2007). Analogous to this, we expect ratios like Ba/Nb (Figure 3.4b) or Sr/Nd to also indicate fluid rather than hydrous melt input. The southernmost NELSC and seamount samples show fluid mobile/immobile

element ratios and *vice versa* with high Ba/Nb of 20 to 153 (MORB <15), Ba/La of 13 to 23 (MORB <15) and with low Ce/Pb of ~10 (MORB ~20-30) which are closest to DR and Niuatahi ratios. Therefore, they display some of the highest values along the NELSC but also amongst the lowest Nb/Yb reflecting a more depleted mantle beneath the southern NELSC (Figure 3.5a) with an enrichment from fluid-mobile elements by a slab component.

Thus, we suggest that simple adiabatic melting of a mantle that has experienced prior melt depletion causes magma formation beneath the rift tip. This increased melt depletion is likely caused by melt loss during mantle flow also called “mantle preconditioning” (Pearce and Stern, 2006a; Pearce et al., 2005), i.e. incompatible elements are extracted by mantle melting in the backarc region so mantle flowing towards the arc is more depleted (Kincaid and Hall, 2003). This melt loss is indicated by the mantle heterogeneities seen along the NELSC where the mantle flowing along-axis loses fractions of more enriched melt causing further depletion towards the south (Pearce and Stern, 2006a; Pearce et al., 2005). We therefore conclude that the NELSC samples lie on a mixing trend between MORB compositions as seen at the southernmost seamounts (endmember A) and an enriched OIB (Samoan-like) endmember B.

3.6.4 Melting and mixing processes along the NELSC and southernmost seamounts

In general, the northern Lau Basin is known for its induced across-axis flow which implies that asthenosphere is drawn to the mantle wedge from the backarc spreading centre (Conder et al., 2002). A flow pattern where asthenosphere that has previously experienced melting at the ridge flows towards the arc explains the greater depletion often observed in arc basalts relative to their associated backarc basalts (e.g., McCulloch and Gamble (1991)). This relationship has previously been observed in Tonga Arc basalts, where greater depletion correlates with increased local backarc spreading rates (Ewart and Hawkesworth, 1987). Spreading rates of the NELSC are around 120 mm/a (Baker et al., 2019; Bird, 2003) causing fast mantle upwelling rates and thus relatively high degrees of adiabatic partial melting. The lack of a clear ridge

south of the actively spreading NELSC suggests that rates of spreading are decreasing (Figure 3.1b). Samples from the southern seamounts and from the overlapping section of the NELSC are more alkaline (Figure 3.2a, e) indicating relatively smaller degrees of partial melting and/or more enriched source compositions. This is consistent with the observation of Langmuir et al. (1986) that ridge offsets generally show a lower extent of melting and comparatively more enriched basalts. However, the overall high degrees of partial melting do not easily allow a more exact estimation by using trace elements. In addition, we see a correlation between melting-sensitive ratios (e.g. Lu/Sm) and source indicators (e.g. Nb/Yb; Figure 3.5a) implying that sources and degrees of partial melting may variably impact on the trace element ratios.

To correct element contents for differentiation, the elements are corrected along a linear regression to a MgO content of 8 wt.%. During decompression melting along mid ocean ridges, degrees and pressure of melting result in a negative correlation of $(Na_2O)_8$ and $(FeO^*)_8$ (Figure 3.9a) (Klein et al., 1988). Our samples show a positive correlation with two trends indicating lower melting temperatures at Segment Ia, II and III and highest extents of melting along the southernmost seamounts and DR (Taylor and Martinez, 2003). At the same time, the seamounts and DR samples have lowest the $(TiO_2)_8$ (Figure 3.9b, c), highest Ba/La and relatively high $(H_2O)_8$ (Figure 3.9c) supporting higher degrees of melting induced by a stronger slab contribution as arc-like samples show low $(Na_2O)_8$, $(FeO^*)_8$ and $(TiO_2)_8$ (Figure 3.9) along with elevated fluid sensitive ratios (Taylor and Martinez, 2003). These low Fe and Ti melts combined with a higher H_2O content are generated under equilibrium and low pressures below 12 kbar, while dry, high Fe and Ti are the result of fractional melting at higher pressures (Langmuir et al., 2006).

Also, ratios of Ba/La show a strong negative correlation with $(TiO_2)_8$ (Figure 3.9d) which indicates varying stronger contributions of a slab fluid component to the depleted mantle wedge (Langmuir et al., 2006). However, Ba/La and $(H_2O)_8$ are not correlated indicating a

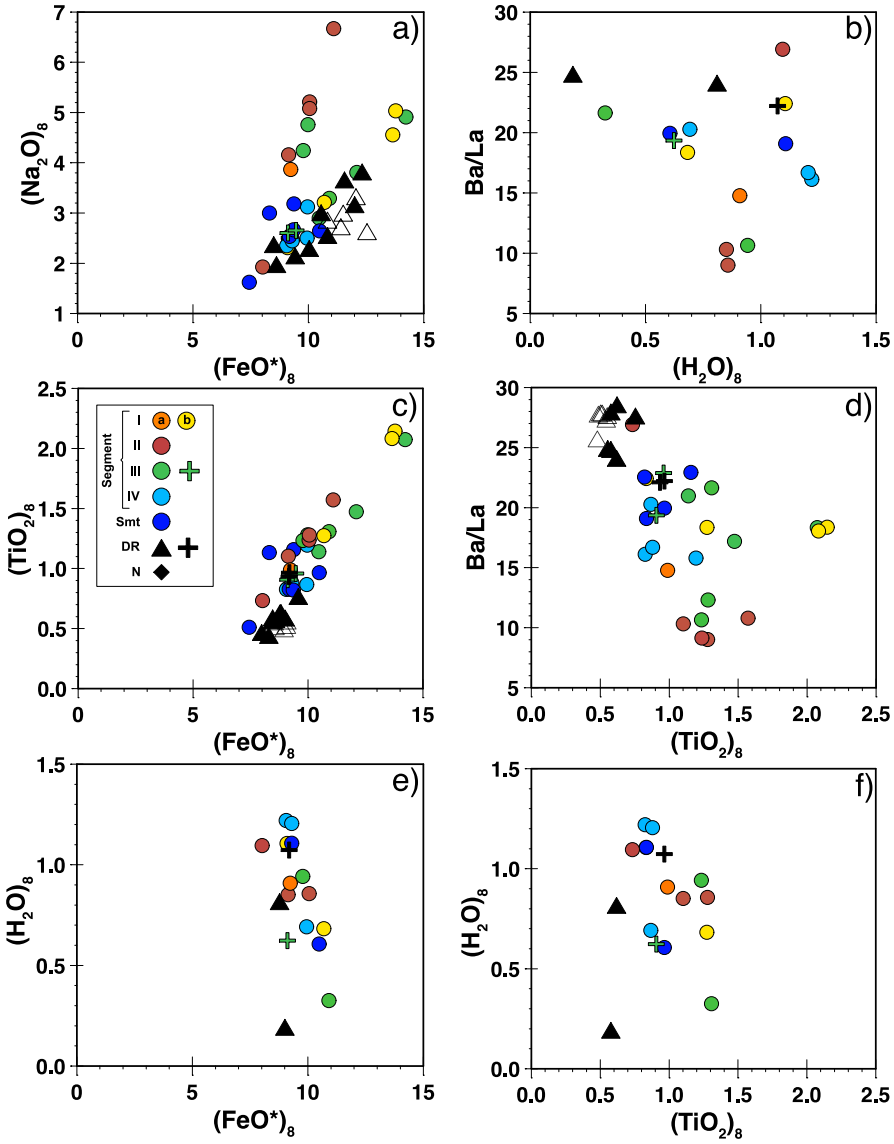

Figure 3.9 *Fractionation corrected major elements and selected trace element ratios for samples with MgO >4 wt.%. Correction calculations via $C_{measured}$ + (m*($MgO_{measured}$-8) with C as the concentration of the selected element in wt.% of the sample and m the slope of the fractionation curve of the element concentrations versus MgO in wt.%, respectively. Plots of a) (Na_2O) versus Fe_8, b) $(TiO_2)_8$ versus $(FeO^*)_8$, c) $(H_2O)_8$ versus $(FeO^*)_8$, d) Ba/La versus $(TiO_2)_8$, e) $(H_2O)_8$ versus $(TiO_2)_8$ and f) Ba/La versus $(H_2O)_8$. Colour coding by different sample location as in Figure 3.2.*

decoupling of Ba/La and $(H_2O)_8$ (Figure 3.9b). Especially lavas from Segment II shows a high discrepancy between the trace element ratio and H_2O contents with lowest Ba/La but medium to high $(H_2O)_8$ compared to the other samples (Figure 3.9d-f). We interpret the decoupling of incompatible and highly mobile trace element ratios and $(H_2O)_8$ to result from extensive

degassing of H_2O also seen in the inverse correlation of water content and water depth (Figure 3.8b).

The variation of relatively depleted samples in the northern NELSC towards highly enriched samples, and depleted samples in the central and southern part of the NELSC, respectively, result from varying contributions of different sources to the melting region. This variation in depletion is correlated with a stronger enrichment in fluid mobile element concentrations (e.g. Ba/Nb versus Nb/La, Figure 3.4b), likely because less volume of enriched material will be required to cause a higher signal. As stated above, we observe the endmember B (OIB-like) signature both in trace element and isotope ratios for the Segment II and III samples. It must be noted though that the enriched signature is generally evident in the central region of the spreading ridge, contrasting a simple southward mantle flow from Samoa from the north underneath the NELSC. If this were the case, we would expect this signature to be present beneath the most northern tip of the NELSC (Segment I) systematically decreasing southward. As we do not see this gradual flow, we propose that the restricted occurrence of the enriched signature may be caused by small-scale enriched mantle heterogeneities with a Samoan-like composition underneath Segment II and III that have been proposed to be abundant in the upper mantle (Zindler et al., 1984).

3.6.5 Formation of the Diagonal Ridge magmas

The DR extends from Niuatahi in the east towards the NELSC at around 15.4°S (Figure 3.1). Given the proximity of the DR to both the arc and backarc, we expect a gradual transition from arc towards backarc affinities from west to east and also a similarity of samples from the NELSC closest to the DR. Trace elements sensitive to melt depletion like Nb/Yb decrease with increasing slab depth and increase slightly at the western end of the DR (Figure 3.5a). We expected similar ratios at the region where the DR is closest to the NELSC, but NELSC samples at along 15.4° (Segment III and IV) do not deviate from those observed along the NELSC (Figure 3 and 4). Trace element patterns normalised to averaged N-MORB data (Gale

et al., 2013) indeed display similarities especially between DR and the off-axis samples (green cross symbols) along with Segment IV and the seamounts (Figure 3).

The subduction influence (Ba/Nb, Ce/Pb) is highest at Niuatahi and the DR (Figure 3.4a, b). It is worth noting, that Niuatahi and some DR samples have <5 wt.% MgO, but the general DR trend is also observed in the less evolved samples. We observe elevated Ba/Nb ratios (Figure 3.4b) along the DR and very low ratios at the northern part of the NELSC where fluid influence derived from the subducted slab is lowest consistent with the overall trace element patterns (Figure 3.3a and b).

Lead isotope signatures of the DR all lie in a narrow range comparable to, but slightly higher than those from Niuatahi volcano (Figure 3.6). Therefore, the elevated Pb isotope signature of the DR cannot be explained by simple mixing of melts or sources from Niuatahi and endmember A or B but a third endmember (C) is involved. The $^{206}Pb/^{204}Pb$ ratios are generally higher compared to most NELSC lavas except for the Segment II and III basalts showing the highest $^{206}Pb/^{204}Pb$ isotope ratios. However, the $^{207}Pb/^{204}Pb$ and $^{208}Pb/^{204}Pb$ of DR lavas are significantly lower than those of any of the radiogenic NELSC samples (Figure 3.6). In terms of the isotopes and particularly in terms of Pb isotope compositions the DR lavas resemble lavas of Niuatoputapu on the island arc front (Figure 3.6). Thus, we propose that the LSC signatures may not be geographically restricted as proposed by Beier et al. (2017) to Niuatoputapu and Tafahi but are more widespread in the north-eastern Lau Basin. We propose that during subduction of the LSC several million years ago, the geochemical signature from the subducting seamounts was emplaced in the overlying island arc crust (Ruellan et al., 2003). During slab rollback and backarc spreading this material may be incorporated into the ascending melts leading to locally restricted mantle heterogeneities along the entire Tonga-Kermadec Arc also seen by Timm et al. (2013).

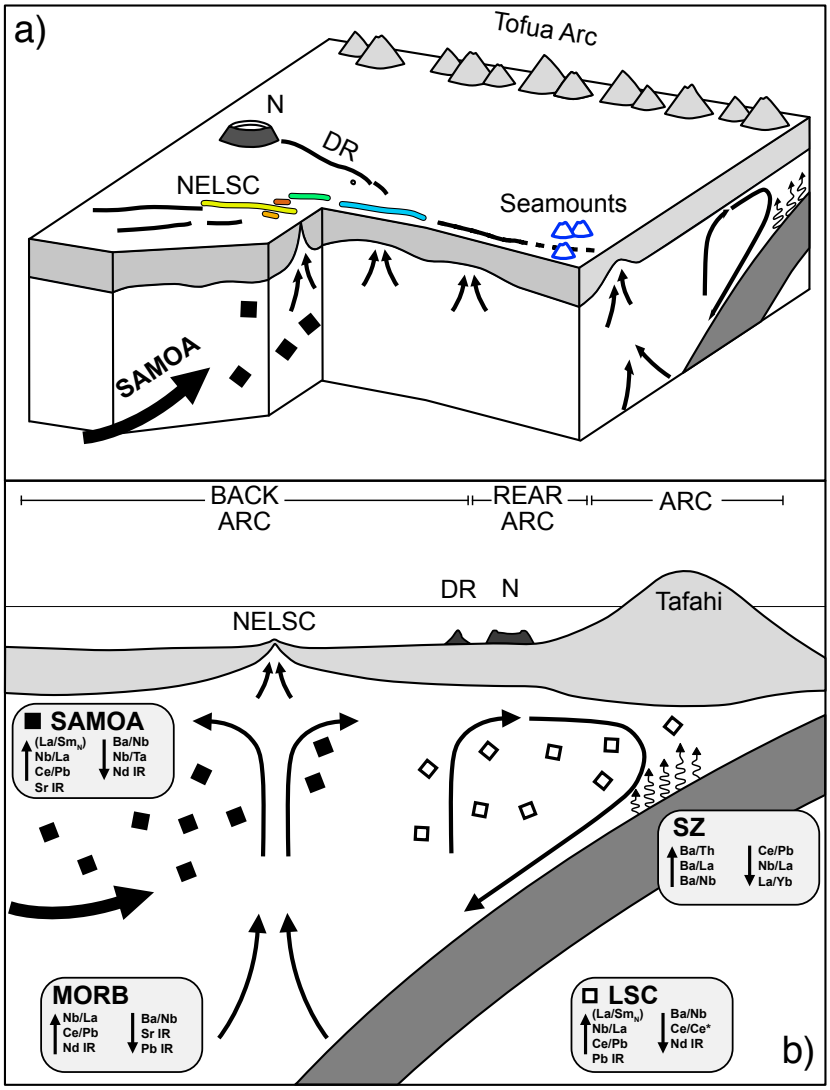

Figure 3.10 *Schematic illustration of the NELSC region showing the influence of Samoa, LSC, the subducting slab (SZ for subduction zone) and MORB in a) a three-dimensional model focusing on the NELSC and b) a cross-section from arc with Tafahi as an exemplary arc volcanic island towards the backarc. Major characteristics of the different sources described in the text are summarised.*

3.7 CONCLUSIONS

We used major and trace element and Sr, Nd and Pb isotope data combined with H_2O analyses from the NELSC, southernmost seamounts and the DR to investigate the influence of the subducting slab on the source composition. We also focused on the gradual compositional changes of the backarc in proximity to the reararc. Based on major and trace element

systematics we can show that the southernmost seamounts are genetically connected to the NELSC and the backarc spreading is likely to continue southwards with decreasing degrees of partial melting (cf. Baxter et al., 2020). Despite the high spreading rates in the northern Lau Basin, mantle heterogeneities are still detectable and Sr, Nd and Pb isotopic ratios show that the lavas along the NELSC are mainly influenced by mixing of two OIB mantle endmembers in addition to the arc (Figure 3.10). Elevated Pb isotopic ratios indicate mixing of an enriched OIB component likely derived from the Samoa plume in the north with depleted MORB-like mantle. A gradual change in the source signature from north to south cannot be observed, so instead the varying degrees of enrichment along the NELSC indicate a highly heterogeneous mantle composition in this area. The third mantle source endmember that influences the mantle source in this area of the Lau Basin derives from the subducted LSC (Figure 3.10) and is restricted to the DR. Based on the presence of the LSC signature in DR lavas and the absence in lavas from NELSC and the southernmost seamounts, we conclude that there is no extensive exchange between the reararc and the backarc magmas. Moreover, we cannot see a gradual systematic change in fluid sensitive trace element ratios derived from the subducting slab with increasing distance to the arc front. We conclude that the signal of fluid-sensitive elements from the subducting slab is diluted by extensive adiabatic melting of a depleted source beneath the NELSC spreading axes mixed with an enriched mantle source endmember.

For future studies, the analysis of He-isotope ratios would be appropriate to further investigate the potential influence of the Samoa plume in this region. The use of U-series data will significantly improve the knowledge about the influence of fluids from the subducted slab on the melts from the Lau Basin and reararc.

3.8 ACKNOWLEDGEMENTS

We thank Captain Oliver Meyer and his crew for the help and effort during SO263 Tonga Rift. We acknowledge the professional help and support of Volker Ratmeyer and the team of ROV MARUM Quest. This publication was funded by the projects BE 4459/8-1 and BR 5297/2-1 BISMArc from the Deutsche Forschungsgemeinschaft.

3.9 SUPPLEMENT

All major and trace element, radiogenic isotopes and water data analysed for this chapter are shown in table A1 of the Appendix along with standard analyses and analytical errors in tables A4, A5 and A6.

4 DYNAMICS OF MELTING ALONG BACKARC SPREADING CENTRES CLOSE TO SUBDUCTION ZONES

M.V. Schoenhofen[1, 2], C. Beier[1, 3], L.E. McGee[2, 4], K.M. Haase[1], P.A. Brandl[5], M. Regelous[1] and S. Turner[2]

[1]*GeoZentrum Nordbayern, Friedrich-Alexander-Universität (FAU) Erlangen-Nürnberg, Schlossgarten 5, 91054 Erlangen, Germany;*

[2]*Department of Earth and Planetary Sciences, Macquarie University, Sydney NSW 2109, Australia*

[3]*Department of Geosciences and Geography, University of Helsinki, PO Box 64, FIN-00014 Helsinki, Finland*

[4]*Department of Geosciences and Geography, University of Adelaide, Australia*

[5]*GEOMAR Helmholtz Centre for Ocean Research Kiel, Wischhofstr. 1-3, 24148 Kiel, Germany*

4.1 ABSTRACT

The processes leading to melting along backarc spreading centres have many similarities to those observed at mid-ocean ridges. Backarcs however, are influenced by fluids from the subducting slab resulting in different melting conditions and lava compositions, respectively. In order to investigate the nature of the melting processes in arc-proximal backarc basins we present new LA-ICP-MS trace element data along with U-Th-Ra isotope data and SHRIMP-SI water measurements from the southernmost tip of the Lau Basin close to the Tonga arc. We combine these with literature data from the Lau Basin to evelop a model of the conditions of melting in the entire Lau Basin. Previous melting models showed that the melting regime along the Lau Basin can be distinguished into a dry, arc-distant and a wet, arc-facing side resulting in different melting regimes and influence of fluids on the magmatic system of the backarc. Samples located on a N-S axis throughout the Lau Basin show a gradual decrease in fluid- and melting-sensitive parameters with an increasing distance to the Tonga Arc. We aim to test here if similar changes in fluid addition and melting regime can be observed in zero-age samples along an E-W transect along the Valu Fa Ridge (VFR) located <50 km distance from and orthogonal to the Tonga Arc. We use highly fluid and melting sensitive U-series isotopes along with water contents to disentangle the influence of fluids and the changes in melting regime with increasing distance from the arc. In our E-W transect we do not observe a gradual decrease of the subduction influence in water, U-series or subduction sensitive ratios like Ba/Nb with increasing distance from the arc. In fact, there is no correlation of these indicators with distance along the 25 km-long transect. We can, however, show that the samples erupted directly at the spreading axis show a stronger subduction zone influence as well as increased sediment tracer signals (e.g., Dy/Dy*) and the lowest degree of depletion along the transect. We interpret this to be the result of the spreading axis being fed by a source strongly influenced by the subducting slab. This, along with the lack of clear chemical changes with increasing

distance from the arc, we interpret an overlap of the melting zones where homogenisation of melts is a major process for the formation of backarcs within <50 km distance to the arc.

4.2 INTRODUCTION

Magmas forming in supra-subduction zone environments are influenced by igneous and sedimentary components from the subducting oceanic plate, the overlying mantle wedge and crust (Pearce and Peate, 1995). Lavas erupted in the adjacent backarc spreading axis vary in composition from arc-like magmas, enriched in large ion lithophile (LILE) and volatile elements and depleted in high field strength elements (HFSE) (Kelley et al., 2006; Langmuir et al., 2006; Taylor and Martinez, 2003) to mid-ocean ridge (MOR) like compositions further distant from the arc (Pearce and Stern, 2006b). The change in composition reflects the distinct change in melting regime from hydrous melting closer to the arc to decompression melting more distant from the active subduction (Kelley et al., 2006; Kelley et al., 2005; Peate et al., 2001). The extent to which these different melting regimes contribute to backarc melting regimes forming at distances of less than 250 km to the active arc remains unresolved (Peate et al., 2001). Langmuir et al. (2006) developed a model which involves mixing of melts from a relatively ‘wet’ melting regime in the backarc’s melting regime closer to the arc with a relatively ‘dry’ melting regime at the backarc side more distant to the arc. The underlying assumption in these models is that the signatures of melting must change from relatively wet, hydrous, arc-like signatures to relatively dry, decompression melts as one transects from the arc to the backarc and beyond. In general, an increasing distance to the arc will be accompanied by an increasing Benioff-zone/slab depth (Hayes et al., 2012). If this is the case, the slab orthogonal geochemical transect should reflect the gradual changes in metamorphic, subduction related slab processes (Bebout, 2007), i.e. the geochemical signatures will change from a strong slab-related component due to the dehydration of the mafic slab components (Bebout et al., 2007) followed by deserpentinisation of the ultramafic slab components (Iwamori, 2007). Here, we

examine whether these differences are detectable on smaller spatial scales of 25 km. For the 25 km-long transect, the slab depth changes by ~30 km from ~110 km in the eastern part to 140 km depth in the western part of the transect (Hayes et al., 2012).The distinguishability of the dehydration signatures will strongly depend on the angle of the subducting slab (van Keken et al., 2011) and the formation of subduction mélange diapirs (Marschall and Schumacher, 2012) as well as overlapping of the melting zones between the arc and backarc (Wiens et al., 1998; Zha et al., 2014) will add additional complexity in the interpretation of the magma compositions.

The short-lived Uranium-series disequilibria and volatile contents provide a unique means for distinguishing the different regimes of melting (Kelley and Cottrell, 2009; Peate et al., 2001; Turner et al., 2003b). The short-lived nature of the U-Th-Ra decay chains (Bourdon et al., 2003c) allows them to track recent fluid addition to the melting regime in that the greater fluid mobility of U relative to Th (Turner et al., 2003b) results in higher U/Th ratios and excess of ^{238}U over ^{230}Th ($(^{230}Th/^{238}U)$ <1, where parentheses denote activity ratios). Elevated ($^{226}Ra/^{230}Th$) of up to 6 in lavas < 8ka and the similar behaviour of ^{226}Ra and Ba indicates that the fluids were added recently (Bourdon et al., 2003a; Elliott, 2004). Decompression melts from MORs are generally defined by excesses of ^{230}Th ($(^{230}Th/^{238}U)$ >1) and ($^{226}Ra/^{230}Th$) disequilibria of <4 (Lundstrom, 2003a). Several studies have shown that the morphology of the ridge axis, the crustal thickness and melt production correlate with distance to the arc (Dunn and Martinez, 2011; Martinez and Taylor, 2006; Sleeper and Martinez, 2014). Few studies however, have systematically investigated the influence of subduction zone components on the backarc arc melting regime combining U-Th-Ra disequilibria and volatile contents (Beier et al., 2010; Caulfield et al., 2012). Thus, the transition between a fluid-fluxed melting regime and decompression melting remains ambiguous.

The Eastern Lau Spreading Centre (ELSC) and its southern extension, the Valu Fa Ridge (VFR) in the western Pacific are situated at an increasing distance to the Central Tonga Arc

(Figure 1a) where the southernmost VFR approaches the active arc volcanoes as close as 30-50 km (Sleeper and Martinez, 2014) at a Benioff Zone depth of ~200 km (Hayes et al., 2012) increasing towards the north. Geophysical models have predicted an overlap of the melting zones between the arc and backarc in the south (Sleeper and Martinez, 2014; Zha et al., 2014) gradually separating northward along the ELSC. The proximity of arc and backarc in the southern VFR allows to decipher the influence of the arc, fluid-fluxed melting regime from the relatively dry, MOR-like decompressional melting environment.

Here, we use major element, trace element, U-Th-Ra and volatile data of a series of submarine samples from the southern VFR that are situated parallel to the subducting slab across the VFR. Our transect of samples shows a strong influence from the subducting slab. The backarc spreading environment significantly imprints on the formation of the magmas resulting in highly variable (^{238}U) excesses, also close to equilibrium but no gradual variation with proximity to arc.

4.3 GEOLOGICAL SETTING

The Tonga-Kermadec island arc is the longest subduction system on Earth (de Ronde et al., 2003). Along the arc front, around 60 distinct volcanic centres can be found (Cañón-Tapia and Walker, 2004). The Lau backarc basin started opening ~2.5 Ma ago (Boespflug et al., 1990; Malahoff et al., 1982) with about 6 cm/a (Von Stackelberg et al., 1990) due to seafloor spreading (Taylor et al., 1996). The plate model by Zellmer and Taylor (2001) shows that three plates are tectonically involved in the Lau Basin: the Australian Plate in the west, the Tongan Plate in the east and the Niuafo'ou microplate in between with spreading centres following the plate boundaries (Figure 1a). The Lau Basin is triangular-shaped (Figure 4.1a) and ~450 to 190 km wide at 18 and 26°S, respectively (Hawkins and Melchior, 1985). This basin separates the different segments of the Lau Ridge from the Tofua island arc (Figure 4.1a) (Boespflug et al., 1990; MacGregor et al., 2001).

The south Tofua arc between 21 and 25° S is about 425 km long and is located around 180 km W from the Tonga Trench (Massoth et al., 2007). In this area, the subduction rate is ~1.6

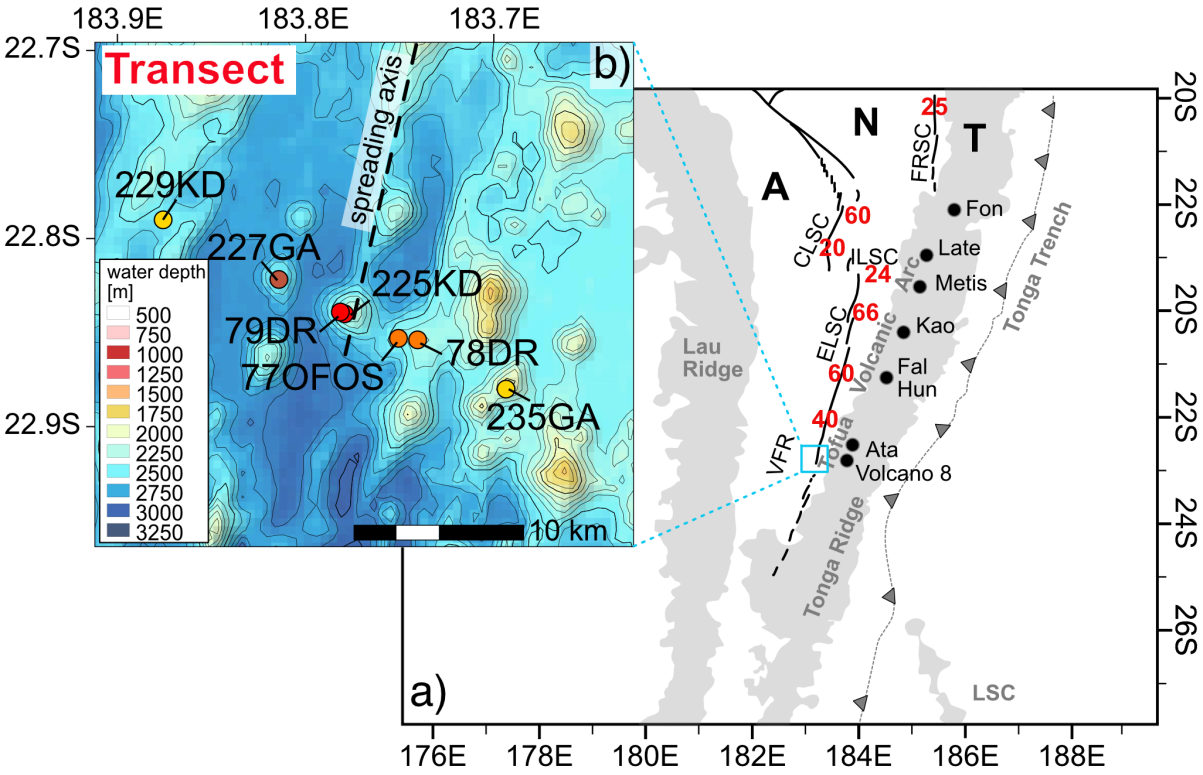

Figure 4.1 *Overview map of a) the remnant Lau Ridge in the west, the Tonga Arc in the east and the active Tofua Volcanic Arc with the arc volcanoes from N to S: Fonualei (Fon), Late, Metis, Kao, Falcon (Fal), Hunga Ha'apai (Hun), Ata and Volcano 8. The dashed grey line refers to approximate positioning of the Tonga Trench. In the SE, the location of the subducting Louisville Seamount Chain (LSC) is shown. For the Lau Basin the backarc systems of the Fonualei Ridge Spreading Centre (FRSC), Central Lau Spreading Centre (CLSC), Intermediate Lau Spreading Centre (ILSC), Eastern Lau Spreading Centre (ELSC) and the Valu Fa Ridge (VFR) including the spreading rates in red (Baker et al., 2019; Bevis et al., 1995; Parson and Wright, 1996; Sleeper et al., 2016) are shown. Bold letters stand for the Australian (A), Niuafo'ou and Tonga (T) Plates (Zellmer and Taylor, 2001). b) Bathymetric map (Gebco) of the location of the samples across the VFR with the approximate spreading axis are shown with the colour coding used for all plots dependent on distance of the spreading axis (see also Fig. 4.2).*

cm/a (Bevis et al., 1995) and the volcanic front is on top of remnant Eocene aged arc and carbonate platforms along with volcanic sediments (Bloomer et al., 1994; Hawkins Jr, 1985; Massoth et al., 2007). The 152-km long NE trending spreading axis of the Lau Basin between 21°26' and 22°44' S is the VFR (Massoth et al., 2007; Vallier et al., 1991) which has been active since ~0.7 to 0.9 Ma (Morton and Pohl, 1990). In the southern part of the basin, the

spreading axis is about 200 km W behind the Tonga Trench (Jenner et al., 1987; Vallier et al., 1991). The spreading rate decreases from 6 to 3.9 cm/a from N to S and the distance to the southern Tonga Arc changes from 40 to 20 km (Zellmer and Taylor, 2001). The VFR is divided by small overlapping spreading centres (OSCs) into a northern (NVFR), central (CVFR) and southern (SVFR) part (Von Stackelberg et al., 1990). A magma chamber was located beneath the central part of the VFR which is distributed for at least 100 km along the axis and about 2-3 km wide (Morton and Sleep, 1985). Samples from the southern VFR are basaltic to rhyolitic and show subduction signatures (Fretzdorff et al., 2006; Haase et al., 2009), while samples from the northern part are MORB-like correlated with increasing distance to the arc (Taylor and Martinez, 2003). In this study, we used samples from a transect in the southern part of the VFR from 22.79 to 22.88°S and 176.88 to 176.69°W (Figure 4.1b). We chose 6 zero-age samples to analyse for U-series and water that lie on an E-W transect in this area, i.e. they are situated orthogonal to the trench. While previous U-series studies focussed on samples aligned in a N-S direction along the ridge, we focus our U-series and water data on an orthogonal profile with distances ranging between ~27 and 47 km from the active arc (Figure 4.1b). The spreading axis is located at about 41 km distance from the arc and the transect samples are situated on both sides of the axis (Figure 4.2).

4.4 METHODS

4.4.1 Sample selection and sampling

The samples were taken during cruises 67 and 167 with the German *R.V. Sonne* in 1990 and 2002, respectively. For this study, we selected fresh volcanic glass samples from locations along the transect with distances of <1 km distance (red circle symbols), ~3 km distance (brown circle symbol) and 10 km distance (yellow circle symbol) from the axis (Fig. 4.1b and 4.2) with MgO contents preferably >5 wt.%. Two samples (orange circle symbols) are located between 4 and 5 km distance from the axis and more evolved with MgO contents of ~2 wt.% along with

~59 wt.% SiO_2 (Figure 4.1b, 4.2 and 4.3a). We treat these samples separately in cases where the trace element ratios are fractional crystallisation sensitive. Major element and Sr-Nd-Pb isotope data for the same transect samples have previously been published by Fretzdorff et al. (2006) and Haase et al. (2009) (Appendix A2).

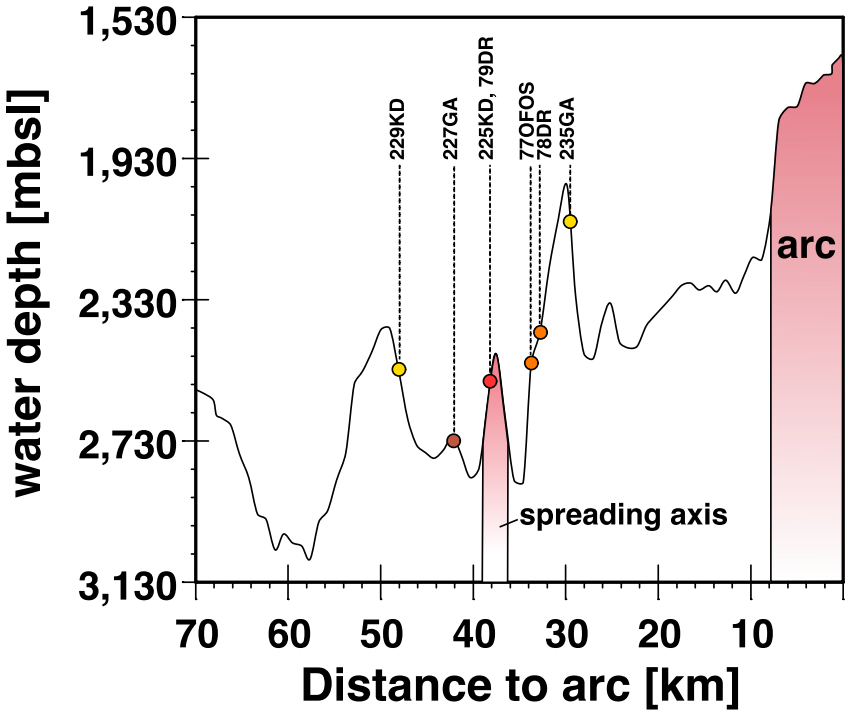

Figure 4.2 *Current location of the spreading axis beneath the transect south of the VFR including distance to the arc. Colour coding for samples for indicating distance from the spreading axis with red for closest location to yellow for most proximal locations.*

4.4.2 Trace element analyses

New trace element concentrations (Appendix A2) on the selected samples were analysed using an Photon Machines Excite Analyte 193 nm excimer laser ablation system coupled to a Agilent 7700× quadrupole ICP-MS with a with HelEx sample cell at Macquarie GeoAnalytical (MQGA), Macquarie University. A laser beam of 65 µm and a measurement time of 120s was used to analyse the volcanic glasses. Multiple individual points (n=4) on each glass sample

were measured and the data was averaged. NIST-610 glass standards were analysed after ever 5th sample to correct for machine drift. The NIST-610 standard was used for an external calibration of relative element sensitivities and Ca^{43} data for internal calibration. Accuracy was <10% for all elements (except for Li and Y with <13%) and reproducibility of <6% for all elements, based on the basaltic reference material BCR-2G (n=9). More details are given in Appendix A5.

4.4.3 Uranium-series analyses

Uranium-series were analysed on hand-picked unaltered volcanic glass samples which were washed and leached prior to dissolution and column chemistry as described in Heyworth et al. (2007) and McGee et al. (2011) and chapter 2.2.2.3.

The samples were analysed at the Macquarie University, Sydney, Australia. The U and Th cuts were analysed on a Nu Instruments® MC-ICP-MS following the method described in Dosseto et al. (2006), Heyworth et al. (2007) and McGee et al. (2011). Accuracy (<3.8%) was determined by the measurements of BCR-2 international rock standard that was processed along with the other samples throughout the whole analysis (Appendix A3).

The Ra cuts were analysed with a ThermoFinnigan Triton® TIMS after being loaded onto degassed Re filaments with a Ta-HF-H_3PO_4 activator solution. The $^{228}Ra/^{226}Ra$ ratios were measured in the dynamic ion counting mode. The accuracy of BCR-2 standard analysis shows 0.53% for ^{226}Ra and 1.33% for the ($^{226}Ra/^{230}Th$) ratios (Appendix A3). Reference values are from Scott et al. (2019) and Sims et al. (2013).

4.4.4 Water measurements

Water measurements of the transect samples were performed at the Australian National University (ANU), Canberra, Australia on the SHRIMP-SI. The handpicked glass chips were embedded in synthetic resin, polished and carefully removed from the resin using acetone and a hand-drill to embed the polished samples into aluminium holders in indium. The mounts were

coated with gold and analysed for $^{16}O^-$ and $^{16}O^1H^-$ following the method described in Turner et al. (2015). Care was taken to avoid cracks and inclusions in the glasses. Internal basaltic glass standards (n=6 each) ND61, ND70 and 24.1 (Turner et al., 2015) were analysed between the

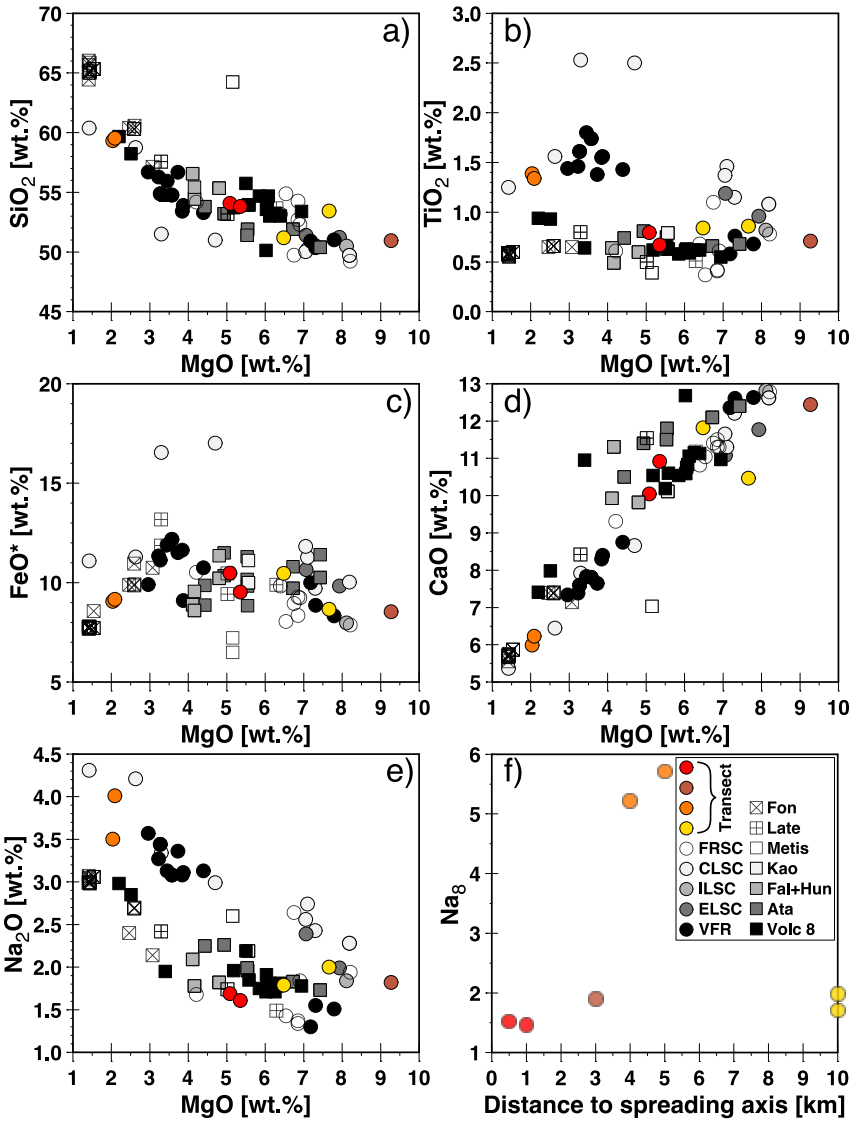

Figure 4.3 *Major element data from the transect across the VFR from Fretzdorff et al. (2006) and Haase et al. (2009) with a) SiO_2, b) TiO_2, c) FeO*, d) CaO, e) Na_2O versus MgO [wt.%] and f) fractionation corrected Na_8 versus distance to the spreading centre in km. Literature data from arc and backarc from (Bach and Niedermann, 1998; Bourdon et al., 1999; Caulfield et al., 2012; Ewart et al., 1994a; Ewart et al., 1998; Ewart and Hawkesworth, 1987; Gill and Williams, 1990; Hawkesworth et al., 1997; Loock et al., 1990; McDermott and Hawkesworth, 1991; Peate et al., 2001; Regelous et al., 1997; Turner et al., 2000; Turner et al., 2012; Turner et al., 1997; Vallier et al., 1991; Vallier, 1985). Abbreviations introduced are those used in Fig. 4.1a.*

sample measurements to check for reproducibility (<1.53% for ND70 and 24.1, 8.54% for ND61) and accuracy (<0.79% for all standards). The sample water data were calculated by the sensitivity factor given by the standard analyses and the sample measurements (Appendix A2). Errors for each sample measurement (n=4) are provided in the Appendix table A6.

4.5 RESULTS

4.5.1 Major and trace elements

The transect data from Fretzdorff et al. (2006) and Haase et al. (2009) show an SiO_2 range of 50.9 to 59.5 wt.% (Figure 4.3a) and are subalkaline basalts to andesites. The MgO contents range from 2.04 to 9.27 wt.%, TiO_2 from 0.67 to 1.39, Na_2O from 1.61 to 4.01 and CaO from 5.99 to 12.44 wt.% (Figure 4.3) (Appendix A2). We do not observe and obvious trend in any of the major elements with distance to the arc. It can generally be observed, that the transect samples lie on the same trend as the general Tonga and Lau Basin literature dataset in a plot of SiO_2 vs MgO (Figure 4.3a). Both in TiO_2 and Na_2O, the transect samples are overlapping with the arc literature data apart from the two most evolved samples which are more comparable to the overall backarc trend (Figure 4.3). In CaO, the transect samples are displaying the same trend as the backarc data (Figure 4.3d). The general H_2O data range between 1.33 (±0.14) and 1.58 (±0.03) wt.% with one outlier of 0.43 (±0.39) wt.% (Figure 4.4).

Selected trace element ratios are plotted against distance to the arc in km (Figure 4.5). The dataset of Figure 4.5 includes all arc and backarc literature data which have existing U-series data. The distances between the arc and backarc range from around 25 to 175 km. Depletion sensitive ratios (e.g., Nb/Yb and Zr/Hf; Figure 4.5a and b) show increasing ratios with increasing distance to the arc (decreasing Longitude), whereas subduction sensitive ratios e.g. Ba/Nb, U/Th and Ce/Yb are decreasing (Figure 4.5). Trace element ratios range from 0.15 to 0.29 in Nb/Yb and 24.9 to 32.0 in Zr/Hf with the lowest ratios at the Valu Fa Ridge and highest ratios observed at the Fonualei Ridge Spreading Centre (FRSC), the northernmost backarc

spreading centre of our dataset (Figure 5). In contrast, Ba/Nb, and U/Th have the highest ratios at Valu Fa Ridge and decrease towards the northern Lau backarc (Figure 4.5). Transect samples range from 108 to 360 and 0.42 to 0.50, respectively, with the other backarc samples reaching down to Ba/Nb 4.76 at the CLSC and U/Th 0.30 at the ELSC, i.e. ratios similar to MORB (Figure 5). Cerium/Yb ranges from 3.03 to 4.93, while the other backarc data show

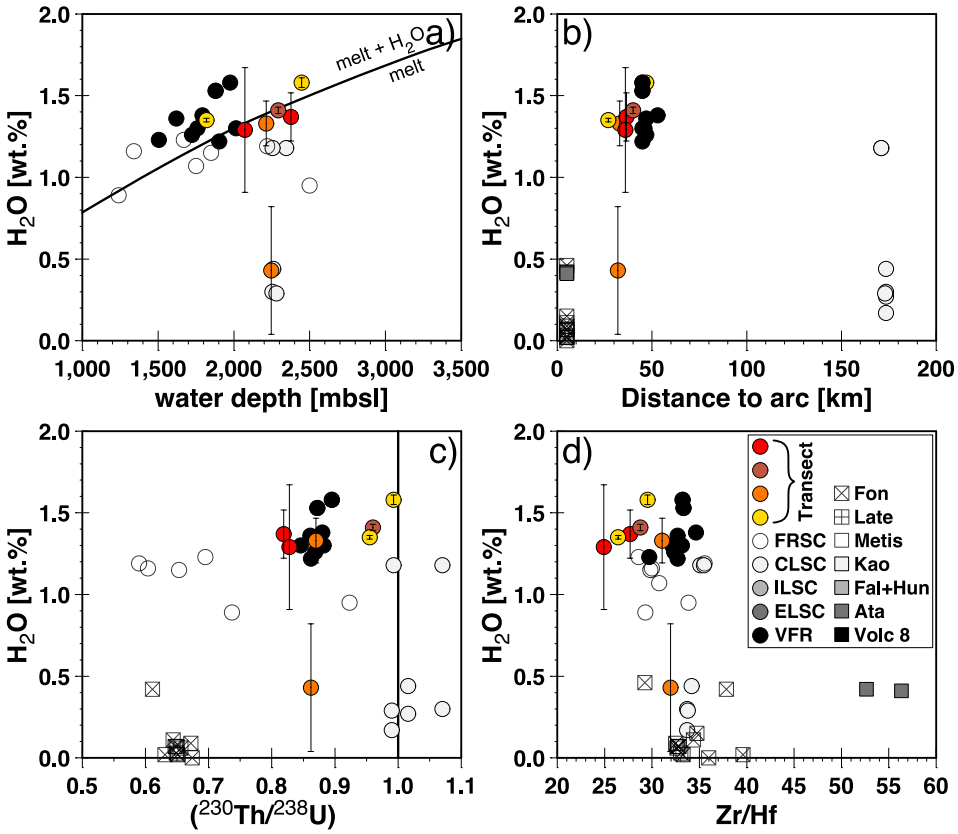

Figure 4.4 *Water data versus a) water depth in mbsl including the water saturation curve from Danyushevsky et al. (1993) showing most samples from the transect are close to the water saturated field (melt + H_2O) suggesting magma degassing, b) ($^{230}Th/^{238}U$) with the equiline where ($^{230}Th/^{238}U$)=1, i.e. in equilibrium, c) distance to the arc in km and d) Zr/Hf. Abbreviations introduced in Fig. 4.1a. References for arc and backarc literature data please see Figure 4.3.*

lower ratios down to 1.62 at the ELSC (Figure 4.5e). On the smaller scale of transect samples, Ba/Th, Ce/Yb and Dy/Yb correlate with the distance to the centre of the spreading axis. The strongest input from a subducting slab component is seen in samples erupted in the axis as opposed to the off-axis lavas.

4.5.2 Lead isotope systematics

Presented Pb-isotope data (Figure 4.6) are from Fretzdorff et al. (2006) and Haase et al. (2009) (Appendix A2). The samples from the transect cover a small range in $^{206}Pb/^{204}Pb$ versus $^{207}Pb/^{204}Pb$ ranging from 18.65 to 18.71 and 15.52 to 15.53, respectively. The $^{208}Pb/^{204}Pb$ ratios display a higher variability with 38.19 to 38.52.

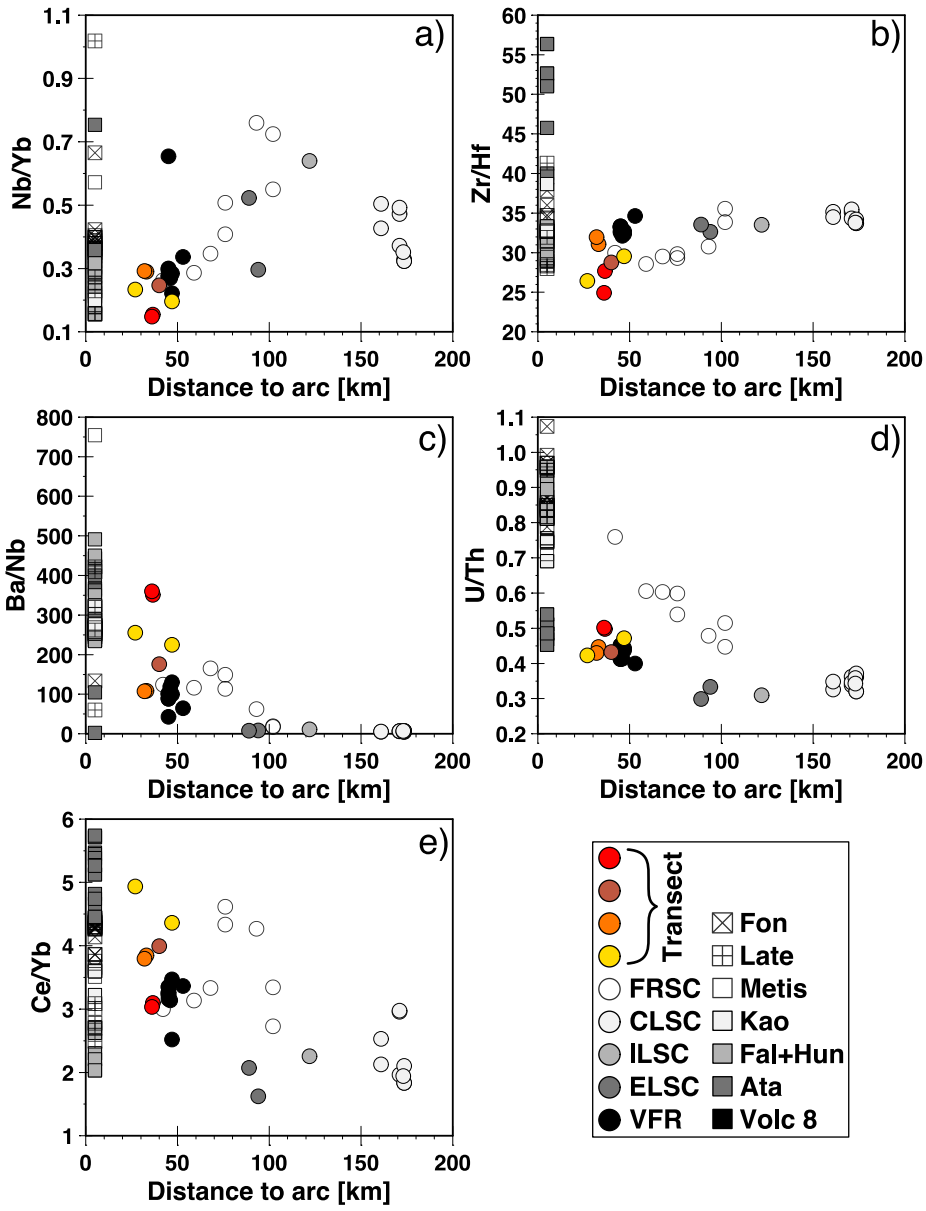

Figure 4.5 *Selected trace element ratios with depletion-sensitive ratios a) Nb/Yb and b) Zr/Hf and subduction sensitive ratios c) Ba/Nb, d) U/Th and e) Ce/Yb versus distance to the arc in km. Abbreviations introduced in Fig. 4.1a. References for arc and backarc literature data please see Figure 4.3.*

4.5.3 Uranium-series systematics

The U-Th-Ra isotopic data are shown in Figure 4.4 and are being compared to literature data from the Lau Basin backarc and Tonga Arc where U-series analyses are available (Bach and Niedermann, 1998; Bourdon et al., 1999; Caulfield et al., 2012; Ewart et al., 1998; Ewart and Hawkesworth, 1987; Ewart et al., 1994b; Gill and Williams, 1990; Hawkesworth et al., 1997; Loock et al., 1990; McDermott and Hawkesworth, 1991; Peate et al., 2001; Regelous et al., 1997; Turner et al., 2000; Turner et al., 2012; Turner et al., 1997; Vallier et al., 1991; Vallier, 1985).

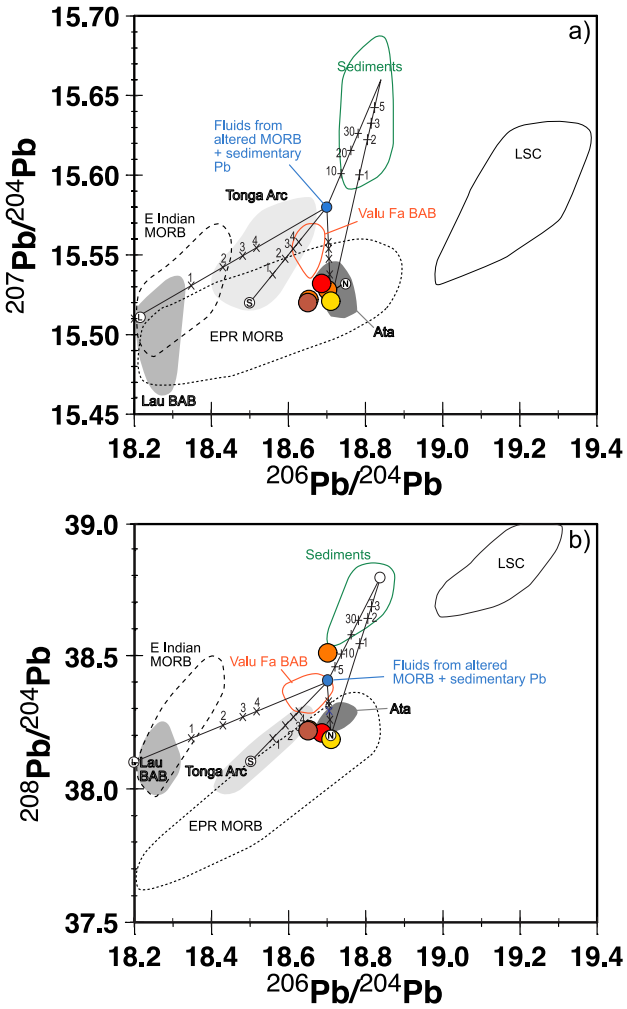

Figure 4.6 *Lead isotope plots including the melting models from Haase et al. (2002), with a) $^{207}Pb/^{204}Pb$ and b) $^{208}Pb/^{204}Pb$ versus $^{206}Pb/^{204}Pb$ showing transect data are distinct from Valu Fa backarc basalts (BAB) with similarities to arc volcano Ata. Transect Pb data are from Fretzdorff et al. (2006) and Haase et al. (2009). Endmembers and calculations from Haase et al. (2002) and references therein.*

Previous work by Peate et al. (2001) implies that the Valu Fa lavas are younger than 8 ka inferred from Ra-excess. Since the eruption ages of the lavas are not exactly known, the (^{226}Ra/^{230}Th) disequilibria are minimal where an unknown amount of decay has occurred since addition of the fluid. Using a total spreading rate of ~40 mm per year for ~23° S with distances of 0.5 to 10 km from the spreading axis (Parson and Wright, 1996) result in ages between 25 to 500 ka for the selected samples if these were erupted along the axis. All samples along the transect display ^{238}U- and ^{226}Ra-excesses. The (^{238}U/^{232}Th) ratios range from 1.01 to 1.22, (^{230}Th/^{232}Th) ranges from 1.09 to 1.19, and thus (^{230}Th/^{238}U) from 0.82 to 0.99 and (^{226}Ra/^{230}Th) from 1.20 to 3.95 in disequilibrium (Figure 4.7). The 2σ errors calculated by the solution standards and the statistical analytical machine error and are given in the Appendix A3. Error bars for (^{226}Ra/^{230}Th) are notably smaller than the symbols.

We do observe that all samples are out of equilibrium in (^{226}Ra/^{230}Th) resulting from fluid addition, and/or melting <8 ka ago (Figure 4.7b). The largest excess in ^{226}Ra display the youngest samples (Figure 4.7d). It shows that fractionation occurs on timescales of < 8 ka. Therefore, (^{230}Th/^{238}U) have not experienced significant decay or in-growth since 8 ka and no age correction is required for our data.

4.6 DISCUSSION

The proximity of the arc and backarc at the southern VFR allows us to decipher the processes of subduction zone input and their impact on the melting regime on a scale of <20 km, i.e. distinguishing between fluid-induced ('wet') versus relatively 'dry' melting (Langmuir et al., 2006) as one traverses across the VFR.

4.6.1 General observations along the VFR

A subset of the samples has previously been discussed by Fretzdorff et al. (2006) who focused on the VFR along-axis magma genesis. The mantle source compositions have previously been

discussed (Escrig et al., 2009; Fretzdorff et al., 2006; Haase et al., 2009; Jenner et al., 1987; Kamenetsky et al., 1997; Peate et al., 2001; Vallier et al., 1991). In short, the VFR samples display both arc and backarc characteristics and result from a combination of Pacific MORB mantle source compositions, fluid influence derived from the subducting slab and sediment

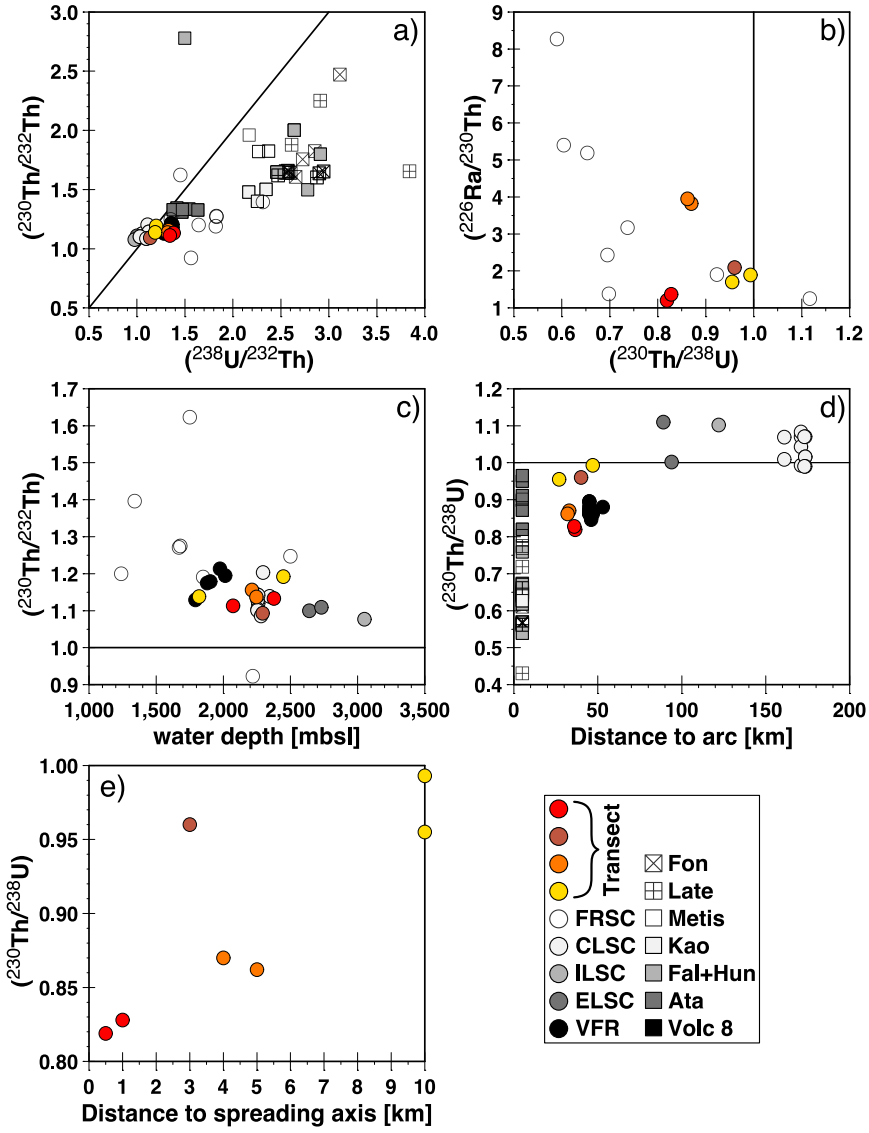

Figure 4.7 *Plots of a) ($^{230}Th/^{232}Th$) versus ($^{238}U/^{232}Th$), c) ($^{226}Ra/^{230}Th$) versus ($^{230}Th/^{238}U$), ($^{230}Th/^{232}Th$) versus d) water depth in mbsl and e) distance to the arc in km. Lines represent equilines where the ratios are in equilibrium (=1). Abbreviations introduced in Fig. 4.1a. References for arc and backarc literature data please see Figure 4.3.*

melts (Figure 6) (Escrig et al., 2009; Fretzdorff et al., 2006; Haase et al., 2009; Haase et al., 2002; Jenner et al., 1987; Peate et al., 2001). The mantle wedge endmember of the southern Lau Basin lavas has $^{87}Sr/^{86}Sr$ ratios of ~0.7028 and $^{143}Nd/^{144}Nd$ isotope ratios of ~0.51307 (Escrig et al., 2009). The southern VFR samples are geochemically comparable to ODP site 839 basalts in the Lau Basin indicating <0.5% sediment contribution to their source (Fretzdorff et al., 2006). Fretzdorff et al. (2006) show that the lava compositions along the transect are dominated by fractionation processes. Major element plots show kinked trends versus MgO (wt.%) indicating changes in fractionation assemblage at about 5 wt.% MgO. Our TiO_2, Na_2O and CaO data show two distinct, parallel trends between the arc and backarc samples (Figure 4.2). Our mafic transect samples have TiO_2 and Na_2O similar to those of the nearby arc lavas but display CaO contents similar to the backarc lavas. The incompatibility of TiO_2 and Na_2O during partial melting (Hirschmann et al., 1999) suggests that the overall melting degree, independent of the melting process, i.e. fluid induced versus decompression melting, between the arc and backarc at the VFR may be comparable. Geophysical data indicate a continuous magma chamber reflector at lower order segments (Wiedicke and Collier, 1993) along the VFR consistent with the presence of a magma chamber underneath the spreading axis. Plots of Ti_8 vs. Fe_8 and Th/Yb vs. Nb/Yb are used for discriminating the different degrees of melting in the Lau Basin area (Jenner et al., 2012; Taylor and Martinez, 2003; Zhang et al., 2019). Using these diagrams for our transect data, the primitive samples indicate very high degrees of melting with Ti_8 <1 and Nb/Yb <0.3 (Figure 4.5a) with Th/Yb <0.3. Comparing Na_8 of the transect to data from Ata island (Figure 4.2f), suggests that the degrees of partial melting along the transect exceeds those observed at the arc (Fretzdorff et al., 2006). Fretzdorff et al. (2006) also discuss partial melting degrees of up to 25% for the southern VFR lavas. The transect glasses were sampled at seamounts south of the VFR tip on older crust (Fretzdorff et al., 2006; Haase et al., 2009). The similarities between the samples more distant from the spreading axis and the spreading axis itself indicate an unchanging lava evolution with time (Haase et al., 2009). Geochemical analyses of the transect show a similarity to VFR lavas (Figure 4.2 and

4.8) but also exceeding the subduction input observed in e.g. higher K_2O contents or $(Dy/Yb)_N$ (Haase et al., 2009). It is shown, that the higher melting volume caused by the subduction input leads to short timescales of magma storage in the chambers shown by predominantly primitive (predominantly >6 MgO wt.%) lava compositions along the transect which is contrary to processes seen along propagating ocean rifts or mature spreading centres (Haase et al., 2009).

Thus, we consider the shallow level crustal fractionation processes along the VFR and ELSC to be comparable to those commonly observed along MORs, and degrees of partial melting between the arc and backarc to be on the same order of magnitude, however, distinct differences in source composition will contribute to the melting regime to different extents, the significance of which we discuss in more detail below.

4.6.2 Mantle wedge depletion and subduction zone input from trace element data

Depletion sensitive trace element ratios (e.g. Nb/Yb <0.5, Nb/La <0.25, Zr/Hf <30, or Zr/Yb <20) indicate a decreasing degree of depletion with increasing distance to the arc, i.e. lavas erupted >150 km from the arc have patterns comparable to mid-ocean ridge basalts (MORB) (Pearce et al., 1994) while those at the southern VFR are slightly more depleted (Figure 4.3). The increasing degree of depletion closer to the arc suggests that the mantle source in the southern VFR may have experienced prior melt extraction but the overall degree of depletion suggest that these changes may be small.

The subduction input to the Lau Basin lavas involves fluids derived from altered oceanic crust (AOC) and fluids and/or melts from sediments, and fluids from the subducting Louisville seamount chain (LSC) (Timm et al., 2013; Turner and Hawkesworth, 1997). The subducting slab contribution to the Lau Basin mantle sources has previously been discussed in Escrig et al. (2009), who determined an increasing subduction input with decreasing distance to the arc

from north to south, however, changes in subduction signatures also occur over small distances not related to the distance to the arc (Escrig et al., 2009).

Along the VFR elevated U/Nb, Ba/Nb and Ce/Pb imply an elevated fluid input at the southernmost ridge (Fretzdorff et al., 2006). The transect samples follow the VFR trend with higher ratios indicating an even higher subduction input (Figure 4.3c, d). The subduction endmember along the VFR resembles that from Ata island located at the Tofua Arc in trace element and isotopic ratios with elevated $^{208}Pb/^{204}Pb$ isotopically dominated by the subducting LSC (Escrig et al., 2009).

The transect samples with the strongest degree of depletion also display the strongest subduction zone signature likely a result that the more depleted source compositions will be relatively more affected by the enriched subduction components. Generally, we would expect a decreasing trend of depletion and subduction input with increasing distance from the arc. While the entire backarc dataset along the VFR and NELSC displays such variability we do not observe a systematic trend across the VFR (Figure 4.3e, f). Both Zr/Hf and U/Th do not correlate with distance from arc. At about 36 km distance from the arc, i.e. closest to the spreading axis (red circle symbols), the samples have the lowest Zr/Hf (also Nb/La; not shown), but highest U/Th and Ba/Nb (Figure 4.5).

In subduction zone environments, water contents are expected to be correlated with fluid-sensitive trace element ratios. Due to the small range of just 0.3 wt.% difference of the transect samples along with relatively large errors, potential correlations of water content with e.g versus Zr/Hf and distance from the arc or spreading axis are not observed (Figure 4.4). A plot of water contents versus water depth in mbsl (meter below sea level) (Figure 4.4a) shows, that all samples lie close to or in the melt + H2O field divided by the water-saturation curve from Danyushevsky et al. (1993). Samples plot close or in the water-saturated field (i.e. melt + H_2O) and therefore display degassing. Initial water contents are expected to be higher. We generally

observe the highest H_2O contents (~1.5 wt.%) along the transect at the largest distance from the arc independent of distance to the spreading axis and at Benioff Zone depths of 125 km (Hayes et al., 2012) depths at which the slab surface temperature will be ~800°C (van Keken et al., 2011). The release of H_2O from the subducting slab in the Tongan arc has been estimated to peak at 100-150 km depth in agreement with our H_2O data (van Keken et al., 2011). A comparison with H_2O data along the VFR does show similar contents (1.2 to 1.6 wt.%) at about 45 km from the arc where our sample with the highest water content is located (Figure 4.5b). Samples between 50 and 175 km distance to the arc show decreasing water contents (Figure 4.4b) (Loock et al., 1990; Peate et al., 2001).

Samples with relatively lower Ba/Nb relative to the samples closest to the spreading axis ratios occur both closer and more distant to the arc (Figure 4.5e). The samples with the most elevated Ba/Nb ratios (225KD and 79DR-01) also display the highest Nb concentrations of >1 ppm, and elevated Nb/La and Nb/Yb (>0.2) ratios indicating that they are originating from a source less depleted than those closer and more distant to the arc. These samples are also those located closest to the spreading axis (Figure 4.6), suggesting that the central VFR axis may be fed by mantle sources closer in composition to normal depleted mantle than the off-axis lavas. The preservation of different source signatures towards the centre of the ridge axis suggests that the more enriched, subduction related signatures may rather be preserved in the off-axis melts, similar to observations on normal MORs (Niu and Batiza, 1991; Standish and Sims, 2010; Turner et al., 2011).

4.6.3 Melting regimes

The occurrence of subduction related signatures at the VFR may either reflect processes from the subducting slab, i.e. with increasing distance from the arc the geochemical signatures will mirror the changes in metamorphic processes in the subducting slab (Tollstrup et al., 2010), or mixing of sources and/or melts from the arc and backarc, i.e. overlapping melting zones (Sleeper and Martinez, 2014; Zha et al., 2014). In both cases the formation of subduction zone

mélanges will add additional complexity to the geochemical signatures erupted on the surface (Marschall and Schumacher, 2012). Here, we use the combined U-Th-Ra disequilibria and H_2O to further understand the changes in melting regime with increasing distance to the arc and spreading axis.

4.6.3.1 Influence of sediment melts

Comparing Pb-isotope ratios to calculated models from Haase et al. (2002), we observe (Figure 4.6) that the transect samples overlap with the field for Ata and S' Havre Trough samples are derived from altered MORB with little but significant sediment contribution (<1%) from Pacific sediment. The transect samples differ from the VFR samples in having lower Pb isotope ratios (Figure 4.6) and display stronger similarities to the arc samples (Haase et al., 2009; Sleeper and Martinez, 2014).

We do observe a positive correlation of heavy rare earth element (HREE, e.g., Dy/Yb) ratios with ($^{230}Th/^{238}U$) (Figure 4.8a) across the VFR. Elevated HREE could be indicative for the involvement of residual garnet during partial melting (Robinson and Wood, 1998). Since Th is more incompatible than U in the presence of garnet (Beattie, 1993), Dy/Yb and ($^{230}Th/^{238}U$) are correlated positively. In addition, we observe similar correlations between the light rare earth element (LREE) and HREE ratios (e.g., Ce/Yb) and U-Th disequilibria across the VFR (Figure 4.8b). Our samples from the VFR display elevated ($^{230}Th/^{238}U$) disequilibria when being compared to existing data from the region. In a plot of Dy/Dy* (Dy Dy*= $Dy_N/La_N^{4/13}*Yb_N^{9/13}$; formula by Davidson et al. (2012)) versus ($^{230}Th/^{238}U$) disequilibria (Figure 4.8c) we do observe a positive correlation close to equilibrium where elevated Dy/Dy* have been interpreted to represent a distinct LREE enrichment due to the addition of sediment melts (Davidson et al., 2012). Temperatures of ~800°C at 150 km depth (van Keken et al., 2011) are high enough to cause melting of sediment from the subducting slab. These sediment melts influence the melts (Hermann and Spandler, 2008) leading to a decrease in Dy/Dy* and significantly lower

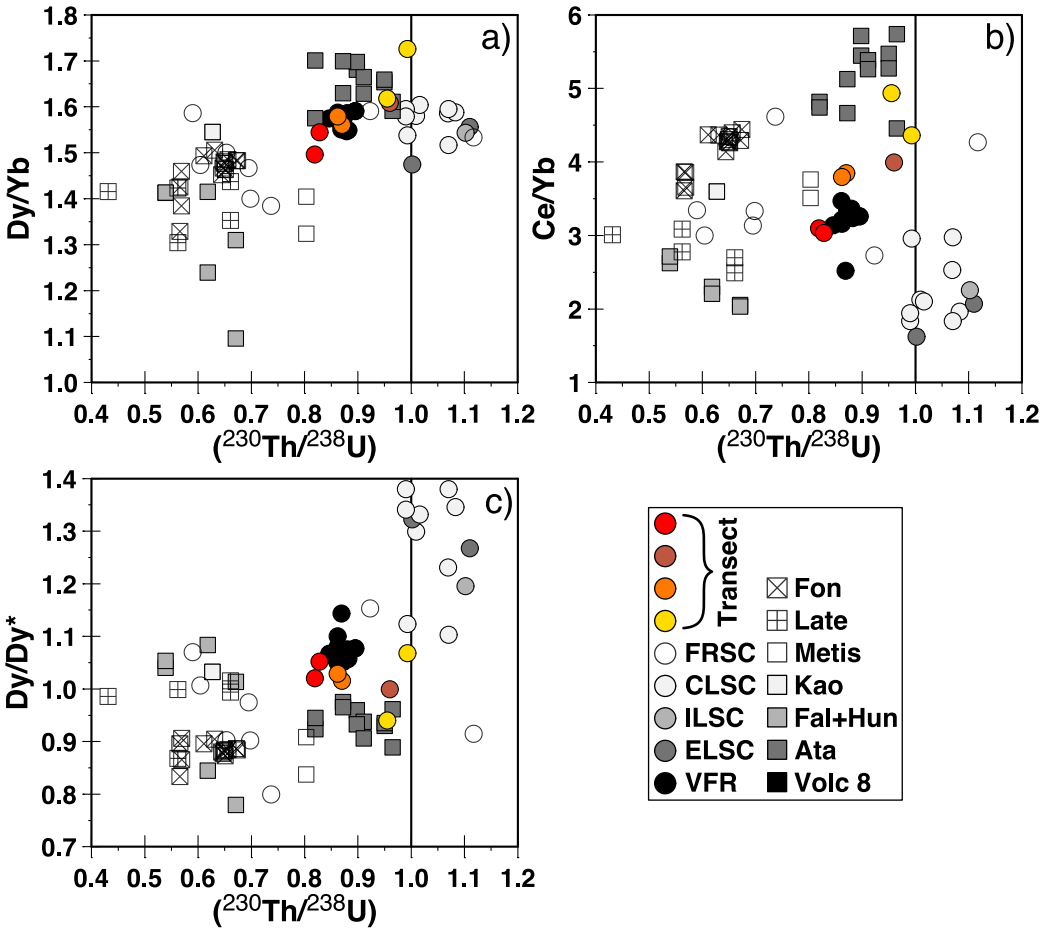

Figure 4.8 *Selected trace element ratios versus U-series with a) Dy/Yb, b) Ce/Yb, and c) Dy/Dy* calculated after the formula of (Davidson et al., 2012) with CI compositions of Lyubetskaya and Korenaga (2007) versus ($^{230}Th/^{238}U$) with equilines where ($^{230}Th/^{238}U$) =1 (in equilibrium). Abbreviations introduced in Fig. 4.1a. References for arc and backarc literature data please see Figure 4.3.*

($^{238}U/^{232}Th$) ratios (Peate and Hawkesworth, 2005), i.e. as seen in the samples close to ($^{230}Th/^{238}U$) equilibrium (Figure 4.8). This is also supported by the trends seen in Pb-isotopes (Figure 4.6).

4.6.3.2 Style of melting along the E-W transect and implications for melting models

Both, U and Th are highly incompatible during mantle melting and their isotopic equilibrium is not influenced by batch or fractional crystallisation (McGee et al., 2011). Uranium behaves fluid-mobile under oxidizing conditions which leads to excesses of (^{238}U) over (^{230}Th) along altered oceanic crust fluid-influenced arcs (Turner and Hawkesworth, 1997). In addition, the

shorter lived daughter isotope of ^{230}Th, ^{226}Ra is similarly fluid mobile to Ba (Bourdon et al., 2003a; Elliott, 2004) allowing it to trace the addition of fluids to the mantle wedge at timescales of <8 ka (Turner et al., 2001). Thus, fluid fluxed melts have commonly been associated with larger (^{238}U) excesses (^{230}Th/^{238}U <<0.9) and elevated (^{226}Ra/^{230}Th >4) in zero-age lavas (Turner et al., 2003b). Contrastingly, simple decompression melting of relatively dry MOR mantle will result in (^{230}Th) excesses (^{230}Th/^{238}U >0.9 to >1). However, Beier et al. (2010) have shown that dynamic decompression melting of subduction modified, oxidized mantle may lead to (^{238}U) excesses but leaving ^{226}Ra disequilibria unchanged.

Generally, there are several models for the different melting regimes in backarcs. Langmuir et al. (2006) conclude, that the backarc melting regime can be divided into a wet subduction influenced part on the arc side and a dry, MORB-like side further away from the arc which interact gradational. A similar model is proposed by Bézos et al. (2009) including a damp component with a composition between the wet component and E-MORB. Dunn and Martinez (2011) discuss that the wet component is more likely to be observed in backarcs due to their lower viscosity and that the dry highly viscous component is only involved in the magma transport to the spreading axis when the ridge axis is completely above the dry source region.

The significant (^{238}U) excesses (Figure 4.7) as well as the increased Ba/Nb and U/Th ratios (Figure 4.5) derived from the subducting slab generally let us conclude that the southern VFR samples are resulting from fluid-fluxed rather than decompression melting. If a model of wet versus dry side melting would be applicable at the VFR, the arc influence would be expected to decrease. We observe relatively low U-excesses of <1.2 (but with significant ^{226}Ra disequilibria) closest and farthest away from the arc, while samples erupted at the spreading axis (31 to 37 km distance to the arc) show higher U-excesses >1.3 (Figure 4.7).

We therefore see different degrees of fluid influence which are not gradual with the distance from the arc on a small scale of <25 km. The gradual trend is also not observed in the water

contents (Figure 4.4) and fluid-sensitive trace element ratios (Figure 4.5). We conclude that the Langmuir et al. (2006) may not be applicable to backarc regimes that are <50 km distance from the active arc due to a complex interaction of the different melting regimes between the arc and backarc. A model for the mantle wedge control by Sleeper and Martinez (2014) shows three main mantle domains with different degrees of depletion and arc-influence similar to Langmuir et al. (2006) but additionally influenced by small, hydrated melt diapirs and sediment-rich diapirs as proposed by Haase et al. (2009). In this context, we propose that much of the melting regime is influenced by the spreading axis focusing melts into the ridge axis. An overlap of the melting zones between the arc and backarc at these distances results in a sufficient homogenisation of the magmas (Sleeper and Martinez, 2014; Zha et al., 2014).

4.7 CONCLUSIONS

This study combines literature data from the entire Lau Basin with newly analysed U-series disequilibria and water data from an E-W transect along the southernmost tip of the VFR to investigate the subduction influence on the melting regime on different spatial scales. We can show that the melting zone model proposed by Langmuir et al. (2006) might be applicable for changes of the melting zones along the entire Lau Basin but not at spreading centres of <50 km distance from the arc. Lavas from the E-W transect across the VFR do not show a gradual decrease in subduction indices, i.e. water contents, ($^{230}Th/^{238}U$) or fluid mobile trace element ratios, with increasing distances from the arc. Instead, the melting regime in this area is strongly dominated by the spreading axis. We conclude that an overlap of the melting zones of arc and backarc like previously indicated by Zhao et al. (1997) in this region leads to mixing of the sources and melts of arc and backarc from <50 km distance from the arc.

Further transect-like profiles from the northern part of the Lau Basin (e.g. Fonualei Spreading Centre) may improve our understanding on small-scale changes in subduction systems.

4.8 ACKNOWLEDGEMENTS

We thank Captains, crews and scientists during the cruises SO67 and SO167 for sampling. This publication was funded by the projects BE 4459/8-1 and BR 5297/2-1 BISMArc from the Deutsche Forschungsgemeinschaft (DFG). We thank T. Ireland at ANU for his help and support during the water analysis.

4.9 SUPPLEMENT

All data analysed for this chapter are shown in tables A2 and A3 of the Appendix along with standard analyses and analytical errors for water and trace element analyses in tables A5 and A6. Major element and Sr-Nd-Pb isotope iterature data of the transect from Fretzdorff et al., 2006 and Haase et al., 2009 are presented in table A2.

5 SUMMARY

Despite the Lau Basin has been subject to many previous publications, there are still many undersampled areas and the evolution of this backarc basin is not fully understood. In this thesis, I present new insight into the complexity of backarcs of the Tonga subduction system which contributes to a better understanding of the Lau Basin and other backarc systems.

5.1 SOURCE VARIABILITY IN THE LAU BASIN

Sources influencing the backarc magmas along the Lau Basin differ with distance relative to the arc, the varying sediment input along the basin, the mantle sources and the subduction components fertilizing the mantle wedge (Bézos et al., 2009; Boespflug et al., 1990; Davis et al., 1986; Dril et al., 1997; Escrig et al., 2009; Escrig et al., 2012; Ewart et al., 1998; Falloon et

al., 1992; Falloon et al., 2007; Hawkins, 1995; Pearce et al., 1994; Price et al., 2014; Tian et al., 2011).

Here, I can present a complete dataset from the North-East Lau Spreading Centre which previously remained nearly unsampled. In order to disentangle the complex melting processes from a highly heterogeneous mantle, I considered major and trace elements, and Sr-Nd-Pb isotopes along with water contents.

The southernmost seamounts represent the continuation of the NELSC which shows that the spreading continues to propagate towards the south. Despite the very high spreading rates along the northern Lau Basin mantle heterogeneities are still detectable using trace element variations. Radiogenic isotope ratios show that two enriched sources influence the area. The rear-arc shows signatures of the subducted Louisville Seamount Chain which was previously thought to be restricted to the arc area of Niuatoputapu and Tafahi (Beier et al., 2017). Moreover, a second enriched OIB source influences this area likely derived from the Samoan hotspot in the north.

The southern part of the basin, i.e. the Valu Fa Ridge, shows sediment and fluid inputs and isotopic signatures show that these samples are highly comparable to the adjacent arc volcano Ata. Previous studies (Fretzdorff et al., 2006; Haase et al., 2009) showed that this area of the backarc is underlain by Pacific-type mantle influenced by fluids from altered oceanic crust and subducted sediments.

5.2 MELTING REGIMES AND MELT FLOW IN THE LAU BASIN

The NELSC and DR are located in immediate vicinity, whereas the DR forms the transition between backarc (NELSC) and the rear-arc volcano Niuatahi. Based on the structural connection, previous assumptions included a direct interaction between the rear-arc and the NELSC by e.g. material flow along the DR’s underlying mantle. towards the NELSC with the

DR located in between. Geochemically, such material flow towards NELSC would result in an increased subduction signature south of the incision of the DR. As opposed to previous assumptions, however, increased signatures from slab fluids are absent at the southern DR. Instead, lavas from NELSC and the DR display different mantle source signatures. I showed that the source differences between these two magmatic features are the result of distinct melting zones that occur on small spatial scales with only limited evidence of interaction in between. Structurally, the DR forms the transition between the rear arc, however, extensive material flow between rear-arc and NELSC can be excluded.

The melting zone model by Langmuir et al. (2006) for the Lau Basin proposes two melting zones: a wet, arc-influenced zone on the arc-facing side and a dry zone on the arc-averted side. On the basis of U-series and water concentrations of fresh volcanic glasses sampled along an E-W transect at the southernmost Valu Fa Ridge, I can show that the model by Langmuir et al. (2006) does not apply on scales of <50 km distance to the volcanic arc. Uranium-series systematics and water concentrations do not show a gradual decrease of subduction influence with increasing distance to the arc as would be expected. Instead, my observations favour extensive mixing like proposed by Zhao et al. (1997) of the melting zones that occurs in areas of <50 km distance from the arc. The mixing between the melting zones results in the overprint of a gradually changing subduction slab signature.

6 REFERENCES

Anderson, M. O., Norris-Julseth, C., Rubin, K. H., Haase, K. M., Hannington, M. D., Baxter, A. T., and Stewart, M., 2020, Geometry and Evolution of Wrench Tectonics in the NE Lau Basin: ESSOAR (Earth and Space Science Open Archive).

Arculus, R., 1994, Aspects of magma genesis in arcs: Lithos, v. 33, no. 1-3, p. 189-208.

Asimow, P. D., Hirschmann, M., Ghiorso, M., O'Hara, M., and Stolper, E., 1995, The effect of pressure-induced solid-solid phase transitions on decompression melting of the mantle: Geochimica et Cosmochimica Acta, v. 59, no. 21, p. 4489-4506.

Bach, W., Hegner, E., Erzinger, J., and Satir, M., 1994, Chemical and isotopic variations along the superfast spreading East Pacific Rise from 6 to 30 S: Contributions to Mineralogy and Petrology, v. 116, no. 4, p. 365-380.

Bach, W., and Niedermann, S., 1998, Atmospheric noble gases in volcanic glasses from the southern Lau Basin: origin from the subducting slab?: Earth and planetary science letters, v. 160, no. 3, p. 297-309.

Baker, E. T., Walker, S. L., Massoth, G. J., and Resing, J. A., 2019, The NE Lau Basin: Widespread and abundant hydrothermal venting in the back-arc region behind a superfast subduction zone: Frontiers in Marine Science, v. 6, p. 382.

Bassett, D., Kopp, H., Sutherland, R., Henrys, S., Watts, A. B., Timm, C., Scherwath, M., Grevemeyer, I., and de Ronde, C. E., 2016, Crustal structure of the Kermadec arc from MANGO seismic refraction profiles: Journal of Geophysical Research: Solid Earth, v. 121, no. 10, p. 7514-7546.

Baxter, A., Hannington, M. D., Stewart, M., Emberley, J., Breker, K., Krätschell, A., Petersen, S., Brandl, P. A., Klischies, M., and Mensing, R., 2020, Shallow seismicity and the classification of structures in the Lau back-arc basin: Geochemistry, Geophysics, Geosystems, p. e2020GC008924.

Beattie, P., 1993, Uranium-thorium disequilibria and partitioning on melting of garnet peridotite: Nature (London), v. 363, no. 6424, p. 63-65.

Bebout, G. E., 2007, Metamorphic chemical geodynamics of subduction zones: Earth and Planetary Science Letters, v. 260, no. 3-4, p. 373-393.

Bebout, G. E., Bebout, A. E., and Graham, C. M., 2007, Cycling of B, Li, and LILE (K, Cs, Rb, Ba, Sr) into subduction zones: SIMS evidence from micas in high-P/T metasedimentary rocks: Chemical Geology, v. 239, no. 3-4, p. 284-304.

Beier, C., Brandl, P. A., Lima, S. M., and Haase, K. M., 2018, Tectonic control on the genesis of magmas in the New Hebrides arc (Vanuatu): Lithos, v. 312, p. 290-307.

Beier, C., Turner, S. P., Haase, K. M., Pearce, J. A., Münker, C., and Regelous, M., 2017, Trace element and isotope geochemistry of the northern and central Tongan islands with an emphasis on the genesis of high Nb/Ta signatures at the northern volcanoes of Tafahi and Niuatoputapu: Journal of Petrology, v. 58, no. 6, p. 1073-1106.

Beier, C., Turner, S. P., Sinton, J. M., and Gill, J. B., 2010, Influence of subducted components on back-arc melting dynamics in the Manus Basin: Geochemistry, Geophysics, Geosystems, v. 11, no. 6.

Beier, C., Vanderkluysen, L., Regelous, M., Mahoney, J. J., and Garbe-Schönberg, D., 2011, Lithospheric control on geochemical composition along the Louisville Seamount Chain: Geochemistry, Geophysics, Geosystems, v. 12, no. 9.

Bevis, M., Taylor, F. W., Schutz, B. E., Recy, J., Isacks, B., Helu, S., Singh, R., Kendrick, E., Stowell, J., and Taylor, B., 1995, Geodetic observations of very rapid convergence and back-arc extension at the Tonga arc: Nature, v. 374, no. 6519, p. 249-251.

Bézos, A., Escrig, S., Langmuir, C. H., Michael, P. J., and Asimow, P. D., 2009, Origins of chemical diversity of back-arc basin basalts: A segment-scale study of the Eastern Lau Spreading Center: Journal of Geophysical Research: Solid Earth, v. 114, no. B6.

Bird, P., 2003, An updated digital model of plate boundaries: Geochemistry, Geophysics, Geosystems, v. 4, no. 3.

Bloomer, S. H., Ewart, A., Hergt, J. M., and Bryan, W. B., 1994, 38. Geochemistry and origin of igneous rocks from the outer Tonga forearc (Site 841): Hawkins J., Parson L., Allan J., et al, p. 625-646.

Blundy, J., and Wood, B., 2003, Mineral-melt partitioning of uranium, thorium and their daughters: Reviews in Mineralogy and Geochemistry, v. 52, no. 1, p. 59-123.

Boespflug, X., Dosso, L., Bougault, H., and Joron, J.-L., 1990, Trace element and isotopic (Sr, Nd) geochemistry of volcanic rocks from the Lau Basin: Geologisches Jahrbuch, v. 92, p. 503-516.

Bourdon, B., Turner, S., and Allègre, C., 1999, Melting dynamics beneath the Tonga-Kermadec island arc inferred from 231Pa-235U systematics: Science, v. 286, no. 5449, p. 2491-2493.

Bourdon, B., Turner, S., and Dosseto, A., 2003a, Dehydration and partial melting in subduction zones: Constraints from U-series disequilibria: Journal of Geophysical Research: Solid Earth, v. 108, no. B6.

Bourdon, B., Turner, S., Henderson, G. M., and Lundstrom, C. C., 2003b, Introduction to U-series geochemistry: Reviews in mineralogy and geochemistry, v. 52, no. 1, p. 1-21.

Bourdon, B., Turner, S. P., Henderson, G. M., and Lundstrom, C. C., 2003c, Introduction to U-series geochemistry, Uranium-series geochemistry, Volume 52;: Washington, DC, United States, Mineralogical Society of America and Geochemical Society, p. 1-21.

Brandl, P. A., Beier, C., Regelous, M., Abouchami, W., Haase, K. M., Garbe-Schönberg, D., and Galer, S. J., 2012, Volcanism on the flanks of the East Pacific Rise: Quantitative

constraints on mantle heterogeneity and melting processes: Chemical Geology, v. 298, p. 41-56.

Cagnioncle, A. M., Parmentier, E., and Elkins-Tanton, L. T., 2007, Effect of solid flow above a subducting slab on water distribution and melting at convergent plate boundaries: Journal of Geophysical Research: Solid Earth, v. 112, no. B9.

Cañón-Tapia, E., and Walker, G. P., 2004, Global aspects of volcanism: the perspectives of "plate tectonics" and "volcanic systems": Earth-Science Reviews, v. 66, no. 1-2, p. 163-182.

Caulfield, J., Turner, S., Arculus, R., Dale, C., Jenner, F., Pearce, J., Macpherson, C., and Handley, H., 2012, Mantle flow, volatiles, slab-surface temperatures and melting dynamics in the north Tonga arc–Lau back-arc basin: Journal of Geophysical Research: Solid Earth, v. 117, no. B11.

Chauvel, C., and Blichert-Toft, J., 2001, A hafnium isotope and trace element perspective on melting of the depleted mantle: Earth and Planetary Science Letters, v. 190, no. 3-4, p. 137-151.

Chauvel, C., McDonough, W., Guille, G., Maury, R., and Duncan, R., 1997, Contrasting old and young volcanism in Rurutu Island, Austral chain: Chemical Geology, v. 139, no. 1-4, p. 125-143.

Cheng, Q., Park, K. H., Macdougall, J., Zindler, A., Lugmair, G., Staudigel, H., Hawkins, J., and Lonsdale, P., 1987, Isotopic evidence for a hotspot origin of the Louisville seamount chain: Seamounts, islands, and atolls, v. 43, p. 283-296.

Clague, D., Caress, D., Rubin, K., and Paduan, J., 2010, The 2008 puipui eruption and morphology of the northeast lau spreading center between maka and tafu: AGUFM, v. 2010, p. T11E-03.

Compston, W., and Oversby, V., 1969, Lead isotopic analysis using a double spike: Journal of Geophysical Research, v. 74, no. 17, p. 4338-4348.

Conder, J. A., Wiens, D. A., and Morris, J., 2002, On the decompression melting structure at volcanic arcs and back-arc spreading centers: Geophysical Research Letters, v. 29, no. 15, p. 17-11-17-14.

Condomines, M., Gauthier, P.-J., and Sigmarsson, O., 2003, Timescales of magma chamber processes and dating of young volcanic rocks: Reviews in Mineralogy and Geochemistry, v. 52, no. 1, p. 125-174.

Cooper, L. B., Plank, T., Arculus, R. J., Hauri, E. H., Hall, P. S., and Parman, S. W., 2010, High-Ca boninites from the active Tonga Arc: Journal of Geophysical Research: Solid Earth, v. 115, no. B10.

Cross, T. A., and Pilger, R. H., 1982, Controls of subduction geometry, location of magmatic arcs, and tectonics of arc and back-arc regions: Geological Society of America Bulletin, v. 93, no. 6, p. 545-562.

Dale, C. W., Macpherson, C. G., Pearson, D. G., Hammond, S. J., and Arculus, R. J., 2012, Inter-element fractionation of highly siderophile elements in the Tonga Arc due to flux melting of a depleted source: Geochimica et Cosmochimica Acta, v. 89, p. 202-225.

Danyushevsky, L., Falloon, T., Sobolev, A., Crawford, A., Carroll, M., and Price, R., 1993, The H 2 O content of basalt glasses from Southwest Pacific back-arc basins: Earth and Planetary Science Letters, v. 117, no. 3, p. 347-362.

Danyushevsky, L. V., Sobolev, A. V., and Falloon, T. J., 1995, North Tongan high-Ca boninite petrogenesis: The role of Samoan plume and subduction zone-transform fault transition: Journal of Geodynamics, v. 20, no. 3, p. 219-242.

Davidson, J., Turner, S., and Plank, T., 2012, Dy/Dy*: variations arising from mantle sources and petrogenetic processes: Journal of Petrology, v. 54, no. 3, p. 525-537.

Davies, J. H., and Stevenson, D. J., 1992, Physical model of source region of subduction zone volcanics: Journal of Geophysical Research: Solid Earth, v. 97, no. B2, p. 2037-2070.

Davis, A., Clague, D., and Morton, J., 1986, Volcanic glass compositions from two spreading centers in Lau Basin, South Pacific Ocean: US Geological Survey, 2331-1258.

de Ronde, C. E., Faure, K., Bray, C. J., Chappell, D. A., and Wright, I. C., 2003, Hydrothermal fluids associated with seafloor mineralization at two southern Kermadec arc volcanoes, offshore New Zealand: Mineralium Deposita, v. 38, no. 2, p. 217-233.

Dosseto, A., Turner, S., and Douglas, G., 2006, Uranium-series isotopes in colloids and suspended sediments: timescale for sediment production and transport in the Murray–Darling River system: Earth and Planetary Science Letters, v. 246, no. 3-4, p. 418-431.

Dosso, L., Bougault, H., Beuzart, P., Calvez, J.-Y., and Joron, J.-L., 1988, The geochemical structure of the South-East Indian ridge: Earth and Planetary Science Letters, v. 88, no. 1-2, p. 47-59.

Dril, S., Kuzmin, M., Tsipukova, S., and Zonenshain, L., 1997, Geochemistry of basalts from the western Woodlark, Lau and Manus basins: implications for their petrogenesis and source rock compositions: Marine Geology, v. 142, no. 1-4, p. 57-83.

Duncan, R. A., 1985, Volcanic episodes at'Eua, Tonga Islands.

Dunn, R. A., and Martinez, F., 2011, Contrasting crustal production and rapid mantle transitions beneath back-arc ridges: Nature, v. 469, no. 7329, p. 198-202.

Elliott, T., 2004, Tracers of the Slab: Inside the Subduction Factory, p. 23-45.

Embley, R. W., and Rubin, K. H., 2018, Extensive young silicic volcanism produces large deep submarine lava flows in the NE Lau Basin: Bulletin of Volcanology, v. 80, no. 4, p. 36.

Escrig, S., Bézos, A., Goldstein, S., Langmuir, C., and Michael, P., 2009, Mantle source variations beneath the Eastern Lau Spreading Center and the nature of subduction components in the Lau basin–Tonga arc system: Geochemistry, Geophysics, Geosystems, v. 10, no. 4.

Escrig, S., Bézos, A., Langmuir, C., Michael, P., and Arculus, R., 2012, Characterizing the effect of mantle source, subduction input and melting in the Fonualei Spreading Center, Lau Basin: Constraints on the origin of the boninitic signature of the back-arc lavas: Geochemistry, Geophysics, Geosystems, v. 13, no. 10.

Ewart, A., Brothers, R., and Mateen, A., 1977, An outline of the geology and geochemistry, and the possible petrogenetic evolution of the volcanic rocks of the Tonga-Kermadec-New Zealand island arc: Journal of volcanology and geothermal research, v. 2, no. 3, p. 205-250.

Ewart, A., Bryan, W., Chappell, B., and Rudnick, R., Regional geochemistry of the Lau-Tonga arc and backarc systems, *in* Proceedings Proceedings of the Ocean Drilling Program. Scientific Results1994a, Volume 135, Ocean Drilling Program, p. 385-425.

Ewart, A., Collerson, K., Regelous, M., Wendt, J., and Niu, Y., 1998, Geochemical evolution within the Tonga–Kermadec–Lau arc–back-arc systems: the role of varying mantle wedge composition in space and time: Journal of Petrology, v. 39, no. 3, p. 331-368.

Ewart, A., and Hawkesworth, C., 1987, The Pleistocene-Recent Tonga-Kermadec arc lavas: interpretation of new isotopic and rare earth data in terms of a depleted mantle source model: Journal of petrology, v. 28, no. 3, p. 495-530.

Ewart, A., Hergt, J., and Hawkins, J., 29. Major element, trace element, and isotope (Pb, Sr, and Nd) geochemistry of Site 839 basalts and basaltic andesites: implications for arc volcanism, *in* Proceedings Proceedings of the Ocean Drilling Program, Scientific Results1994b, Volume 135, p. 519.

Falloon, T., Malahoff, A., Zonenshaina, L., and Bogdanova, Y., 1992, Petrology and geochemistry of back-arc basin basalts from Lau Basin spreading ridges at 15, 18 and 19 S: Mineralogy and Petrology, v. 47, no. 1, p. 1-35.

Falloon, T. J., Danyushevsky, L. V., Crawford, T. J., Maas, R., Woodhead, J. D., Eggins, S. M., Bloomer, S. H., Wright, D. J., Zlobin, S. K., and Stacey, A. R., 2007, Multiple mantle plume components involved in the petrogenesis of subduction-related lavas from the northern termination of the Tonga Arc and northern Lau Basin: Evidence from the

geochemistry of arc and backarc submarine volcanics: Geochemistry, Geophysics, Geosystems, v. 8, no. 9.

Fretzdorff, S., Schwarz-Schampera, U., Gibson, H., Garbe-Schönberg, C. D., Hauff, F., and Stoffers, P., 2006, Hydrothermal activity and magma genesis along a propagating back-arc basin: Valu Fa Ridge (southern Lau Basin): Journal of Geophysical Research: Solid Earth, v. 111, no. B8.

Freund, S., Beier, C., Krumm, S., and Haase, K. M., 2013, Oxygen isotope evidence for the formation of andesitic–dacitic magmas from the fast-spreading Pacific–Antarctic Rise by assimilation–fractional crystallisation: Chemical Geology, v. 347, p. 271-283.

Gale, A., Dalton, C. A., Langmuir, C. H., Su, Y., and Schilling, J. G., 2013, The mean composition of ocean ridge basalts: Geochemistry, Geophysics, Geosystems, v. 14, no. 3, p. 489-518.

Gill, J. B., 1976, Composition and age of Lau Basin and Ridge volcanic rocks: implications for evolution of an interarc basin and remnant arc: Geological Society of America Bulletin, v. 87, no. 10, p. 1384-1395.

Gill, J. B., and Williams, R. W., 1990, Th isotope and U-series studies of subduction-related volcanic rocks: Geochimica et Cosmochimica Acta, v. 54, no. 5, p. 1427-1442.

Graham, I. J., Reyes, A. G., Wright, I. C., Peckett, K. M., Smith, I. E., and Arculus, R. J., 2008, Structure and petrology of newly discovered volcanic centers in the northern Kermadec–southern Tofua arc, South Pacific Ocean: Journal of Geophysical Research: Solid Earth, v. 113, no. B8.

Haase, K. M., Beier, C., Bach, W., Kleint, C., Anderson, M., Büttner, H., Dede, B., Diehl, A., Ernst, D., Funganitao, C., Giguere, T., Gonzales Porras, M. A., Günther, T., Hüttich, D., Krumm, S. H., Leymann, T., Meierhoff, I., Moje, A., Monien, P., Murdock, S., Nowald, N., Peters, C., Planer- Friedrich, B., Ratmeyer, V., Reuter, C., Reuter, M., Rubin, K., Schade, T., Schleifer, B. K., Schönhofen, M., Sopke, S., Storch, B., Ücker, M., Türke, A., and Wilckens, F., 2018, SO-263 Cruise Report: Tonga Rift.

Haase, K. M., Fretzdorff, S., Mühe, R., Garbe-Schönberg, D., and Stoffers, P., 2009, A geochemical study of off-axis seamount lavas at the Valu Fa Ridge: Constraints on magma genesis and slab contributions in the southern Tonga subduction zone: Lithos, v. 112, no. 1–2, p. 137-148.

Haase, K. M., Freund, S., Beier, C., Koepke, J., Erdmann, M., and Hauff, F., 2016, Constraints on the magmatic evolution of the oceanic crust from plagiogranite intrusions in the Oman ophiolite: Contributions to Mineralogy and Petrology, v. 171, no. 5, p. 46.

Haase, K. M., Worthington, T. J., Stoffers, P., Garbe-Schönberg, D., and Wright, I., 2002, Mantle dynamics, element recycling, and magma genesis beneath the Kermadec Arc-Havre Trough: Geochemistry, Geophysics, Geosystems, v. 3, no. 11, p. 1-22.

Hahm, D., Hilton, D. R., Castillo, P. R., Hawkins, J. W., Hanan, B. B., and Hauri, E. H., 2012, An overview of the volatile systematics of the Lau Basin–Resolving the effects of source variation, magmatic degassing and crustal contamination: Geochimica et Cosmochimica Acta, v. 85, p. 88-113.

Hamburger, M. W., Everingham, I. B., Isacks, B. L., and Barazangi, M., 1988, Active tectonism within the Fiji platform, southwest Pacific: Geology, v. 16, no. 3, p. 237-241.

Hamelin, B., and Allègre, C. J., 1985, Large-scale regional units in the depleted upper mantle revealed by an isotope study of the South-West Indian Ridge: Nature, v. 315, no. 6016, p. 196-199.

Hanyu, T., Dosso, L., Ishizuka, O., Tani, K., Hanan, B. B., Adam, C., Nakai, S. i., Senda, R., Chang, Q., and Tatsumi, Y., 2013, Geochemical diversity in submarine HIMU basalts from Austral Islands, French Polynesia: Contributions to Mineralogy and Petrology, v. 166, no. 5, p. 1285-1304.

Hart, S. R., and Jackson, M. G., 2014, Ta'u and Ofu/Olosega volcanoes: The “Twin Sisters” of Samoa, their P, T, X melting regime, and global implications: Geochemistry, Geophysics, Geosystems, v. 15, no. 6, p. 2301-2318.

Hawkesworth, C., Turner, S., McDermott, F., Peate, D., and Van Calsteren, P., 1997, U-Th isotopes in arc magmas: Implications for element transfer from the subducted crust: Science, v. 276, no. 5312, p. 551-555.

Hawkins, J., and Melchior, J., 1985, Petrology of Mariana Trough and Lau basin basalts: Journal of Geophysical Research: Solid Earth, v. 90, no. B13, p. 11431-11468.

Hawkins Jr, J. W., 1985, Low-K rhyolitic pumice from the Tonga Ridge.

Hawkins, J. W., 1995, The geology of the Lau Basin, Backarc Basins, Springer, p. 63-138.

Hawkins, J. W., Lonsdale, P. F., and Batiza, R., 1987, Petrologic evolution of the Louisville seamount chain: Seamounts, islands, and atolls, v. 43, p. 235-254.

Hayes, G. P., Wald, D. J., and Johnson, R. L., 2012, Slab1. 0: A three-dimensional model of global subduction zone geometries: Journal of Geophysical Research: Solid Earth, v. 117, no. B1.

Hegner, E., and Tatsumoto, M., 1987, Pb, Sr, and Nd isotopes in basalts and sulfides from the Juan de Fuca Ridge: Journal of Geophysical Research: Solid Earth, v. 92, no. B11, p. 11380-11386.

Hergt, J. M., and Woodhead, J. D., 2007, A critical evaluation of recent models for Lau–Tonga arc–backarc basin magmatic evolution: Chemical Geology, v. 245, no. 1-2, p. 9-44.

Hermann, J., Spandler, C., Hack, A., and Korsakov, A. V., 2006, Aqueous fluids and hydrous melts in high-pressure and ultra-high pressure rocks: implications for element transfer in subduction zones: Lithos, v. 92, no. 3-4, p. 399-417.

Hermann, J., and Spandler, C. J., 2008, Sediment Melts at Sub-arc Depths: an Experimental Study: Journal of Petrology, v. 49, no. 4, p. 717-740.

Heuret, A., and Lallemand, S., 2005, Plate motions, slab dynamics and back-arc deformation: Physics of the Earth and Planetary Interiors, v. 149, no. 1-2, p. 31-51.

Heyworth, Z., Turner, S., Schaefer, B., Wood, B., George, R., Berlo, K., Cunningham, H., Price, R., Cook, C., and Gamble, J., 2007, 238U–230Th–226Ra–210Pb constraints on the genesis of high-Mg andesites at White Island, New Zealand: Chemical Geology, v. 243, no. 1-2, p. 105-121.

Hirschmann, M. M., Ghiorso, M. S., and Stolper, E. M., 1999, Calculation of peridotite partial melting from thermodynamic models of minerals and melts; II, Isobaric variations in melts near the solidus and owing to variable source composition: Journal of Petrology, v. 40, no. 2, p. 297-313.

Honda, M., Patterson, D. B., McDougall, I., and Falloon, T. J., 1993, Noble gases in submarine pillow basalt glasses from the Lau Basin: Detection of a solar component in backarc basin basalts: Earth and Planetary Science Letters, v. 120, no. 3-4, p. 135-148.

Horan, M. F., Carlson, R. W., Walker, R. J., Jackson, M., Garçon, M., and Norman, M., 2018, Tracking Hadean processes in modern basalts with 142-Neodymium: Earth and Planetary Science Letters, v. 484, p. 184-191.

Ito, E., White, W. M., and Göpel, C., 1987, The O, Sr, Nd and Pb isotope geochemistry of MORB: Chemical Geology, v. 62, no. 3-4, p. 157-176.

Iwamori, H., 2007, Transportation of H2O beneath the Japan arcs and its implications for global water circulation: Chemical Geology, v. 239, no. 3-4, p. 182-198.

Jackson, M., Hart, S., Konter, J., Kurz, M., Blusztajn, J., and Farley, K., 2014, Helium and lead isotopes reveal the geochemical geometry of the Samoan plume: Nature, v. 514, no. 7522, p. 355-358.

Jackson, M., Kurz, M., Hart, S., and Workman, R., 2005, Implications of new high 3He/4He values from the Samoan hotspot: AGUFM, v. 2005, p. V41D-1485.

Jackson, M. G., and Carlson, R. W., 2012, Homogeneous superchondritic 142Nd/144Nd in the mid-ocean ridge basalt and ocean island basalt mantle: Geochemistry, Geophysics, Geosystems, v. 13, no. 6.

Jackson, M. G., and Hart, S. R., 2006, Strontium isotopes in melt inclusions from Samoan basalts: implications for heterogeneity in the Samoan plume: Earth and Planetary Science Letters, v. 245, no. 1-2, p. 260-277.

Jackson, M. G., Hart, S. R., Konter, J. G., Koppers, A. A., Staudigel, H., Kurz, M. D., Blusztajn, J., and Sinton, J. M., 2010, Samoan hot spot track on a “hot spot highway”: Implications for mantle plumes and a deep Samoan mantle source: Geochemistry, Geophysics, Geosystems, v. 11, no. 12.

Jackson, M. G., Hart, S. R., Koppers, A. A., Staudigel, H., Konter, J., Blusztajn, J., Kurz, M., and Russell, J. A., 2007a, The return of subducted continental crust in Samoan lavas: Nature, v. 448, no. 7154, p. 684-687.

Jackson, M. G., Hart, S. R., Saal, A. E., Shimizu, N., Kurz, M. D., Blusztajn, J. S., and Skovgaard, A. C., 2008, Globally elevated titanium, tantalum, and niobium (TITAN) in ocean island basalts with high 3He/4He: Geochemistry, Geophysics, Geosystems, v. 9, no. 4.

Jackson, M. G., Kurz, M. D., Hart, S. R., and Workman, R. K., 2007b, New Samoan lavas from Ofu Island reveal a hemispherically heterogeneous high 3He/4He mantle: Earth and Planetary Science Letters, v. 264, no. 3-4, p. 360-374.

Jackson, M. G., and Shirey, S. B., 2011, Re–Os isotope systematics in Samoan shield lavas and the use of Os-isotopes in olivine phenocrysts to determine primary magmatic compositions: Earth and Planetary Science Letters, v. 312, no. 1-2, p. 91-101.

Jagoutz, O., Müntener, O., Schmidt, M. W., and Burg, J.-P., 2011, The roles of flux-and decompression melting and their respective fractionation lines for continental crust formation: evidence from the Kohistan arc: Earth and Planetary Science Letters, v. 303, no. 1-2, p. 25-36.

Jenner, F., Arculus, R., Mavrogenes, J., Dyriw, N., Nebel, O., and Hauri, E., 2012, Chalcophile element systematics in volcanic glasses from the northwestern Lau Basin: Geochemistry, Geophysics, Geosystems, v. 13, no. 6.

Jenner, F., and O'Neill, H., 2012, Analysis of 60 elements in 616 ocean floor basaltic glasses: Geochemistry Geophysics Geosystems, v. 13, p. Q02005.

Jenner, G., Cawood, P., Rautenschlein, M., and White, W., 1987, Composition of back-arc basin volcanics, Valu Fa Ridge, Lau Basin: evidence for a slab-derived component in their mantle source: Journal of Volcanology and Geothermal Research, v. 32, no. 1, p. 209-222.

Johnson, M. C., Anderson, A. T., and J, R. M., 1994, Pre-eruptive volatile contents of magmas: Volatiles in magmas, v. 30, no. Reviews in Mineralogy, p. 281-330.

Jones, D. W. R., Katz, R. F., Tian, M., and Rudge, J. F., 2018, Thermal impact of magmatism in subduction zones: Earth and Planetary Science Letters, v. 481, p. 73-79.

Kamenetsky, V. S., Crawford, A. J., Eggins, S., and Mühe, R., 1997, Phenocryst and melt inclusion chemistry of near-axis seamounts, Valu Fa Ridge, Lau Basin: insight into mantle wedge melting and the addition of subduction components: Earth and Planetary Science Letters, v. 151, no. 3-4, p. 205-223.

Keller, N. S., Arculus, R. J., Hermann, J., and Richards, S., 2008, Submarine back-arc lava with arc signature: Fonualei Spreading Center, northeast Lau Basin, Tonga: Journal of Geophysical Research: solid earth, v. 113, no. B8.

Kelley, K. A., and Cottrell, E., 2009, Water and the oxidation state of subduction zone magmas: Science, v. 325, no. 5940, p. 605-607.

Kelley, K. A., Plank, T., Grove, T. L., Stolper, E. M., Newman, S., and Hauri, E., 2006, Mantle melting as a function of water content beneath back-arc basins: Journal of Geophysical Research: Solid Earth, v. 111, no. B9.

Kelley, K. A., Plank, T., Ludden, J., and Staudigel, H., 2005, Subduction cycling of U, Th, and Pb: Earth and Planetary Science Letters, v. 234, p. 369-383.

Kendrick, M. A., Arculus, R. J., Danyushevsky, L. V., Kamenetsky, V. S., Woodhead, J. D., and Honda, M., 2014, Subduction-related halogens (Cl, Br and I) and H2O in magmatic glasses from Southwest Pacific Backarc Basins: Earth and Planetary Science Letters, v. 400, p. 165-176.

Kendrick, M. A., Jackson, M. G., Hauri, E. H., and Phillips, D., 2015, The halogen (F, Cl, Br, I) and H2O systematics of Samoan lavas: Assimilated-seawater, EM2 and high-3He/4He components: Earth and Planetary Science Letters, v. 410, p. 197-209.

Kent, A. J., Peate, D. W., Newman, S., Stolper, E. M., and Pearce, J. A., 2002, Chlorine in submarine glasses from the Lau Basin: seawater contamination and constraints on the composition of slab-derived fluids: Earth and Planetary Science Letters, v. 202, no. 2, p. 361-377.

Kim, J., Son, S.-K., Son, J.-W., Kim, K.-H., Shim, W. J., Kim, C. H., and Lee, K.-Y., 2009, Venting sites along the Fonualei and Northeast Lau Spreading Centers and evidence of hydrothermal activity at an off-axis caldera in the northeastern Lau Basin: Geochemical Journal, v. 43, no. 1, p. 1-13.

Kincaid, C., and Hall, P. S., 2003, Role of back arc spreading in circulation and melting at subduction zones: Journal of Geophysical Research: Solid Earth, v. 108, no. B5.

Klein, E., Langmuir, C., Zindler, A., Staudigel, H., and Hamelin, B., 1988, Isotope evidence of a mantle convection boundary at the Australian-Antarctic Discordance: Nature, v. 333, no. 6174, p. 623-629.

Klein, E. M., Langmuir, C. H., and Staudigel, H., 1991, Geochemistry of basalts from the Southeast Indian Ridge, 115 E–138 E: Journal of Geophysical Research: Solid Earth, v. 96, no. B2, p. 2089-2107.

Kogiso, T., Tatsumi, Y., and Nakano, S., 1997, Trace element transport during dehydration processes in the subducted oceanic crust: 1. Experiments and implications for the origin of ocean island basalts: Earth and Planetary Science Letters, v. 148, no. 1-2, p. 193-205.

Kohut, E. J., Stern, R. J., Kent, A. J., Nielsen, R. L., Bloomer, S. H., and Leybourne, M., 2006, Evidence for adiabatic decompression melting in the Southern Mariana Arc from high-Mg lavas and melt inclusions: Contributions to Mineralogy and Petrology, v. 152, no. 2, p. 201-221.

König, S., Münker, C., Hohl, S., Paulick, H., Barth, A., Lagos, M., Pfänder, J., and Büchl, A., 2011, The Earth's tungsten budget during mantle melting and crust formation: Geochimica et Cosmochimica Acta, v. 75, no. 8, p. 2119-2136.

Konter, J. G., and Jackson, M. G., 2012, Large volumes of rejuvenated volcanism in Samoa: Evidence supporting a tectonic influence on late-stage volcanism: Geochemistry, Geophysics, Geosystems, v. 13, no. 6.

Konter, J. G., Pietruszka, A. J., Hanan, B. B., Finlayson, V. A., Craddock, P. R., Jackson, M. G., and Dauphas, N., 2016, Unusual δ56Fe values in Samoan rejuvenated lavas generated in the mantle: Earth and Planetary Science Letters, v. 450, p. 221-232.

Koppers, A. A., Duncan, R. A., and Steinberger, B., 2004, Implications of a nonlinear 40Ar/39Ar age progression along the Louisville seamount trail for models of fixed and moving hot spots: Geochemistry, Geophysics, Geosystems, v. 5, no. 6.

Koppers, A. A., Staudigel, H., Pringle, M. S., and Wijbrans, J. R., 2003, Short-lived and discontinuous intraplate volcanism in the South Pacific: Hot spots or extensional volcanism?: Geochemistry, Geophysics, Geosystems, v. 4, no. 10.

Langmuir, C., Bezos, A., Escrig, S., and Parman, S., 2006, Chemical systematics and hydrous melting of the mantle in back-arc basins: Geophysical Monograph-American Geophysical Union, v. 166, p. 87.

Langmuir, C. H., Bender, J. F., and Batiza, R., 1986, Petrological and tectonic segmentation of the East Pacific Rise, 5 30′–14 30′ N: Nature, v. 322, no. 6078, p. 422-429.

Layne, G. D., Kent, A. J., and Bach, W., 2009, δ37Cl systematics of a backarc spreading system: The Lau Basin: Geology, v. 37, no. 5, p. 427-430.

Le Bas, M., 2000, IUGS reclassification of the high-Mg and picritic volcanic rocks: Journal of Petrology, v. 41, no. 10, p. 1467-1470.

Leeman, W. P., 1983, The influence of crustal structure on compositions of subduction-related magmas: Journal of Volcanology and Geothermal Research, v. 18, no. 1-4, p. 561-588.

Loock, G., McDonough, W., Goldstein, S., and Hofmann, A., 1990, Isotopic compositions of volcanic glasses from the Lau Basin: Marine Mining, v. 9, no. 2, p. 235-&.

Lundstrom, C. C., 2003a, Uranium-series Disequilibria in Mid-ocean Ridge Basalts: Observations and Models of Basalt Genesis, *in* Bourdon, B., Henderson, G. M., Lundstrom, C., and Turner, S. P., eds., Uranium-series geochemistry, Volume 52: Washington, Mineralogical Society of America, p. 175-214.

Lundstrom, C. C., 2003b, Uranium-series disequilibria in mid-ocean ridge basalts: observations and models of basalt genesis: Reviews in mineralogy and geochemistry, v. 52, no. 1, p. 175-214.

Lupton, J., Rubin, K. H., Arculus, R., Lilley, M., Butterfield, D., Resing, J., Baker, E., and Embley, R., 2015, Helium isotope, C/3 H e, and B a-N b-T i signatures in the northern L au B asin: Distinguishing arc, back-arc, and hotspot affinities: Geochemistry, Geophysics, Geosystems, v. 16, no. 4, p. 1133-1155.

Lyubetskaya, T., and Korenaga, J., 2007, Chemical composition of Earth's primitive mantle and its variance: 1. Method and results: Journal of Geophysical Research: Solid Earth, v. 112, no. B3.

Macdougall, J., and Lugmair, G., 1986, Sr and Nd isotopes in basalts from the East Pacific Rise: significance for mantle heterogeneity: Earth and Planetary Science Letters, v. 77, no. 3-4, p. 273-284.

MacGregor, L., Sinha, M., and Constable, S., 2001, Electrical resistivity structure of the Valu Fa Ridge, Lau Basin, from marine controlled-source electromagnetic sounding: Geophysical Journal International, v. 146, no. 1, p. 217-236.

Mahoney, J., Graham, D., Christie, D., Johnson, K., Hall, L., and Vonderhaar, D., 2002, Between a hotspot and a cold spot: isotopic variation in the Southeast Indian Ridge asthenosphere, 86 E–118 E: Journal of Petrology, v. 43, no. 7, p. 1155-1176.

Mahoney, J., le Roex, A., Peng, Z., Fisher, R., and Natland, J., 1992, Western limits of Indian MORB mantle and the origin of low 206Pb/204Pb MORB: isotope systematics of the central Southwest Indian Ridge (17–50° E): J. Geophys. Res, v. 97, p. 19,771-719,790.

Mahoney, J., Natland, J., White, W., Poreda, R., Bloomer, S., Fisher, R., and Baxter, A., 1989, Isotopic and geochemical provinces of the western Indian Ocean spreading centers: Journal of Geophysical Research: Solid Earth, v. 94, no. B4, p. 4033-4052.

Mahoney, J., Sinton, J., Kurz, M., Macdougall, J., Spencer, K., and Lugmair, G., 1994, Isotope and trace element characteristics of a super-fast spreading ridge: East Pacific Rise, 13–23 S: Earth and Planetary Science Letters, v. 121, no. 1-2, p. 173-193.

Malahoff, A., Feden, R. H., and Fleming, H. S., 1982, Magnetic anomalies and tectonic fabric of marginal basins north of New Zealand: Journal of Geophysical Research: Solid Earth, v. 87, no. B5, p. 4109-4125.

Marschall, H. R., and Schumacher, J. C., 2012, Arc magmas sourced from mélange diapirs in subduction zones: Nature Geoscience, v. 5, no. 11, p. 1-6.

Martinez, F., and Taylor, B., 2006, Modes of crustal accretion in back-arc basins: Inferences from the Lau Basin: Back-Arc Spreading Systems: Geological, Biological, Chemical, and Physical Interactions, v. 166, p. 5-+.

Martinez, F., Taylor, B., Baker, E. T., Resing, J. A., and Walker, S. L., 2006, Opposing trends in crustal thickness and spreading rate along the back-arc Eastern Lau Spreading

Center: Implications for controls on ridge morphology, faulting, and hydrothermal activity: Earth and Planetary Science Letters, v. 245, no. 3-4, p. 655-672.

Massoth, G., Baker, E., Worthington, T., Lupton, J., De Ronde, C., Arculus, R., Walker, S., Nakamura, K. i., Ishibashi, J. i., and Stoffers, P., 2007, Multiple hydrothermal sources along the south Tonga arc and Valu Fa Ridge: Geochemistry, Geophysics, Geosystems, v. 8, no. 11.

McCulloch, M. T., and Gamble, J., 1991, Geochemical and geodynamical constraints on subduction zone magmatism: Earth and Planetary Science Letters, v. 102, no. 3-4, p. 358-374.

McDermott, F., and Hawkesworth, C., 1991, Th, Pb, and Sr isotope variations in young island arc volcanics and oceanic sediments: Earth and Planetary Science Letters, v. 104, no. 1, p. 1-15.

McDougall, I., 2010, Age of volcanism and its migration in the Samoa Islands: Geological Magazine, v. 147, no. 5, p. 705-717.

McGee, L. E., Beier, C., Smith, I. E., and Turner, S. P., 2011, Dynamics of melting beneath a small-scale basaltic system: a U-Th–Ra study from Rangitoto volcano, Auckland volcanic field, New Zealand: Contributions to Mineralogy and Petrology, v. 162, no. 3, p. 547-563.

McKenzie, D., 1985, 230Th238U disequilibrium and the melting processes beneath ridge axes: Earth and Planetary Science Letters, v. 72, no. 2-3, p. 149-157.

Meffre, S., Falloon, T. J., Crawford, T. J., Hoernle, K., Hauff, F., Duncan, R. A., Bloomer, S. H., and Wright, D. J., 2012, Basalts erupted along the Tongan fore arc during subduction initiation: Evidence from geochronology of dredged rocks from the Tonga fore arc and trench: Geochemistry, Geophysics, Geosystems, v. 13, no. 12.

Michard, A., Montigny, R., and Schlich, R., 1986, Geochemistry of the mantle beneath the Rodriguez triple junction and the South-East Indian Ridge: Earth and Planetary Science Letters, v. 78, no. 1, p. 104-114.

Millen, D. W., and Hamburger, M. W., 1998, Seismological evidence for tearing of the Pacific plate at the northern termination of the Tonga subduction zone: Geology, v. 26, no. 7, p. 659-662.

Mortimer, N., Gans, P., Palin, J., Meffre, S., Herzer, R., and Skinner, D., 2010, Location and migration of Miocene–Quaternary volcanic arcs in the SW Pacific region: Journal of Volcanology and Geothermal Research, v. 190, no. 1-2, p. 1-10.

Morton, J. L., and Pohl, W., 1990, Magnetic anomaly identification in the Lau basin and North Fiji basin, southwest Pacific ocean: Geologisches Jahrbuch. Reihe D. Mineralogie, Petrographie, Geochemie, Lagerstättenkunde, no. 92, p. 93-108.

Morton, J. L., and Sleep, N. H., 1985, Seismic reflections from a Lau Basin magma chamber.

Nakakuki, T., and Mura, E., 2013, Dynamics of slab rollback and induced back-arc basin formation: Earth and Planetary Science Letters, v. 361, p. 287-297.

Nebel, O., and Arculus, R. J., 2015, Selective ingress of a Samoan plume component into the northern Lau backarc basin: Nature communications, v. 6, no. 1, p. 1-7.

Nebel, O., Sossi, P. A., Foden, J., Bénard, A., Brandl, P. A., Stammeier, J. A., Lupton, J., Richter, M., and Arculus, R. J., 2018, Iron isotope variability in ocean floor lavas and mantle sources in the Lau back-arc basin: Geochimica et Cosmochimica Acta, v. 241, p. 150-163.

Newsom, H., White, W., Jochum, K., and Hofmann, A., 1986, Siderophile and chalcophile element abundances in oceanic basalts, Pb isotope evolution and growth of the Earth's core: Earth and Planetary Science Letters, v. 80, no. 3-4, p. 299-313.

Niu, Y., and Batiza, R., 1991, An empirical method for calculating melt compositions produced beneath mid-ocean ridges; for axis and off-axis (seamounts) melting application: Journal of Geophysical Research, B, Solid Earth and Planets, v. 96, no. 13, p. 21,753-721,777.

O'Neill, H. S. C., 2016, The smoothness and shapes of chondrite-normalized rare earth element patterns in basalts: Journal of Petrology, v. 57, no. 8, p. 1463-1508.

Park, J.-W., Campbell, I. H., Kim, J., and Moon, J.-W., 2015, The role of late sulfide saturation in the formation of a Cu-and Au-rich magma: Insights from the platinum group element geochemistry of Niuatahi–Motutahi lavas, Tonga rear arc: Journal of Petrology, v. 56, no. 1, p. 59-81.

Paropkari, A. L., Ray, D., Balaram, V., Prakash, L. S., Mirza, I. H., Satyanarayana, M., Rao, T. G., and Kaisary, S., 2010, Formation of hydrothermal deposits at Kings Triple Junction, northern Lau back-arc basin, SW Pacific: The geochemical perspectives: Journal of Asian Earth Sciences, v. 38, no. 3-4, p. 121-130.

Parson, L., and Wright, I., 1996, The Lau-Havre-Taupo back-arc basin: A southward-propagating, multi-stage evolution from rifting to spreading: Tectonophysics, v. 263, no. 1-4, p. 1-22.

Peacock, S. M., 1990, Numerical simulation of metamorphic pressure-temperature-time paths and fluid production in subducting slabs: Tectonics, v. 9, no. 5, p. 1197-1211.

Peacock, S. M., 2003, Thermal structure and metamorphic evolution of subducting slabs: Geophysical Monograph-American Geophysical Union, v. 138, p. 7-22.

Pearce, J. A., 1983, Role of the sub-continental lithosphere in magma genesis at active continental margins.

Pearce, J. A., Ernewein, M., Bloomer, S. H., Parson, L. M., Murton, B. J., and Johnson, L. E., 1994, Geochemistry of Lau Basin volcanic rocks: influence of ridge segmentation and arc proximity: Geological Society, London, Special Publications, v. 81, no. 1, p. 53-75.

Pearce, J. A., Kempton, P., and Gill, J., 2007, Hf–Nd evidence for the origin and distribution of mantle domains in the SW Pacific: Earth and Planetary Science Letters, v. 260, no. 1, p. 98-114.

Pearce, J. A., and Peate, D. W., 1995, Tectonic implications of the composition of volcanic arc magmas: Annual Review of Earth and Planetary Sciences, v. 23, p. 251-286.

Pearce, J. A., and Reagan, M. K., 2019, Identification, classification, and interpretation of boninites from Anthropocene to Eoarchean using Si-Mg-Ti systematics: Geosphere, v. 15, no. 4, p. 1008-1037.

Pearce, J. A., and Stern, R. J., 2006a, Origin of back-arc basin magmas: trace element and isotope perspectives: Geophysical Monograph-American Geophysical Union, v. 166, p. 63.

Pearce, J. A., and Stern, R. J., 2006b, The origin of back-arc basin magmas: trace element and isotope perspectives., *in* Christie, D. M., ed., Back-Arc Spreading Systems: Geological, Biological, Chemical, and Physical Interactions, Volume 166: Washington D.C., p. 63-86.

Pearce, J. A., Stern, R. J., Bloomer, S. H., and Fryer, P., 2005, Geochemical mapping of the Mariana arc-basin system: Implications for the nature and distribution of subduction components: Geochemistry, geophysics, geosystems, v. 6, no. 7.

Peate, D. W., and Hawkesworth, C. J., 2005, U series disequilibria; insights into mantle melting and the timescales of magma differentiation: Reviews of Geophysics, v. 43, no. 1, p. RG1003.1001-1043.

Peate, D. W., Kokfelt, T. F., Hawkesworth, C. J., Van Calsteren, P. W., Hergt, J. M., and Pearce, J. A., 2001, U-series isotope data on Lau Basin glasses: the role of subduction-related fluids during melt generation in back-arc basins: Journal of Petrology, v. 42, no. 8, p. 1449-1470.

Plank, T., and Langmuir, C. H., 1988, An evaluation of the global variations in the major element chemistry of arc basalts: Earth and Planetary Science Letters, v. 90, no. 4, p. 349-370.

Price, A. A., Jackson, M. G., Blichert-Toft, J., Blusztajn, J., Conatser, C. S., Konter, J. G., Koppers, A. A., and Kurz, M. D., 2016, Geochemical evidence in the northeast Lau

Basin for subduction of the Cook-Austral volcanic chain in the Tonga Trench: Geochemistry, Geophysics, Geosystems, v. 17, no. 5, p. 1694-1724.

Price, A. A., Jackson, M. G., Blichert-Toft, J., Hall, P. S., Sinton, J. M., Kurz, M. D., and Blusztajn, J., 2014, Evidence for a broadly distributed Samoan-plume signature in the northern Lau and North Fiji Basins: Geochemistry, Geophysics, Geosystems, v. 15, no. 4, p. 986-1008.

Price, A. A., Jackson, M. G., Blichert-Toft, J., Kurz, M. D., Gill, J., Blusztajn, J., Jenner, F., Brens, R., and Arculus, R., 2017, Geodynamic implications for zonal and meridional isotopic patterns across the northern L au and N orth F iji B asins: Geochemistry, Geophysics, Geosystems, v. 18, no. 3, p. 1013-1042.

Price, R., Kennedy, A., Riggs-Sneeringer, M., and Frey, F., 1986, Geochemistry of basalts from the Indian Ocean triple junction: implications for the generation and evolution of Indian Ocean ridge basalts: Earth and Planetary Science Letters, v. 78, no. 4, p. 379-396.

Profeta, L., Ducea, M. N., Chapman, J. B., Paterson, S. R., Gonzales, S. M. H., Kirsch, M., Petrescu, L., and DeCelles, P. G., 2015, Quantifying crustal thickness over time in magmatic arcs: Scientific reports, v. 5, p. 17786.

Pyle, D. G., Christie, D. M., and Mahoney, J. J., 1992, Resolving an isotopic boundary within the Australian-Antarctic Discordance: Earth and Planetary Science Letters, v. 112, no. 1-4, p. 161-178.

Regelous, M., Collerson, K., Ewart, A., and Wendt, J., 1997, Trace element transport rates in subduction zones: evidence from Th, Sr and Pb isotope data for Tonga-Kermadec arc lavas: Earth and Planetary Science Letters, v. 150, no. 3, p. 291-302.

Rehkaemper, M., and Hofmann, A., 1997, Recycled ocean crust and sediment in Indian Ocean MORB: Earth and Planetary Science Letters, v. 147, no. 1-4, p. 93-106.

Reinhard, A. A., Jackson, M. G., Blusztajn, J., Koppers, A. A., Simms, A. R., and Konter, J. G., 2019, “Petit Spot” Rejuvenated Volcanism Superimposed on Plume-Derived Samoan Shield Volcanoes: Evidence From a 645-m Drill Core From Tutuila Island, American Samoa: Geochemistry, Geophysics, Geosystems, v. 20, no. 3, p. 1485-1507.

Resing, J. A., Rubin, K. H., Embley, R. W., Lupton, J. E., Baker, E. T., Dziak, R. P., Baumberger, T., Lilley, M. D., Huber, J. A., and Shank, T. M., 2011, Active submarine eruption of boninite in the northeastern Lau Basin: Nature Geoscience, v. 4, no. 11, p. 799-806.

Robinson, J. A. C., and Wood, B. J., 1998, The depth of the spinel to garnet transition at the peridotite solidus: Earth and Planetary Science Letters, v. 164, no. 1-2, p. 277-284.

Romer, R., Beier, C., Haase, K., Klügel, A., and Hamelin, C., 2019, Progressive changes in magma transport at the active Serreta Ridge, Azores: Geochemistry, Geophysics, Geosystems.

Romer, R. H., Beier, C., Haase, K. M., and Hübscher, C., 2018, Correlated changes between volcanic structures and magma composition in the Faial volcanic system, Azores: Frontiers in Earth Science, v. 6, p. 78.

Ruellan, E., Delteil, J., Wright, I., and Matsumoto, T., 2003, From rifting to active spreading in the Lau Basin–Havre Trough backarc system (SW Pacific): Locking/unlocking induced by seamount chain subduction: Geochemistry, Geophysics, Geosystems, v. 4, no. 5.

Rüpke, L. H., Morgan, J. P., Hort, M., and Connolly, J. A., 2004, Serpentine and the subduction zone water cycle: Earth and Planetary Science Letters, v. 223, no. 1-2, p. 17-34.

Salters, V. J., Mallick, S., Hart, S. R., Langmuir, C. E., and Stracke, A., 2011, Domains of depleted mantle: New evidence from hafnium and neodymium isotopes: Geochemistry, Geophysics, Geosystems, v. 12, no. 8.

Salters, V. J., and White, W. M., 1998, Hf isotope constraints on mantle evolution: Chemical Geology, v. 145, no. 3-4, p. 447-460.

Scott, S. R., Sims, K. W., Reagan, M. K., Ball, L., Schwieters, J. B., Bouman, C., Lloyd, N. S., Waters, C. L., Standish, J. J., and Tollstrup, D. L., 2019, The application of abundance sensitivity filters to the precise and accurate measurement of uranium series nuclides by plasma mass spectrometry: International Journal of Mass Spectrometry, v. 435, p. 321-332.

Sdrolias, M., and Müller, R. D., 2006, Controls on back-arc basin formation: Geochemistry, Geophysics, Geosystems, v. 7, no. 4.

Sims, K. W., Gill, J. B., Dosseto, A., Hoffmann, D. L., Lundstrom, C. C., Williams, R. W., Ball, L., Tollstrup, D., Turner, S., and Prytulak, J., 2008a, An inter-laboratory assessment of the thorium isotopic composition of synthetic and rock reference materials: Geostandards and Geoanalytical Research, v. 32, no. 1, p. 65-91.

Sims, K. W., Hart, S., Reagan, M., Blusztajn, J., Staudigel, H., Sohn, R., Layne, G., Ball, L., and Andrews, J., 2008b, 238U-230Th-226Ra-210Pb-210Po, 232Th-228Ra, and 235U-231Pa constraints on the ages and petrogenesis of Vailulu'u and Malumalu Lavas, Samoa: Geochemistry, Geophysics, Geosystems, v. 9, no. 4.

Sims, K. W., Pichat, S., Reagan, M. K., Kyle, P. R., Dulaiova, H., Dunbar, N. W., Prytulak, J., Sawyer, G., Layne, G. D., and Blichert-Toft, J., 2013, On the time scales of magma genesis, melt evolution, crystal growth rates and magma degassing in the Erebus volcano magmatic system using the 238U, 235U and 232Th decay series: Journal of Petrology, v. 54, no. 2, p. 235-271.

Sinton, J. M., Ford, L. L., Chappell, B., and McCULLOCH, M. T., 2003, Magma genesis and mantle heterogeneity in the Manus back-arc basin, Papua New Guinea: Journal of Petrology, v. 44, no. 1, p. 159-195.

Sleeper, J. D., and Martinez, F., 2014, Controls on segmentation and morphology along the back-arc Eastern Lau Spreading Center and Valu Fa Ridge: Journal of Geophysical Research: Solid Earth, v. 119, no. 3, p. 1678-1700.

Sleeper, J. D., Martinez, F., and Arculus, R., 2016, The Fonualei Rift and Spreading Center: Effects of ultraslow spreading and arc proximity on back-arc crustal accretion: Journal of Geophysical Research: Solid Earth, v. 121, no. 7, p. 4814-4835.

Smith, I. E., and Price, R. C., 2006, The Tonga–Kermadec arc and Havre–Lau back-arc system: their role in the development of tectonic and magmatic models for the western Pacific: Journal of volcanology and geothermal research, v. 156, no. 3-4, p. 315-331.

Spandler, C., Mavrogenes, J., and Hermann, J., 2007, Experimental constraints on element mobility from subducted sediments using high-P synthetic fluid/melt inclusions: Chemical Geology, v. 239, no. 3-4, p. 228-249.

Standish, J. J., and Sims, K. W. W., 2010, Young off-axis volcanism along the ultraslow-spreading Southwest Indian Ridge: Nature Geosci, v. 3, no. 4, p. 286-292.

Stern, R. J., 2002, Subduction zones: Reviews of geophysics, v. 40, no. 4.

Stolz, A., Jochum, K., Spettel, B., and Hofmann, A., 1996, Fluid-and melt-related enrichment in the subarc mantle: evidence from Nb/Ta variations in island-arc basalts: Geology, v. 24, no. 7, p. 587-590.

Sutherland, R., Dickens, G. R., Blum, P., Agnini, C., Alegret, L., Asatryan, G., Bhattacharya, J., Bordenave, A., Chang, L., and Collot, J., 2020, Continental-scale geographic change across Zealandia during Paleogene subduction initiation: Geology, v. 48, no. 5, p. 419-424.

Tappin, D., Bruns, T., and Geist, E., 1994, 22. RIFTING OF THE TONGA/LAU RIDGE AND FORMATION OF THE LAU BACKARC BASIN: EVIDENCE FROM SITE 840 ON THE TONGA RIDGE1.

Tatsumi, Y., and Eggins, S., 1995, Subduction zone magmatism, Wiley.

Tatsumi, Y., Hamilton, D., and Nesbitt, R., 1986, Chemical characteristics of fluid phase released from a subducted lithosphere and origin of arc magmas: evidence from high-

pressure experiments and natural rocks: Journal of Volcanology and Geothermal Research, v. 29, no. 1-4, p. 293-309.

Tatsumi, Y., and Kogiso, T., 2003, The subduction factory: its role in the evolution of the Earth's crust and mantle: Geological Society, London, Special Publications, v. 219, no. 1, p. 55-80.

Tatsumi, Y., Sakuyama, M., Fukuyama, H., and Kushiro, I., 1983, Generation of arc basalt magmas and thermal structure of the mantle wedge in subduction zones: Journal of Geophysical Research: Solid Earth, v. 88, no. B7, p. 5815-5825.

Taylor, B., and Martinez, F., 2003, Back-arc basin basalt systematics: Earth and Planetary Science Letters, v. 210, no. 3-4, p. 481-497.

Taylor, B., Zellmer, K., Martinez, F., and Goodliffe, A., 1996, Sea-floor spreading in the Lau back-arc basin: Earth and Planetary Science Letters, v. 144, no. 1, p. 35-40.

Tian, L., Castillo, P. R., Hawkins, J. W., Hilton, D. R., Hanan, B. B., and Pietruszka, A. J., 2008, Major and trace element and Sr–Nd isotope signatures of lavas from the Central Lau Basin: Implications for the nature and influence of subduction components in the back-arc mantle: Journal of Volcanology and Geothermal Research, v. 178, no. 4, p. 657-670.

Tian, L., Castillo, P. R., Hilton, D. R., Hawkins, J. W., Hanan, B. B., and Pietruszka, A. J., 2011, Major and trace element and Sr-Nd isotope signatures of the northern Lau Basin lavas: Implications for the composition and dynamics of the back-arc basin mantle: Journal of Geophysical Research: Solid Earth, v. 116, no. B11.

Timm, C., Bassett, D., Graham, I. J., Leybourne, M. I., De Ronde, C. E., Woodhead, J., Layton-Matthews, D., and Watts, A. B., 2013, Louisville seamount subduction and its implication on mantle flow beneath the central Tonga–Kermadec arc: Nature communications, v. 4, no. 1, p. 1-9.

Timm, C., de Ronde, C., Hoernle, K., Cousens, B., Wartho, J.-A., Tontini, F. C., Wysoczanski, R., Hauff, F., and Handler, M., 2019, New age and geochemical data from the southern Colville and Kermadec ridges, SW Pacific: insights into the recent geological history and petrogenesis of the Proto-Kermadec (Vitiaz) Arc: Gondwana Research, v. 72, p. 169-193.

Timm, C., Graham, I. J., de Ronde, C. E., Leybourne, M. I., and Woodhead, J., 2011, Geochemical evolution of Monowai volcanic center: New insights into the northern Kermadec arc subduction system, SW Pacific: Geochemistry, Geophysics, Geosystems, v. 12, no. 8.

Tollstrup, D., Gill, J., Kent, A., Prinkey, D., Williams, R., Tamura, Y., and Ishizuka, O., 2010, Across-arc geochemical trends in the Izu-Bonin arc: Contributions from the subducting slab, revisited: Geochemistry Geophysics Geosystems, v. 11, no. 1, p. Q01X10-.

Tontini, F. C., Bassett, D., de Ronde, C. E., Timm, C., and Wysoczanski, R., 2019, Early evolution of a young back-arc basin in the Havre Trough: Nature Geoscience, v. 12, no. 10, p. 856-862.

Turner, M., Ireland, T., Hermann, J., Holden, P., Padrón-Navarta, J. A., Hauri, E. H., and Turner, S., 2015, Sensitive high resolution ion microprobe–stable isotope (SHRIMP-SI) analysis of water in silicate glasses and nominally anhydrous reference minerals: Journal of Analytical Atomic Spectrometry, v. 30, no. 8, p. 1706-1722.

Turner, S., Beier, C., Niu, Y., and Cook, C., 2011, U-Th-Ra disequilibria and the extent of off-axis volcanism across the East Pacific Rise at 9°30'N, 10°30'N, and 11°20'N: Geochemistry, Geophysics, Geosystems, v. 12, no. 7, p. Q0AC12.

Turner, S., Bourdon, B., and Gill, J., 2003a, Insights into magma genesis at convergent margins from U-series isotopes: Reviews in Mineralogy and Geochemistry, v. 52, no. 1, p. 255-315.

Turner, S., Bourdon, B., and Gill, J. B., 2003b, Insights into magma genesis at convergent margins from U-series isotopes., *in* Bourdon, B., Henderson, G. M., Lundstrom, C., and

Turner, S. P., eds., Uranium-series geochemistry, Volume 52: Washington, Mineralogical Society of America, p. 255-310.

Turner, S., Bourdon, B., Hawkesworth, C., and Evans, P., 2000, 226 Ra–230 Th evidence for multiple dehydration events, rapid melt ascent and the time scales of differentiation beneath the Tonga–Kermadec island arc: Earth and Planetary Science Letters, v. 179, no. 3, p. 581-593.

Turner, S., Caulfield, J., Rushmer, T., Turner, M., Cronin, S., Smith, I., and Handley, H., 2012, Magma evolution in the primitive, intra-oceanic Tonga arc: Rapid petrogenesis of dacites at Fonualei volcano: Journal of petrology, v. 53, no. 6, p. 1231-1253.

Turner, S., Evans, P., and Hawkesworth, C. J., 2001, Ultrafast source-to-surface movement of melt at island arcs from ^{226}Ra-^{230}Th systematics: Science, v. 292, no. 5520, p. 1363-1366.

Turner, S., and Foden, J., 2001, U, Th and Ra disequilibria, Sr, Nd and Pb isotope and trace element variations in Sunda arc lavas: predominance of a subducted sediment component: Contributions to Mineralogy and Petrology, v. 142, no. 1, p. 43-57.

Turner, S., and Hawkesworth, C., 1997, Constraints on flux rates and mantle dynamics beneath island arcs from Tonga–Kermadec lava geochemistry: Nature, v. 389, no. 6651, p. 568-573.

Turner, S., and Hawkesworth, C., 1998, Using geochemistry to map mantle flow beneath the Lau Basin: Geology, v. 26, no. 11, p. 1019-1022.

Turner, S., Hawkesworth, C., Rogers, N., Bartlett, J., Worthington, T., Hergt, J., Pearce, J., and Smith, I., 1997, 238 U 230 Th disequilibria, magma petrogenesis, and flux rates beneath the depleted Tonga-Kermadec island arc: Geochimica et Cosmochimica Acta, v. 61, no. 22, p. 4855-4884.

Turner, S. J., Langmuir, C. H., Katz, R. F., Dungan, M. A., and Escrig, S., 2016, Parental arc magma compositions dominantly controlled by mantle-wedge thermal structure: Nature Geoscience, v. 9, no. 10, p. 772-776.

Vallier, T., Jenner, G., Frey, F., Gill, J., Davis, A., Volpe, A., Hawkins, J., Morris, J., Cawood, P. A., and Morton, J., 1991, Subalkaline andesite from Valu Fa Ridge, a back-arc spreading center in southern Lau Basin: petrogenesis, comparative chemistry, and tectonic implications: Chemical Geology, v. 91, no. 3, p. 227-256.

Vallier, T. L., 1985, Petrology of rocks dredged from the landward slope of the Tonga Trench: implications for middle Miocene volcanism and subsidence of the Tonga Ridge.

van der Hilst, R., 1995, Complex morphology of subducted lithosphere in the mantle beneath the Tonga trench: Nature, v. 374, no. 6518, p. 154-157.

van Keken, P. E., Hacker, B. R., Syracuse, E. M., and Abers, G. A., 2011, Subduction factory: 4. Depth-dependent flux of H2O from subducting slabs worldwide: Journal of Geophysical Research: Solid Earth, v. 116, no. B1.

Vlastelic, I., Aslanian, D., Dosso, L., Bougault, H., Olivet, J., and Geli, L., 1999, Large-scale chemical and thermal division of the Pacific mantle: Nature, v. 399, no. 6734, p. 345-350.

Von Stackelberg, U., Marchig, V., Müller, P., and Weiser, T., 1990, Hydrothermal mineralization in the Lau and North Fiji basins: Geol. Jahrb., Reihe D, v. 92, p. 547-613.

Wallace, P. J., 2005, Volatiles in subduction zone magmas: concentrations and fluxes based on melt inclusion and volcanic gas data: Journal of volcanology and Geothermal Research, v. 140, no. 1-3, p. 217-240.

Wei, S. S., Wiens, D. A., Zha, Y., Plank, T., Webb, S. C., Blackman, D. K., Dunn, R. A., and Conder, J. A., 2015, Seismic evidence of effects of water on melt transport in the Lau back-arc mantle: Nature, v. 518, no. 7539, p. 395-398.

Wendt, J., Regelous, M., Collerson, K. t., and Ewart, A., 1997, Evidence for a contribution from two mantle plumes to island-arc lavas from northern Tonga: Geology, v. 25, no. 7, p. 611-614.

Wendt, J. I., Regelous, M., Niu, Y., Hékinian, R., and Collerson, K. D., 1999, Geochemistry of lavas from the Garrett Transform Fault: insights into mantle heterogeneity beneath the eastern Pacific: Earth and Planetary Science Letters, v. 173, no. 3, p. 271-284.

Whelan, P. M., Gill, J. B., Kollman, E., Duncan, R. A., and Drake, R. E., 1985, Radiometric dating of magmatic stages in Fiji.

White, W. M., Hofmann, A., and Puchelt, H., 1987, Isotope geochemistry of Pacific mid-ocean ridge basalt: Journal of Geophysical Research: Solid Earth, v. 92, no. B6, p. 4881-4893.

Wiedicke, M., and Collier, J., 1993, Morphology of the Valu Fa Spreading Ridge in the southern Lau Basin: Journal of Geophysical Research: Solid Earth, v. 98, no. B7, p. 11769-11782.

Wiens, D. A., Kelley, K. A., and Plank, T., 2006, Mantle temperature variations beneath back-arc spreading centers inferred from seismology, petrology, and bathymetry: Earth and Planetary Science Letters, v. 248, no. 1-2, p. 30-42.

Wiens, D. A., Koper, K., Xu, Y., Roth, E., Dorman, L. M., Webb, S., Hildebrand, J. A., and Zhao, D., 1998, The upper mantle seismic structure of the Lau spreading center, *in* Anonymous, ed., AGU 1998 spring meeting., Volume 79: Washington, DC, United States, American Geophysical Union, p. 225.

Woelki, D., Regelous, M., Haase, K. M., and Beier, C., 2019, Geochemical mapping of a paleo-subduction zone beneath the Troodos Ophiolite: Chemical Geology, v. 523, p. 1-8.

Wood, B. J., Bryndzia, L. T., and Johnson, K. E., 1990, Mantle oxidation state and its relationship to tectonic environment and fluid speciation: Science, v. 248, no. 4953, p. 337-345.

Woodhall, D., 1985, Geology of the Lau Ridge.

Woodhead, J., Eggins, S., and Gamble, J., 1993, High field strength and transition element systematics in island arc and back-arc basin basalts: evidence for multi-phase melt extraction and a depleted mantle wedge: Earth and Planetary Science Letters, v. 114, no. 4, p. 491-504.

Workman, R. K., and Hart, S. R., 2005, Major and trace element composition of the depleted MORB mantle (DMM): Earth and Planetary Science Letters, v. 231, no. 1, p. 53-72.

Workman, R. K., Hart, S. R., Jackson, M., Regelous, M., Farley, K., Blusztajn, J., Kurz, M., and Staudigel, H., 2004, Recycled metasomatized lithosphere as the origin of the Enriched Mantle II (EM2) end-member: Evidence from the Samoan Volcanic Chain: Geochemistry, Geophysics, Geosystems, v. 5, no. 4.

Workman, R. K., Hauri, E., Hart, S. R., Wang, J., and Blusztajn, J., 2006, Volatile and trace elements in basaltic glasses from Samoa: Implications for water distribution in the mantle: Earth and Planetary Science Letters, v. 241, no. 3-4, p. 932-951.

Yan, C., A plate reconstruction of the south west Pacific 0-100 Ma, *in* Proceedings Proceedings of Ocean Drilling Program, Scientific Results1993, Volume 130, p. 697-709.

Zellmer, K. E., and Taylor, B., 2001, A three-plate kinematic model for Lau Basin opening: Geochemistry, Geophysics, Geosystems, v. 2, no. 5.

Zha, Y., Webb, S. C., Wei, S. S., Wiens, D. A., Blackman, D. K., Menke, W., Dunn, R. A., and Conder, J. A., 2014, Seismological imaging of ridge–arc interaction beneath the Eastern Lau Spreading Center from OBS ambient noise tomography: Earth and Planetary Science Letters, v. 408, no. 0, p. 194-206.

Zhang, H., Yan, Q., Li, C., Zhu, Z., Zhao, R., and Shi, X., 2019, Geochemistry of diverse lava types from the Lau Basin (South West Pacific): Implications for complex back-arc mantle dynamics: Geological Journal, v. 54, no. 6, p. 3643-3659.

Zhao, D., Xu, Y., Wiens, D. A., Dorman, L., Hildebrand, J., and Webb, S., 1997, Depth extent of the Lau back-arc spreading center and its relation to subduction processes: Science, v. 278, no. 5336, p. 254-257.

Zindler, A., Staudigel, H., and Batiza, R., 1984, Isotope and trace element geochemistry of young Pacific seamounts: implications for the scale of upper mantle heterogeneity: Earth and Planetary Science Letters, v. 70, no. 2, p. 175-195.

APPENDIX

1 TABLES

Table A1: Major element, water contents, trace element and Sr-Nd-Pb isotope analyses of the NELSC, DR, southernmost seamounts and MTJ.

Table A2: Water and trace element analyses of the VFR transect.

Table A3: Uranium-series of the VFR transect (including standard analyses).

Table A4: Major and trace element EMP and XRF standard analyses.

Table A5: Trace element LA-ICP-MS standard analyses.

Table A6: Water SHRIMP-SI standard analyses.

2 Figures

Figure A7: Mounted glass samples for SHRIMP-SI analyses at Australia National University (ANU), Canberra, Australia, Disc 1 – 6.

2 ABBREVIATIONS

- **n** number of samples
- **LOI** loss on ignition
- **SD** standard deviation
- **err. Abs.** absolute error
- **NELSC** North-East Lau Spreading Centre
- **DR** Diagonal Ridge
- **MTJ** Mangatolu Triple Junction
- **Smt** southernmost seamounts
- **VFR** Valu-Fa Ridge
- **GZN** GeoZentrum Nordbayern, Erlangen
- **MQU** Macquarie University Sydney
- **ANU** Australia National University, Canberrra
- **EMP** Electron microprobe
- **XRF** X-ray fluorescence analysis
- **LA-ICP-MS** Laserablation inductively-coupled-plasma mass-spectrometry
- **MC-ICP-MS** Multicollector inductively-coupled-plasma mass-spectrometry
- **Q-ICP-MS** Quadrupole inductively-coupled-plasma mass-spectrometry
- **SHRIMP-SI** Sensitive high resolution ion microprobe – stable isotope

Table A1 *Major and trace elements, and Sr-Nd-Pb isotope ratios of lavas from cruise SO263 from the NELSC, DR and smt. Segment number I-IV in brackets. D120 and MTJ samples from previous cruises (Melville96 and Keldysh90). Analytical methods in italics. Major element totals are given without H_2O contents. $FeO^T = Fe_2O_3 + 0.8998 \times FeO$*

Sample	074VSR-01	075VSR-02	076VSR-01	077VSR-01	078VSR-01	079VSR-02	080VSR-01
Location	NELSC (II)	NELSC (II)	NELSC (II)	NELSC (III)	NELSC (III)	NELSC (III)	NELSC (III)
Latitude (S)	15.35	15.36	15.37	15.37	15.38	15.39	15.40
Longitude (W)	174.23	174.23	174.24	174.23	174.24	174.25	174.27
Elevation (m)	-1801	-1700	-1670	-1681	-1636	-1615	-1826
(wt. %)	*EMP*	*EMP/* ***SHRIMP-SI***	*EMP/* ***SHRIMP-SI***	*EMP*	*EMP*	*EMP/* ***SHRIMP-SI***	*EMP*
SiO_2	48.52	48.64	50.29	52.44	49.40	48.74	54.29
TiO_2	1.27	1.13	0.97	0.86	1.10	1.11	1.54
Al_2O_3	16.34	15.68	16.11	16.08	15.16	15.36	14.61
FeO^T	9.38	9.21	8.39	8.88	8.95	9.08	11.19
MnO	0.16	0.16	0.16	0.17	0.18	0.18	0.20
MgO	5.68	6.86	6.98	5.85	6.61	7.05	3.90
CaO	11.60	12.58	12.53	11.37	12.37	12.70	8.45
Na_2O	3.47	3.64	2.75	2.06	2.84	2.93	3.31
K_2O	1.16	0.88	0.65	0.88	1.11	0.88	0.98
P_2O_5	0.52	0.49	0.30	0.19	0.44	0.41	0.27
SO_3	0.05	0.06	0.06	0.02	0.04	0.04	0.05
Cl	0.21	0.21	0.16	0.17	0.19	0.17	0.28
H_2O	-	**1.37**	**1.31**	-	-	**1.37**	-
SD (2σ)	-	**0.06**	**0.05**	-	-	**0.32**	-
LOI	-	-	-	-	-	-	-
Total	98.32	99.49	99.32	98.92	98.33	98.61	99.02
(ppm)	*LA-ICP-MS*	*LA-ICP-MS*	*LA-ICP-MS*	*LA-ICP-MS*	*LA-ICP-MS*	*LA-ICP-MS*	*LA-ICP-MS*
Sc	18.61	20.44	22.77	23.97	25.1	25.94	24.59
V	269	256	225	246	270	263	356
Cr	3.01	27.15	42.8	12.3	60.9	31.7	2.87
Co	40.3	40.4	37.6	37.8	39.6	43.6	31.3
Ni	34.8	55.7	51.3	30.6	49.1	64.4	8.22
Cu	112	99	88	109	104	96.4	162
Zn	97.2	85.3	77.0	85.0	86.5	86.4	113
Rb	32.4	22.4	17.4	22.2	31.2	23.6	26.6
Sr	836	792	459	254	660	625	206
Y	18.55	15.62	14.93	12.61	16.61	15.63	24.2
Zr	102	88.5	59.9	52.0	85.0	79.4	80.6
Nb	44.8	45.6	20.6	8.9	31.9	31.7	8.66
Cs	0.630	0.451	0.321	0.356	0.674	0.452	0.443
Ba	451	370	233	174	390	330	173
La	41.8	41.0	22.6	8.29	31.7	31.0	9.45
Ce	83.5	86.5	46.4	18.0	64.6	64.0	22.9
Pr	9.10	9.04	5.26	2.26	7.06	7.04	2.96
Nd	34.6	34.8	19.8	10.1	28.1	27.1	13.1
Sm	6.39	5.78	3.97	2.11	5.20	4.88	3.46
Eu	1.85	1.77	1.26	0.80	1.70	1.50	1.21
Gd	4.88	4.52	3.33	2.33	4.16	3.97	3.86
Tb	0.650	0.560	0.510	0.340	0.610	0.560	0.610
Dy	3.99	3.55	2.88	2.34	3.62	3.35	4.40
Ho	0.692	0.686	0.587	0.499	0.652	0.636	0.990
Er	1.96	1.81	1.63	1.32	1.96	1.62	2.83
Tm	0.274	0.240	0.223	0.207	0.257	0.240	0.445
Yb	1.95	1.54	1.71	1.48	1.76	1.64	3.11
Lu	0.280	0.230	0.230	0.210	0.230	0.210	0.420
Hf	2.26	2.05	1.54	1.54	1.96	1.94	2.18
Ta	2.38	2.22	0.960	0.58	1.69	1.49	0.590
Pb	6.71	6.41	3.90	1.78	5.41	5.03	2.35
Th	5.30	5.12	3.13	1.02	3.96	3.82	1.28
U	1.44	1.43	0.878	0.381	1.17	1.05	0.44
$^{87}Sr/^{86}Sr$	-	-	0.703899 ± 8	0.703927 ± 7	-	0.703819 ± 7	-
$^{143}Nd/^{144}Nd$	-	-	0.512746 ± 4	0.512783 ± 5	-	0.512784 ± 4	-
$^{206}Pb/^{204}Pb$	-	-	19.0427 ± 4	18.9049 ± 4	-	19.2071 ± 4	-
$^{207}Pb/^{204}Pb$	-	-	15.6406 ± 3	15.6065 ± 3	-	15.6526 ± 4	-
$^{208}Pb/^{204}Pb$	-	-	39.0552 ± 7	38.8193 ± 8	-	39.1750 ± 9	-

Table A1 *(continued)*

Sample	098VSR-01	099VSR-01	100VSR-01	101VSR-01	102VSR-01	104VSR-01	105VSR-01
Location	NELSC (III)	NELSC (III)	NELSC (IV)	NELSC (IV)	NELSC (IV)	NELSC (Ib)	NELSC (Ib)
Latitude (S)	15.41	15.43	15.43	15.44	15.45	15.27	15.30
Longitude (W)	174.27	174.29	174.29	174.30	174.31	174.21	174.22
Elevation (m)	-1812	-1669	-1745	-1780	-1873	-2033	-1981
(wt. %)	*EMP/* ***SHRIMP-SI***	*EMP/* ***SHRIMP-SI***	*EMP/* ***SHRIMP-SI***	*EMP*	*EMP/* ***SHRIMP-SI***	*EMP*	*EMP*
SiO_2	53.01	53.44	50.00	51.02	52.21	54.16	54.02
TiO_2	1.11	1.02	1.04	1.01	0.68	1.60	1.61
Al_2O_3	15.39	15.43	15.94	15.98	15.74	15.44	14.53
FeO^T	10.03	9.28	8.97	8.91	8.88	10.68	10.97
MnO	0.17	0.19	0.18	0.17	0.16	0.19	0.20
MgO	5.21	5.79	7.05	6.58	6.56	3.81	4.37
CaO	9.70	10.38	12.65	12.30	11.98	8.19	8.53
Na_2O	2.72	2.43	2.60	2.57	1.94	3.40	3.14
K_2O	0.93	0.95	0.39	0.51	0.44	1.03	1.05
P_2O_5	0.25	0.19	0.15	0.18	0.10	0.28	0.29
SO_3	0.02	0.02	0.06	0.05	0.04	0.05	0.04
Cl	0.23	0.20	0.11	0.12	0.09	0.23	0.24
H_2O	**1.15**	**1.32**	**1.37**	**-**	**1.34**	-	-
SD (2σ)	**0.56**	**0.02**	**0.11**	**-**	**0.00**	-	-
LOI	-	-	-	-	-	-	-
Total	98.71	99.29	99.11	99.38	98.81	99.01	98.93
(ppm)	*LA-ICP-MS*	*LA-ICP-MS*	*LA-ICP-MS*	*LA-ICP-MS*	*LA-ICP-MS*	*LA-ICP-MS*	*LA-ICP-MS*
Sc	22.9	26.5	28.9	29.9	32.9	21.7	24.6
V	284	283	252	266	276	341	338
Cr	12.5	33.2	67.5	107	130	6.5	8.5
Co	34.8	36.4	39.2	37.7	33.2	29.9	33.0
Ni	27.2	41.8	58.8	53.2	46.1	11.3	14.7
Cu	135	131	105	121	109	152	153
Zn	98.1	98.5	82.3	85.9	78.1	104	115
Rb	23.3	25.9	12.4	15.8	8.8	25.3	28.4
Sr	296	226	211	216	174	224	224
Y	16.3	16.3	18.7	18.3	12.1	20.5	22.5
Zr	54.9	52.9	54.7	54.3	29.3	73.8	82.7
Nb	8.97	6.47	3.08	3.91	1.68	11.5	12.9
Cs	0.377	0.499	0.239	0.260	0.187	0.393	0.368
Ba	198	176	62.7	86.0	71.2	197	219
La	11.5	8.15	4.67	5.44	3.51	10.7	12.1
Ce	25.2	19.3	11.7	13.0	8.31	24.6	27.6
Pr	2.98	2.44	1.72	1.79	1.07	3.09	3.47
Nd	12.8	11.4	7.92	8.64	5.23	14.0	14.9
Sm	2.83	2.72	2.45	2.70	1.54	3.26	3.51
Eu	0.980	0.940	0.890	0.920	0.550	1.13	1.42
Gd	2.99	3.11	3.14	3.11	1.63	4.00	4.11
Tb	0.430	0.450	0.500	0.490	0.310	0.590	0.690
Dy	3.08	2.88	3.46	3.52	2.32	3.69	4.12
Ho	0.697	0.613	0.744	0.753	0.458	0.842	0.905
Er	1.91	1.86	2.00	2.18	1.47	2.39	2.41
Tm	0.290	0.276	0.302	0.311	0.205	0.321	0.354
Yb	1.95	2.10	2.20	2.13	1.51	2.49	2.65
Lu	0.290	0.300	0.300	0.370	0.230	0.350	0.380
Hf	1.55	1.55	1.65	1.43	0.83	2.05	2.34
Ta	0.510	0.410	0.200	0.240	0.100	0.740	0.790
Pb	2.85	2.19	1.14	1.29	1.26	2.00	2.36
Th	1.62	0.968	0.484	0.616	0.421	1.29	1.46
U	0.533	0.400	0.202	0.243	0.175	0.443	0.488
$^{87}Sr/^{86}Sr$	0.703678 ± 8	0.703656 ± 7	-	-	0.703572 ± 7	-	-
$^{143}Nd/^{144}Nd$	0.512827 ± 5	0.512848 ± 5	-	-	0.512918 ± 5	-	-
$^{206}Pb/^{204}Pb$	19.0563 ± 4	19.0735 ± 3	-	-	19.1401 ± 4	-	-
$^{207}Pb/^{204}Pb$	15.6221 ± 3	15.6150 ± 3	-	-	15.6066 ± 3	-	-
$^{208}Pb/^{204}Pb$	38.9688 ± 8	38.9252 ± 7	-	-	38.8723 ± 8	-	-

Table A1 *(continued)*

Sample	106VSR-01	107VSR-01	108VSR-01	109VSR-01	111TVG-01	111TVG-02	111TVG-03
Location	NELSC (Ia)	NELSC (Ib)	NELSC (Ib)	NELSC (II)	DR	DR	DR
Latitude (S)	15.31	15.33	15.34	15.34	15.37	15.37	15.37
Longitude (W)	174.24	174.24	174.25	174.23	174.10	174.10	174.10
Elevation (m)	-1717	-1818	-1934	-1820	-1360	-1360	-1360
(wt. %)	*EMP/* ***SHRIMP-SI***	*EMP/* ***SHRIMP-SI***	*EMP/* ***SHRIMP-SI***	*EMP*	*XRF*	*EMP/* ***SHRIMP-SI***	*XRF*
SiO_2	51.81	50.83	50.34	48.52	54.39	54.23	57.28
TiO_2	0.85	1.06	0.74	1.09	0.43	0.55	0.53
Al_2O_3	15.28	15.77	15.82	15.09	13.70	15.64	15.13
FeO^T	8.44	9.48	8.56	9.21	-	8.82	-
MnO	0.16	0.17	0.16	0.17	0.16	0.16	0.14
MgO	6.93	6.36	7.28	6.87	7.65	5.99	4.57
CaO	12.22	11.58	13.30	12.67	11.19	11.40	8.98
Na_2O	2.39	2.57	2.03	3.52	1.82	1.75	2.29
K_2O	0.66	0.76	0.51	0.85	0.48	0.73	0.85
P_2O_5	0.25	0.22	0.14	0.51	0.14	0.15	0.20
SO_3	0.05	0.05	0.03	0.06	-	0.01	-
Cl	0.20	0.14	0.11	0.21	-	0.14	-
H_2O	**1.39**	**1.42**	**1.43**	-	-	**1.09**	-
SD (2σ)	**0.05**	**0.12**	**0.03**	-	-	**0.17**	-
LOI	-	-	-	-	0.65	-	0.82
Total	99.19	98.96	99.00	98.72	99.80	99.54	99.84
(ppm)	*LA-ICP-MS*	*LA-ICP-MS*	*LA-ICP-MS*	*LA-ICP-MS*	*LA-ICP-MS*	*LA-ICP-MS*	*LA-ICP-MS*
Sc	27.16	27.1	28.24	20.37	-	35.36	-
V	232	272	238	247	299	341	265
Cr	41.0	18.7	37.4	29.1	338.8	72.3	49.3
Co	37.5	40.7	37.3	38.1	-	33.9	-
Ni	51.1	45.1	52.8	52.8	59.4	33.5	34.70
Cu	87.6	126	103	94.7	-	139	-
Zn	73.6	92.1	75.6	81.6	55.4	78.8	59.9
Rb	16.6	28.5	14.8	21.5	8.60	15.6	15.0
Sr	370	231	210	759	186	216	223
Y	12.9	17.3	12.8	15.0	9.5	9.43	13.5
Zr	52.7	55.6	33.6	85.0	27.9	24.2	39.6
Nb	12.5	5.52	2.87	43.4	1.60	2.24	3.90
Cs	0.334	0.639	0.254	0.429	-	0.310	-
Ba	218	119	90.1	361	115	130	170
La	14.8	6.47	4.02	39.54	-	5.26	-
Ce	31.8	15.9	9.84	82.0	-	11.8	-
Pr	3.67	2.19	1.38	8.64	-	1.49	-
Nd	14.4	9.81	6.78	33.0	-	6.42	-
Sm	3.21	2.60	2.03	6.02	-	1.50	-
Eu	0.990	1.03	0.700	1.73	-	0.610	-
Gd	2.96	3.10	2.14	4.67	-	1.55	-
Tb	0.400	0.510	0.340	0.560	-	0.240	-
Dy	2.53	3.34	2.41	3.33	-	1.78	-
Ho	0.540	0.699	0.467	0.595	-	0.388	-
Er	1.40	2.00	1.39	1.65	-	1.19	-
Tm	0.224	0.300	0.244	0.230	-	0.166	-
Yb	1.60	1.92	1.45	1.62	-	0.970	-
Lu	0.240	0.300	0.250	0.220	-	0.160	-
Hf	1.44	1.53	0.990	1.98	-	0.670	-
Ta	0.690	0.380	0.190	2.160	-	0.130	-
Pb	3.25	1.29	1.06	5.70	<1.0	1.88	4.70
Th	2.05	0.846	0.454	4.89	<1.0	0.792	0.800
U	0.565	0.383	0.195	1.39	-	0.349	-
$^{87}Sr/^{86}Sr$	0.703907 ± 7	0.703554 ± 7	0.703415 ± 7	0.703752 ± 8	-	0.703783 ± 8	-
$^{143}Nd/^{144}Nd$	0.512786 ± 5	0.512868 ± 4	0.512914 ± 5	0.512776 ± 4	-	0.512906 ± 5	-
$^{206}Pb/^{204}Pb$	19.0442 ± 3	18.7744 ± 5	18.7912 ± 4	19.2237 ± 4	-	19.3359 ± 4	-
$^{207}Pb/^{204}Pb$	15.6374 ± 3	15.5825 ± 4	15.5905 ± 3	15.6542 ± 3	-	15.6261 ± 3	-
$^{208}Pb/^{204}Pb$	39.0511 ± 6	38.7098 ± 10	38.71367 ± 7	39.1817 ± 8	-	39.0375 ± 8	-

Table A1 *(continued)*

Sample	111TVG-03	111TVG-03	111TVG-04	111TVG-04	111TVG-05	111TVG-06	111TVG-06
Location	DR	DR	DR	DR	DR	DR	DR
Latitude (S)	15.37	15.37	15.37	15.37	15.37	15.37	15.37
Longitude (W)	174.10	174.10	174.10	174.10	174.10	174.10	174.10
Elevation (m)	-1360	-1360	-1360	-1360	-1360	-1360	-1360
(wt. %)	*XRF*	*EMP*	*XRF*	*XRF*	*XRF*	*XRF*	*XRF*
SiO_2	57.28	60.32	66.87	66.87	54.06	56.48	56.48
TiO_2	0.53	0.48	0.34	0.34	0.45	0.52	0.52
Al_2O_3	15.13	20.89	11.42	11.42	14.41	14.12	14.12
FeO^T	-	-	-	-	-	-	-
MnO	0.14	0.06	0.08	0.08	0.10	0.15	0.15
MgO	4.57	0.42	1.70	1.70	7.43	6.03	6.03
CaO	8.98	9.13	4.19	4.19	9.05	9.31	9.31
Na_2O	2.29	2.85	5.51	5.51	2.13	2.10	2.10
K_2O	0.85	1.09	0.86	0.86	0.14	0.75	0.75
P_2O_5	0.20	0.18	0.16	0.16	0.14	0.18	0.18
SO_3	-	0.02	-	-	-	-	-
Cl	-	0.22	-	-	-	-	-
H_2O	-	-	-	-	-	-	-
SD (2σ)	-	-	-	-	-	-	-
LOI	0.82	-	3.95	3.95	3.11	0.66	0.66
Total	99.84	99.52	99.88	99.88	99.82	99.82	99.82
(ppm)	*Q-ICP-MS*	-	*XRF*	*Q-ICP-MS*	*XRF*	*XRF*	*Q-ICP-MS*
Sc	33.7	-	-	14.6	-	-	36.0
V	307	-	90.0	96.6	330	290	330
Cr	49.1	-	44.5	40.8	269	214	220
Co	29.2	-	-	12.1	-	-	33.8
Ni	42.9	-	10.0	9.43	61.2	57.9	69.4
Cu	133	-	-	67.6	-	-	141
Zn	63.6	-	44.3	45.4	72.8	47.9	61.9
Rb	16.2	-	12.8	12.4	1.70	14.7	14.5
Sr	243	-	170	172	179	227	242
Y	12.4	-	15.7	14.7	9.80	15.90	11.53
Zr	35.5	-	48.0	39.5	27.1	37.2	30.0
Nb	2.90	-	3.30	2.40	1.40	3.20	2.39
Cs	0.360	-	-	0.481	-	-	0.316
Ba	198	-	207	215	20.9	157	175
La	7.11	-	-	4.34	-	-	6.20
Ce	15.1	-	-	9.24	-	-	13.30
Pr	1.94	-	-	1.25	-	-	1.75
Nd	8.26	-	-	5.78	-	-	7.55
Sm	2.03	-	-	1.69	-	-	1.88
Eu	0.67	-	-	0.51	-	-	0.63
Gd	2.11	-	-	2.13	-	-	1.97
Tb	0.341	-	-	0.369	-	-	0.319
Dy	2.28	-	-	2.55	-	-	2.13
Ho	0.483	-	-	0.562	-	-	0.454
Er	1.48	-	-	1.77	-	-	1.39
Tm	0.222	-	-	0.271	-	-	0.207
Yb	1.55	-	-	1.91	-	-	1.46
Lu	0.234	-	-	0.292	-	-	0.219
Hf	1.02	-	-	1.30	-	-	0.888
Ta	0.122	-	-	0.102	-	-	0.103
Pb	3.03	-	5.20	3.52	1.90	3.10	2.72
Th	1.16	-	<1.0	0.748	<0.9	1.20	0.975
U	0.450	-	-	0.476	-	-	0.392
$^{87}Sr/^{86}Sr$	0.703832 ± 8	0.703832 ± 8	0.704120 ± 7	0.704120 ± 7	-	-	0.703843 ± 7
$^{143}Nd/^{144}Nd$	0.512873 ± 5	0.512873 ± 5	0.512935 ± 6	0.512935 ± 6	-	-	0.512881 ± 5
$^{206}Pb/^{204}Pb$	19.3660 ± 3	19.3660 ± 3	19.2666 ± 4	19.2666 ± 4	-	-	19.3271 ± 3
$^{207}Pb/^{204}Pb$	15.6299 ± 3	15.6299 ± 3	15.6245 ± 3	15.6245 ± 3	-	-	15.6223 ± 3
$^{208}Pb/^{204}Pb$	39.0588 ± 7	39.0588 ± 7	38.9685 ± 8	38.9685 ± 8	-	-	39.0168 ± 6

Table A1 *(continued)*

Sample	111TVG-06	111TVG-07	111TVG-07	111TVG-08	111TVG-10	112TVG-01	112TVG-01
Location	DR	DR	DR	DR	DR	DR	DR
Latitude (S)	15.37	15.37	15.37	15.37	-15.37	15.40	15.40
Longitude (W)	174.10	174.10	174.10	174.10	-174.10	174.14	174.14
Elevation (m)	-1360	-1360	-1360	-1360	-1360	-1477	-1477
(wt. %)	*EMP*	*XRF*	*EMP*	*EMP*	*EMP*	*XRF*	*XRF*
SiO_2	62.93	56.11	60.52	66.49	58.27	67.34	67.34
TiO_2	0.67	0.52	0.63	0.95	0.57	0.28	0.28
Al_2O_3	17.75	14.09	17.46	14.04	15.25	10.87	10.87
FeO^T	-	-	-	-	8.46	-	-
MnO	0.05	0.15	0.11	0.09	0.15	0.09	0.09
MgO	0.36	5.98	1.24	0.22	4.13	1.15	1.15
CaO	7.25	9.45	7.92	5.77	9.00	3.56	3.56
Na_2O	2.92	2.20	2.38	2.83	2.29	5.93	5.93
K_2O	1.24	0.74	1.03	0.41	0.91	0.89	0.89
P_2O_5	0.17	0.18	0.20	0.30	0.15	0.13	0.13
SO_3	0.01	-	0.01	0.02	0.01	-	-
Cl	0.29	-	0.28	0.49	0.20	-	-
H_2O	**-**	**-**	**-**	-	-	**-**	-
SD (2σ)	**-**	**-**	**-**	-	-	**-**	-
LOI	-	0.92	-	-	-	5.22	5.22
Total	98.54	99.81	98.30	97.19	99.35	99.90	99.90
(ppm)	*LA-ICP-MS*	*XRF*	-	-	*LA-ICP-MS*	*XRF*	*Q-ICP-MS*
Sc	19.32	-	-	-	25.10	-	14.12
V	306	288	-	-	275	38.1	38.8
Cr	4.50	219	-	-	22.4	8.20	3.40
Co	21.3	-	-	-	26.4	-	8.87
Ni	7.45	58.2	-	-	32.0	<0.5	1.96
Cu	85.6	-	-	-	156	-	90.1
Zn	81.7	52.4	-	-	80.3	44.8	53.6
Rb	17.8	13.8	-	-	16.6	12.7	12.8
Sr	162	231	-	-	173	154	154
Y	12.1	14.0	-	-	9.22	16.4	14.5
Zr	31.3	38.5	-	-	24.9	41.8	35.3
Nb	2.71	2.70	-	-	2.50	1.20	2.10
Cs	0.397	-	-	-	0.390	-	0.515
Ba	168	173	-	-	150	230	205
La	7.29	-	-	-	5.26	-	3.92
Ce	15.0	-	-	-	12.5	-	8.44
Pr	1.84	-	-	-	1.54	-	1.16
Nd	8.48	-	-	-	6.17	-	5.37
Sm	1.90	-	-	-	1.58	-	1.61
Eu	0.618	-	-	-	0.570	-	0.490
Gd	1.87	-	-	-	1.54	-	2.08
Tb	0.327	-	-	-	0.240	-	0.363
Dy	2.13	-	-	-	1.87	-	2.55
Ho	0.453	-	-	-	0.384	-	0.560
Er	1.33	-	-	-	1.13	-	1.77
Tm	0.223	-	-	-	0.159	-	0.270
Yb	1.46	-	-	-	1.15	-	1.93
Lu	0.227	-	-	-	0.170	-	0.294
Hf	0.989	-	-	-	0.770	-	1.17
Ta	0.141	-	-	-	0.070	-	0.083
Pb	3.21	3.70	-	-	2.75	4.00	3.55
Th	1.07	1.10	-	-	0.781	0.700	0.664
U	0.421	-	-	-	0.357	-	0.419
$^{87}Sr/^{86}Sr$	0.703843 ± 7	-	-	-	-	0.704053 ± 8	0.704053 ± 8
$^{143}Nd/^{144}Nd$	0.512881 ± 5	-	-	-	-	0.512927 ± 5	0.512927 ± 5
$^{206}Pb/^{204}Pb$	19.3271 ± 3	-	-	-	-	19.3008 ± 3	19.3008 ± 3
$^{207}Pb/^{204}Pb$	15.6223 ± 3	-	-	-	-	15.6237 ± 2	15.6237 ± 2
$^{208}Pb/^{204}Pb$	39.0168 ± 6	-	-	-	-	38.9932 ± 6	38.9932 ± 6

Table A1 *(continued)*

Sample	112TVG-03	113TVG-01	114TVG-01	114TVG-01	116ROV-01	116ROV-02	116ROV-03
Location	DR	DR	DR	DR	NELSC (IV)	NELSC (IV)	NELSC (IV)
Latitude (S)	15.40	15.40	15.44	15.44	15.42	15.42	15.42
Longitude (W)	174.14	174.20	174.21	174.21	174.28	174.28	174.28
Elevation (m)	-1477	-2129	-2133	-2133	-1782	-1768	-1742
(wt. %)	*EMP/* ***SHRIMP-SI***	*EMP*	*XRF*	*XRF*	*EMP*	*EMP*	*EMP*
SiO_2	55.24	52.44	68.43	68.43	53.35	53.14	53.56
TiO_2	0.72	0.54	0.29	0.29	0.99	0.99	1.04
Al_2O_3	15.05	15.85	10.98	10.98	15.34	15.45	15.31
FeO^T	9.32	8.35	-	-	9.25	9.30	9.46
MnO	0.19	0.17	0.12	0.12	0.19	0.15	0.20
MgO	5.31	6.92	1.09	1.09	5.64	5.66	5.28
CaO	10.11	12.24	3.65	3.65	10.28	10.21	10.12
Na_2O	2.10	1.71	5.45	5.45	2.44	2.43	2.44
K_2O	0.72	0.47	0.89	0.89	0.95	0.95	1.01
P_2O_5	0.14	0.12	0.14	0.14	0.21	0.23	0.21
SO_3	0.02	0.02	-	-	0.02	0.01	0.02
Cl	0.12	0.08	-	-	0.20	0.20	0.20
H_2O	**0.60**	**-**	**-**	-	-	**-**	-
SD (2σ)	**0.15**	**-**	**-**	-	-	**-**	-
LOI	-	-	4.23	4.23	-	-	-
Total	99.03	98.91	99.89	99.89	98.82	98.77	98.82
(ppm)	*LA-ICP-MS*	*LA-ICP-MS*	*XRF*	*Q-ICP-MS*	-	-	-
Sc	34.6	34.5	-	14.6	-	-	-
V	289	293	41.7	42.1	-	-	-
Cr	20.8	198.7	11.1	5.21	-	-	-
Co	28.6	30.7	-	8.60	-	-	-
Ni	18.1	61.3	<0.5	5.11	-	-	-
Cu	120	141	-	63.9	-	-	-
Zn	75.9	69.0	50.5	56.5	-	-	-
Rb	13.4	10.2	13.2	13.0	-	-	-
Sr	174	158	163	161	-	-	-
Y	12.1	8.29	17.6	15.4	-	-	-
Zr	29.7	19.2	42.3	38.4	-	-	-
Nb	1.94	1.97	2.80	2.22	-	-	-
Cs	0.304	0.197	-	0.529	-	-	-
Ba	122	88.4	245	248	-	-	-
La	4.42	3.56	-	4.33	-	-	-
Ce	10.3	8.41	-	8.87	-	-	-
Pr	1.35	0.980	-	1.23	-	-	-
Nd	5.75	4.39	-	5.76	-	-	-
Sm	1.54	1.20	-	1.71	-	-	-
Eu	0.620	0.480	-	0.516	-	-	-
Gd	1.95	1.28	-	2.23	-	-	-
Tb	0.300	0.210	-	0.387	-	-	-
Dy	2.03	1.44	-	2.71	-	-	-
Ho	0.437	0.328	-	0.597	-	-	-
Er	1.34	0.940	-	1.88	-	-	-
Tm	0.200	0.162	-	0.286	-	-	-
Yb	1.47	1.06	-	2.04	-	-	-
Lu	0.230	0.140	-	0.311	-	-	-
Hf	0.970	0.620	-	1.27	-	-	-
Ta	0.100	0.090	-	0.090	-	-	-
Pb	1.85	1.38	6.30	4.53	-	-	-
Th	0.732	0.533	1.90	0.687	-	-	-
U	0.307	0.220	-	0.432	-	-	-
$^{87}Sr/^{86}Sr$	-	0.703822 ± 9	0.704067 ± 8	0.704067 ± 8	-	-	-
$^{143}Nd/^{144}Nd$	-	0.512895 ± 4	-	-	-	-	-
$^{206}Pb/^{204}Pb$	-	19.3734 ± 4	19.2998 ± 4	19.2998 ± 4	-	-	-
$^{207}Pb/^{204}Pb$	-	15.6304 ± 3	15.6241 ± 3	15.6241 ± 3	-	-	-
$^{208}Pb/^{204}Pb$	-	39.0876 ± 7	38.9936 ± 8	38.9936 ± 8	-	-	-

Table A1 *(continued)*

Sample	116ROV-04	116ROV-05	116ROV-06	116ROV-07	116ROV-08	116ROV-09	116ROV-10
Location	NELSC (IV)	NELSC (IV)	NELSC (IV)	NELSC (IV)	NELSC (IV)	NELSC (IV)	NELSC (IV)
Latitude (S)	15.42	15.42	15.42	15.42	15.42	15.42	15.42
Longitude (W)	174.28	174.28	174.28	174.28	174.28	174.28	174.28
Elevation (m)	-1721	-1692	-1676	-1649	-1610	-1604	-1570
(wt. %)	*EMP*	*EMP*	*EMP*	*EMP*	*EMP*	*EMP*	*EMP*
SiO_2	53.31	53.33	53.26	53.57	53.21	53.48	53.46
TiO_2	1.03	1.01	1.00	0.94	0.97	1.01	1.01
Al_2O_3	15.27	15.23	15.26	15.41	15.35	15.24	15.11
FeO^T	9.41	9.45	9.27	9.35	9.18	9.29	9.50
MnO	0.17	0.17	0.18	0.18	0.18	0.18	0.18
MgO	5.50	5.76	5.79	5.83	5.89	5.88	5.63
CaO	10.19	10.19	10.29	10.31	10.40	10.40	10.18
Na_2O	2.43	2.42	2.34	2.37	2.36	2.39	2.39
K_2O	0.97	0.96	0.92	0.95	0.94	0.92	0.97
P_2O_5	0.22	0.24	0.22	0.22	0.19	0.22	0.24
SO_3	0.01	0.02	0.02	0.02	0.02	0.02	0.01
Cl	0.20	0.21	0.20	0.20	0.20	0.20	0.21
H_2O	-	-	-	-	-	-	-
SD (2σ)	-	-	-	-	-	-	-
LOI	-	-	-	-	-	-	-
Total	98.68	98.92	98.71	99.30	98.84	99.19	98.86
(ppm)	-	-	-	-	-	-	-
Sc	-	-	-	-	-	-	-
V	-	-	-	-	-	-	-
Cr	-	-	-	-	-	-	-
Co	-	-	-	-	-	-	-
Ni	-	-	-	-	-	-	-
Cu	-	-	-	-	-	-	-
Zn	-	-	-	-	-	-	-
Rb	-	-	-	-	-	-	-
Sr	-	-	-	-	-	-	-
Y	-	-	-	-	-	-	-
Zr	-	-	-	-	-	-	-
Nb	-	-	-	-	-	-	-
Cs	-	-	-	-	-	-	-
Ba	-	-	-	-	-	-	-
La	-	-	-	-	-	-	-
Ce	-	-	-	-	-	-	-
Pr	-	-	-	-	-	-	-
Nd	-	-	-	-	-	-	-
Sm	-	-	-	-	-	-	-
Eu	-	-	-	-	-	-	-
Gd	-	-	-	-	-	-	-
Tb	-	-	-	-	-	-	-
Dy	-	-	-	-	-	-	-
Ho	-	-	-	-	-	-	-
Er	-	-	-	-	-	-	-
Tm	-	-	-	-	-	-	-
Yb	-	-	-	-	-	-	-
Lu	-	-	-	-	-	-	-
Hf	-	-	-	-	-	-	-
Ta	-	-	-	-	-	-	-
Pb	-	-	-	-	-	-	-
Th	-	-	-	-	-	-	-
U	-	-	-	-	-	-	-
$^{87}Sr/^{86}Sr$	-	-	-	-	-	-	-
$^{143}Nd/^{144}Nd$	-	-	-	-	-	-	-
$^{206}Pb/^{204}Pb$	-	-	-	-	-	-	-
$^{207}Pb/^{204}Pb$	-	-	-	-	-	-	-
$^{208}Pb/^{204}Pb$	-	-	-	-	-	-	-

Table A1 *(continued)*

Sample	116ROV-19	117TVG-01	118TVG-01	119TVG-01	120TVG-03	120TVG-04	122ROV-02
Location	NELSC (IV)	NELSC (II)	NELSC off-axis (III)	NELSC off-axis (III)	NELSC	NELSC	NELSC (IV)
Latitude (S)	15.42	15.37	15.38	15.41	15.47	15.47	15.43
Longitude (W)	174.28	174.24	174.31	174.24	174.26	174.26	174.29
Elevation (m)	-1544	-1412	-2015	-2028	-2031	-2031	-1689
(wt. %)	*EMP*	*EMP/* ***SHRIMP-SI***	*EMP/* ***SHRIMP-SI***	*EMP*	*EMP*	*EMP*	*EMP*
SiO_2	53.62	52.93	50.57	52.73	49.97	50.06	53.38
TiO_2	1.43	0.72	0.81	0.77	0.84	0.88	1.02
Al_2O_3	14.68	14.21	16.22	15.73	16.14	16.05	15.27
FeO^T	10.95	7.95	8.56	8.39	8.64	8.70	9.34
MnO	0.21	0.15	0.17	0.16	0.18	0.17	0.18
MgO	4.27	7.90	7.25	6.55	7.28	7.34	5.89
CaO	8.88	12.71	12.89	11.66	13.30	13.37	10.27
Na_2O	3.11	1.79	2.31	2.09	2.23	2.21	2.41
K_2O	0.93	0.77	0.54	0.72	0.35	0.35	0.96
P_2O_5	0.26	0.15	0.17	0.16	0.15	0.14	0.23
SO_3	0.05	0.01	0.05	0.02	0.09	0.08	0.03
Cl	0.25	0.14	0.13	0.15	0.07	0.07	0.20
H_2O	**-**	**1.14**	**0.96**	-	-	**1.37**	-
SD (2σ)	**-**	**0.03**	**1.26**	-	-	**0.06**	-
LOI	-	-	-	-	-	-	-
Total	98.59	99.41	99.62	99.09	99.21	99.40	99.13
(ppm)	-	*LA-ICP-MS*	*LA-ICP-MS*	*LA-ICP-MS*	*LA-ICP-MS*	*LA-ICP-MS*	-
Sc	-	33.87	31.17	29.02	33.57	33.77	-
V	-	215	214	228	261	260	-
Cr	-	242	208	72.4	172	174	-
Co	-	33.6	33.7	31.9	38.8	38.9	-
Ni	-	55.5	67.7	52.5	69.8	69.7	-
Cu	-	84.0	108	100	116	114	-
Zn	-	61.2	65.4	68.4	88.9	88.3	-
Rb	-	15.5	12.5	16.0	9.53	9.38	-
Sr	-	188	185	189	189	188	-
Y	-	9.04	12.9	10.8	14.6	14.2	-
Zr	-	35.3	34.4	34.5	37.4	36.4	-
Nb	-	6.22	2.20	4.15	2.80	2.77	-
Cs	-	0.278	0.208	0.311	0.188	0.163	-
Ba	-	151	74.1	122	88.7	88.9	-
La	-	5.61	3.83	5.33	4.01	4.00	-
Ce	-	13.1	9.72	13.0	10.0	10.0	-
Pr	-	1.71	1.41	1.57	1.45	1.45	-
Nd	-	7.32	6.34	7.31	6.40	6.64	-
Sm	-	1.81	1.91	1.75	1.83	1.65	-
Eu	-	0.61	0.71	0.57	0.70	0.69	-
Gd	-	1.72	2.13	1.97	2.20	2.16	-
Tb	-	0.290	0.350	0.310	0.380	0.380	-
Dy	-	1.83	2.45	2.09	2.76	2.74	-
Ho	-	0.366	0.538	0.438	0.551	0.534	-
Er	-	1.03	1.43	1.26	1.66	1.61	-
Tm	-	0.142	0.239	0.176	0.245	0.249	-
Yb	-	0.98	1.49	1.38	1.59	1.60	-
Lu	-	0.150	0.190	0.190	0.250	0.250	-
Hf	-	1.08	0.970	1.05	1.01	1.05	-
Ta	-	0.360	0.120	0.240	0.180	0.170	-
Pb	-	1.37	0.95	1.41	1.53	1.43	-
Th	-	0.614	0.432	0.697	0.457	0.377	-
U	-	0.217	0.223	0.253	0.188	0.189	-
$^{87}Sr/^{86}Sr$	-	0.704063 ± 7	0.703459 ± 8	0.703684 ± 7	-	0.703218 ± 7	-
$^{143}Nd/^{144}Nd$	-	0.512764 ± 5	0.512890 ± 5	0.512852 ± 5	-	0.512944 ± 5	-
$^{206}Pb/^{204}Pb$	-	18.8412 ± 3	18.6835 ± 3	19.0873 ± 3	-	18.7777 ± 3	-
$^{207}Pb/^{204}Pb$	-	15.6049 ± 2	15.5658 ± 2	15.6131 ± 2	-	15.5841 ± 3	-
$^{208}Pb/^{204}Pb$	-	38.7740 ± 6	38.6063 ± 6	38.9256 ± 6	-	38.6872 ± 6	-

Table A1 *(continued)*

Sample	122ROV-03	122ROV-04	122ROV-05	122ROV-06	122ROV-07	122ROV-08	122ROV-09
Location	NELSC (IV)	NELSC (IV)	NELSC (IV)	NELSC (IV)	NELSC (IV)	NELSC (IV)	NELSC (IV)
Latitude (S)	15.43	15.42	15.42	15.42	15.42	15.42	15.42
Longitude (W)	174.29	174.29	174.29	174.29	174.29	174.29	174.29
Elevation (m)	-1681	-1661	-1651	-1629	-1608	-1592	-1579
(wt. %)	*EMP*	*EMP*	*EMP*	*EMP*	*EMP*	*EMP*	*EMP*
SiO_2	53.40	53.41	53.23	53.48	53.99	53.86	54.00
TiO_2	1.00	1.03	1.01	0.98	1.08	1.05	1.07
Al_2O_3	15.23	15.25	15.24	15.30	15.28	15.13	15.20
FeO^T	9.32	9.44	9.27	9.30	9.62	9.55	9.64
MnO	0.18	0.17	0.17	0.17	0.16	0.17	0.18
MgO	5.94	5.94	5.92	5.86	5.16	5.54	5.30
CaO	10.32	10.20	10.38	10.36	9.89	10.08	9.95
Na_2O	2.32	2.31	2.37	2.37	2.53	2.45	2.53
K_2O	0.96	0.99	0.95	0.96	1.03	0.99	1.00
P_2O_5	0.22	0.22	0.21	0.23	0.25	0.25	0.24
SO_3	0.02	0.02	0.02	0.01	0.02	0.02	0.02
Cl	0.20	0.20	0.20	0.20	0.22	0.21	0.22
H_2O	-	-	-	-	-	-	-
SD (2σ)	-	-	-	-	-	-	-
LOI	-	-	-	-	-	-	-
Total	99.07	99.13	98.92	99.20	99.19	99.26	99.30
(ppm)	-	-	-	-	-	-	-
Sc	-	-	-	-	-	-	-
V	-	-	-	-	-	-	-
Cr	-	-	-	-	-	-	-
Co	-	-	-	-	-	-	-
Ni	-	-	-	-	-	-	-
Cu	-	-	-	-	-	-	-
Zn	-	-	-	-	-	-	-
Rb	-	-	-	-	-	-	-
Sr	-	-	-	-	-	-	-
Y	-	-	-	-	-	-	-
Zr	-	-	-	-	-	-	-
Nb	-	-	-	-	-	-	-
Cs	-	-	-	-	-	-	-
Ba	-	-	-	-	-	-	-
La	-	-	-	-	-	-	-
Ce	-	-	-	-	-	-	-
Pr	-	-	-	-	-	-	-
Nd	-	-	-	-	-	-	-
Sm	-	-	-	-	-	-	-
Eu	-	-	-	-	-	-	-
Gd	-	-	-	-	-	-	-
Tb	-	-	-	-	-	-	-
Dy	-	-	-	-	-	-	-
Ho	-	-	-	-	-	-	-
Er	-	-	-	-	-	-	-
Tm	-	-	-	-	-	-	-
Yb	-	-	-	-	-	-	-
Lu	-	-	-	-	-	-	-
Hf	-	-	-	-	-	-	-
Ta	-	-	-	-	-	-	-
Pb	-	-	-	-	-	-	-
Th	-	-	-	-	-	-	-
U	-	-	-	-	-	-	-
$^{87}Sr/^{86}Sr$	-	-	-	-	-	-	-
$^{143}Nd/^{144}Nd$	-	-	-	-	-	-	-
$^{206}Pb/^{204}Pb$	-	-	-	-	-	-	-
$^{207}Pb/^{204}Pb$	-	-	-	-	-	-	-
$^{208}Pb/^{204}Pb$	-	-	-	-	-	-	-

Table A1 *(continued)*

Sample	122ROV-10	122ROV-11	122ROV-12	122ROV-23	124TVG-01	124TVG-01	125TVG-02
Location	NELSC (IV)	NELSC (IV)	NELSC (IV)	NELSC (IV)	smt	smt	smt
Latitude (S)	15.42	15.42	15.42	15.42	15.68	15.68	15.71
Longitude (W)	174.28	174.28	174.28	174.28	174.52	174.52	174.48
Elevation (m)	-1532	-1550	-1537	-1534	-2031	-2031	-1259
(wt. %)	*EMP*	*EMP*	*EMP*	*EMP*	*EMP/* ***SHRIMP-SI***	*XRF*	*XRF*
SiO_2	53.95	53.77	53.20	48.38	49.26	48.25	46.37
TiO_2	1.08	1.06	1.05	0.02	0.75	0.65	0.64
Al_2O_3	15.15	15.15	15.11	31.79	16.42	16.15	14.62
FeO^T	9.64	9.59	9.47	0.90	8.82	8.31	8.17
MnO	0.18	0.18	0.17	0.00	0.17	0.17	0.16
MgO	5.41	5.54	5.40	0.21	7.35	8.71	8.99
CaO	9.97	10.06	10.05	16.26	13.76	13.94	13.34
Na_2O	2.51	2.52	2.38	2.25	2.23	2.09	2.01
K_2O	1.00	0.99	1.00	0.09	0.47	0.42	0.62
P_2O_5	0.24	0.23	0.22	0.01	0.10	0.18	0.20
SO_3	0.02	0.01	0.02	0.00	0.07	-	-
Cl	0.21	0.21	0.21	0.01	0.12	-	-
H_2O	**-**	**-**	**-**	-	**1.40**	**-**	**-**
SD (2σ)	**-**	**-**	**-**	-	**0.05**	**-**	**-**
LOI	-	-	-	-	-	0.01	3.76
Total	99.32	99.26	98.26	99.91	99.49	98.88	98.88
(ppm)	-	-	-	-	*LA-ICP-MS*	*Q-ICP-MS*	*Q-ICP-MS*
Sc	-	-	-	-	31.6	45.4	-
V	-	-	-	-	259	266	245
Cr	-	-	-	-	108	401	392
Co	-	-	-	-	41.9	44.7	-
Ni	-	-	-	-	60.5	116	128
Cu	-	-	-	-	129	129	-
Zn	-	-	-	-	78.9	43.8	46.4
Rb	-	-	-	-	13.8	7.80	14.5
Sr	-	-	-	-	205	248	220
Y	-	-	-	-	13.9	12.2	16.7
Zr	-	-	-	-	34.8	36.0	42.6
Nb	-	-	-	-	3.0	2.7	2.7
Cs	-	-	-	-	0.233	0.172	-
Ba	-	-	-	-	72.7	75.1	116
La	-	-	-	-	3.81	3.63	-
Ce	-	-	-	-	9.25	9.54	-
Pr	-	-	-	-	1.34	1.34	-
Nd	-	-	-	-	6.29	6.27	-
Sm	-	-	-	-	1.83	1.82	-
Eu	-	-	-	-	0.700	0.749	-
Gd	-	-	-	-	2.28	2.11	-
Tb	-	-	-	-	0.360	0.369	-
Dy	-	-	-	-	2.55	2.43	-
Ho	-	-	-	-	0.517	0.517	-
Er	-	-	-	-	1.6	1.53	-
Tm	-	-	-	-	0.243	0.223	-
Yb	-	-	-	-	1.67	1.51	-
Lu	-	-	-	-	0.240	0.216	-
Hf	-	-	-	-	0.840	0.919	-
Ta	-	-	-	-	0.150	0.150	-
Pb	-	-	-	-	0.954	0.886	0.800
Th	-	-	-	-	0.418	0.422	<1.0
U	-	-	-	-	0.284	0.281	-
$^{87}Sr/^{86}Sr$	-	-	-	-	-	-	-
$^{143}Nd/^{144}Nd$	-	-	-	-	-	-	-
$^{206}Pb/^{204}Pb$	-	-	-	-	-	-	-
$^{207}Pb/^{204}Pb$	-	-	-	-	-	-	-
$^{208}Pb/^{204}Pb$	-	-	-	-	-	-	-

Table A1 *(continued)*

Sample	125TVG-03	125TVG-04	125TVG-05	126TVG-01	126TVG-02	129VSR-01	130VSR-01
Location	smt	smt	smt	smt	smt	NELSC (IV)	NELSC (IV)
Latitude (S)	15.71	15.71	15.71	15.71	15.71	15.50	15.49
Longitude (W)	174.48	174.48	174.48	174.45	174.45	174.35	174.36
Elevation (m)	-1259	-1259	-1259	-1210	-1210	-2173	-2278
(wt. %)	*XRF*	*XRF*	*EMP/* ***SHRIMP-SI***	*XRF*	*XRF*	*EMP/* ***SHRIMP-SI***	*EMP/* ***SHRIMP-SI***
SiO_2	49.01	48.57	49.81	49.32	48.82	49.44	49.40
TiO_2	0.72	0.72	0.82	0.90	0.93	0.76	0.80
Al_2O_3	16.53	16.37	15.97	17.76	17.14	16.21	16.14
FeO^T	8.57	8.78	9.66	6.99	8.08	8.68	8.85
MnO	0.17	0.17	0.20	0.12	0.17	0.17	0.17
MgO	7.17	7.22	6.88	6.21	6.25	7.49	7.39
CaO	13.55	13.68	12.99	13.56	13.05	13.75	13.59
Na_2O	2.21	2.36	2.21	2.30	2.50	2.15	2.21
K_2O	0.71	0.73	0.83	1.57	1.59	0.31	0.32
P_2O_5	0.24	0.25	0.20	0.31	0.38	0.12	0.12
SO_3	-	-	0.03	-	-	0.08	0.08
Cl	-	-	0.15	-	-	0.07	0.08
H_2O	-	-	**1.11**	**-**	-	**1.45**	**1.48**
SD (2σ)	-	-	**0.03**	**-**	-	**0.04**	**0.02**
LOI	0.00	0.00	-	0.00	0.03	-	-
Total	98.88	98.85	99.72	99.04	98.94	99.22	99.15
(ppm)	*Q-ICP-MS*	*Q-ICP-MS*	*LA-ICP-MS*	*Q-ICP-MS*	*Q-ICP-MS*	*LA-ICP-MS*	*LA-ICP-MS*
Sc	-	43.71	29.51	-	36.83	32.55	34.47
V	256	317	291	256	322	262	277
Cr	72.8	72.3	24.5	51.8	36.4	213	150
Co	-	44.4	44.1	-	41.6	39.1	41.8
Ni	52.8	64.5	49.9	55.7	66.01	68.90	66.4
Cu	-	110	152	-	105	115	126
Zn	48.6	54.4	89.7	48.6	62.9	73.4	75.7
Rb	19.8	18.7	28.6	36.7	39.3	6.9	7.6
Sr	241	280	222	335	401	154	167
Y	20.6	14.6	16.5	20.0	15.1	14.1	16.4
Zr	42.0	39.6	39.4	56.2	59.6	30.5	35
Nb	0.70	2.52	2.56	5.70	6.00	1.56	1.89
Cs	-	0.389	0.546	-	1.15	0.142	0.142
Ba	107	115	101	224	281	46.4	53.4
La	-	5.10	5.08	-	12.3	2.88	3.20
Ce	-	13.4	12.2	-	29.6	7.67	8.54
Pr	-	1.84	1.68	-	3.78	1.08	1.25
Nd	-	8.45	8.13	-	16.7	5.45	6.18
Sm	-	2.34	2.28	-	4.30	1.54	2.05
Eu	-	0.911	0.860	-	1.56	0.660	0.710
Gd	-	2.57	2.90	-	4.16	2.05	2.38
Tb	-	0.438	0.440	-	0.636	0.350	0.390
Dy	-	2.90	2.96	-	3.90	2.59	2.91
Ho	-	0.616	0.657	-	0.798	0.540	0.693
Er	-	1.85	1.80	-	2.33	1.64	1.95
Tm	-	0.270	0.290	-	0.333	0.244	0.281
Yb	-	1.86	1.89	-	2.25	1.63	2.08
Lu	-	0.267	0.300	-	0.316	0.280	0.300
Hf	-	1.05	1.11	-	1.53	0.930	1.04
Ta	-	0.135	0.130	-	0.284	0.090	0.120
Pb	1.10	1.28	1.39	2.20	3.44	0.681	0.862
Th	2.90	0.696	0.724	1.30	1.59	0.295	0.368
U	-	0.472	0.462	-	0.966	0.152	0.135
$^{87}Sr/^{86}Sr$	-	-	0.703512 ± 7	-	-	-	0.703180 ± 7
$^{143}Nd/^{144}Nd$	-	-	0.512884 ± 6	-	-	-	0.512998 ± 5
$^{206}Pb/^{204}Pb$	-	-	18.7223 ± 3	-	-	-	18.7179 ± 3
$^{207}Pb/^{204}Pb$	-	-	15.5666 ± 2	-	-	-	15.5612 ± 3
$^{208}Pb/^{204}Pb$	-	-	38.5915 ± 6	-	-	-	38.5376 ± 7

Table A1 *(continued)*

Sample	D120-2-1	M2212-2	M2218-10	M2218-12	M2218-7	M2218-8
Location	NELSC	MTJ	MTJ	MTJ	MTJ	MTJ
Latitude (S)	-	-	-	-	-	-
Longitude (W)	-	-	-	-	-	-
Elevation (m)	-	-	-	-	-	-
(wt. %)	*EMP*	*EMP*	*EMP*	*EMP*	*EMP*	*EMP*
SiO_2	54.47	50.51	50.31	52.80	51.07	50.28
TiO_2	1.10	1.06	1.07	1.80	1.28	0.98
Al_2O_3	15.48	15.76	16.10	14.89	15.52	16.00
FeO^T	9.24	9.04	8.90	11.44	9.95	8.51
MnO	0.17	0.17	0.19	0.21	0.18	0.16
MgO	4.72	7.06	8.09	4.51	6.22	7.42
CaO	9.35	12.44	12.40	9.22	11.26	12.80
Na_2O	2.59	2.49	2.55	3.41	2.86	2.40
K_2O	0.89	0.27	0.15	0.50	0.28	0.28
P_2O_5	0.24	0.12	0.10	0.23	0.16	0.13
SO_3	0.05	0.25	0.25	0.19	0.26	0.23
Cl	0.20	0.06	0.01	0.09	0.05	0.03
H_2O	-	-	-	-	-	-
SD (2σ)	-	-	-	-	-	-
LOI	-	-	-	-	-	-
Total	98.45	99.21	100.13	99.27	99.08	99.19
(ppm)	*LA-ICP-MS*	*LA-ICP-MS*	*LA-ICP-MS*	*LA-ICP-MS*	*LA-ICP-MS*	*LA-ICP-MS*
Sc	25.89	33.29	33.78	30.59	30.33	30.97
V	299	251	231	347	260	226
Cr	8.40	156	310	14.0	32.3	261
Co	28.2	39.6	42.1	34.0	38.2	36.0
Ni	20.2	55.0	96.6	8.49	27.9	69.5
Cu	141	84.1	74.6	36.9	55.8	73.1
Zn	86.8	80.4	77.7	112	87.7	69.5
Rb	22.4	7.20	4.08	13.7	6.88	8.17
Sr	228	126	111	132	120	117
Y	15.4	20.7	21.0	32.1	23.7	17.0
Zr	56.5	51.3	54.4	85.6	63.2	44.1
Nb	10.3	2.09	1.88	3.69	2.55	1.70
Cs	0.369	0.128	0.101	0.258	0.159	0.284
Ba	189	37.7	25.2	63.7	39.7	31.8
La	10.2	3.22	3.16	5.24	3.87	2.72
Ce	23.3	8.86	8.58	15.2	10.9	8.22
Pr	2.75	1.37	1.35	2.29	1.55	1.26
Nd	11.5	7.16	6.80	11.35	8.41	6.54
Sm	2.60	2.08	2.31	3.97	2.53	2.11
Eu	1.02	0.830	0.870	1.31	0.990	0.790
Gd	2.72	2.85	3.27	4.82	3.77	2.75
Tb	0.440	0.520	0.590	0.810	0.620	0.450
Dy	2.94	3.78	4.13	5.69	4.69	3.13
Ho	0.604	0.840	0.849	1.253	0.895	0.727
Er	1.79	2.44	2.39	3.72	2.51	2.09
Tm	0.251	0.353	0.401	0.561	0.437	0.300
Yb	1.68	2.3	2.53	3.75	2.9	1.97
Lu	0.230	0.330	0.390	0.570	0.440	0.330
Hf	1.43	1.32	1.40	2.57	1.89	1.27
Ta	0.570	0.160	0.130	0.230	0.160	0.130
Pb	2.15	0.660	0.625	1.05	0.867	0.565
Th	1.34	0.258	0.251	0.537	0.355	0.275
U	0.461	0.123	0.078	0.237	0.133	0.150
$^{87}Sr/^{86}Sr$	-	-	0.703512	-	-	-
$^{143}Nd/^{144}Nd$	-	-	0.512884	-	-	-
$^{206}Pb/^{204}Pb$	-	-	18.7223	-	-	-
$^{207}Pb/^{204}Pb$	-	-	15.5666	-	-	-
$^{208}Pb/^{204}Pb$	-	-	38.5915	-	-	-

Table A2 *H_2O and trace element contents of lavas from cruises SO67 and SO167 from the southernmost VFR. Analytical methods in italics. Major elements and Sr-Nd-Pb isotope ratios from Fretzdorff et al., 2006 and Haase et al., 2009.*

Sample	77OFOS	78DR-03	79DR-01	225KD	227GA-01	229KD	235GA
Cruise	SO167	SO167	SO167	SO67	SO67	SO67	SO67
Latitude (S)	22.85	22.85	22.84	22.84	22.82	22.79	22.88
Longitude (W)	176.75	176.74	176.78	176.78	176.81	176.88	176.69
Elevation (m)	-2213	-2247	-2376	-2073	-2293	-2447	-1819
(wt. %)	***SHRIMP-SI***	***SHRIMP-SI***	***SHRIMP-SI***	***SHRIMP-SI***	***SHRIMP-SI***	***SHRIMP-SI***	***SHRIMP-SI***
SiO_2	59.33	59.53	54.07	53.82	50.94	53.43	51.20
TiO_2	1.39	1.34	0.80	0.67	0.71	0.86	0.84
Al_2O_3	14.58	14.69	14.50	16.96	15.14	16.14	15.75
FeO^T	9.06	9.16	10.48	9.53	8.54	8.66	10.46
MnO	0.19	0.20	0.18	0.17	0.16	0.16	0.45
MgO	2.04	2.09	5.08	5.35	9.27	7.66	6.48
CaO	5.99	6.23	10.04	10.92	12.44	10.47	11.82
Na_2O	3.50	4.01	1.69	1.61	1.82	2.00	1.79
K_2O	0.57	0.58	0.33	0.30	0.36	0.38	0.51
P_2O_5	0.42	0.35	0.15	0.07	0.09	0.11	0.13
SO_2	0.03	-	0.01	-	-	-	-
Cl	1,961.33	-	934.29	-	-	-	-
H_2O	**1.33**	**0.43**	**1.37**	**1.29**	**1.41**	**1.59**	**1.35**
SD (2σ)	**0.14**	**0.39**	**0.15**	**0.38**	**0.02**	**0.03**	**0.01**
LOI	-	0.45	-	-	-	-	-
Total	97.10	98.18	97.33	99.40	99.47	99.87	99.43
(ppm)	*LA-ICP-MS*	*LA-ICP-MS*	*LA-ICP-MS*	*LA-ICP-MS*	*LA-ICP-MS*	*LA-ICP-MS*	*LA-ICP-MS*
Sc	28.3	29.3	46.3	51.3	40.2	42.6	44.0
V	60.2	-	373	414	283	347	331
Cr	-	-	16.7	10.4	122	108	-
Co	16.5	-	39.0	42.4	38.0	33.7	42.5
Ni	-	-	26.0	25.8	52.5	32.7	38.0
Cu	23.5	36.3	180	208	128	97.0	147
Zn	127	127	100	109	77.6	93.0	85.6
Rb	10.6	10.7	4.79	5.40	6.57	6.64	7.88
Sr	178	181	157	173	182	183	236
Y	38.5	39.7	16.8	19.2	16.8	19.2	15.8
Zr	86.8	90.9	27.1	31.2	30.1	41.4	28.8
Nb	1.24	1.31	0.295	0.324	0.455	0.396	0.406
Cs	0.645	-	-	-	-	-	-
Ba	135	141	104	117	80.0	89.1	104
La	5.83	6.04	2.22	2.56	2.91	3.22	3.40
Ce	16.5	17.0	5.91	6.64	7.36	8.81	8.57
Pr	2.66	2.68	0.913	1.09	1.15	1.39	1.31
Nd	13.8	14.3	5.08	5.71	6.15	7.95	6.84
Sm	4.52	4.67	1.79	2.12	2.17	2.61	2.18
Eu	1.60	1.66	0.682	0.784	0.806	0.932	0.853
Gd	6.11	6.07	2.38	2.91	2.77	3.20	2.87
Tb	0.986	1.03	0.411	0.485	0.436	0.506	0.441
Dy	6.70	7.06	2.86	3.38	2.97	3.48	2.81
Ho	1.42	1.50	0.636	0.725	0.630	0.696	0.623
Er	4.40	4.49	1.98	2.11	1.95	2.18	1.73
Tm	0.610	0.653	0.298	0.314	0.249	0.313	0.239
Yb	4.29	4.47	1.91	2.19	1.84	2.02	1.74
Lu	0.632	0.676	0.298	0.327	0.272	0.293	0.248
Hf	2.79	2.84	0.978	1.25	1.05	1.40	1.09
Ta	0.090	0.084	-	0.024	0.032	0.034	0.026
Pb	1.73	1.76	1.29	1.37	1.13	1.31	1.32
Th	0.504	0.563	0.281	0.321	0.356	0.356	0.449
U	0.225	0.242	0.140	0.161	0.154	0.168	0.190
$^{87}Sr/^{86}Sr$	0.703316	0.703296	0.703362	-	0.703313	-	0.703278
$^{143}Nd/^{144}Nd$	0.513043	0.513057	0.513061	-	0.513042	-	0.513039
$^{206}Pb/^{204}Pb$	18.653	18.701	18.6860	-	18.65	-	18.71
$^{207}Pb/^{204}Pb$	15.522	15.528	15.5320	-	15.52	-	15.521
$^{208}Pb/^{204}Pb$	38.225	38.515	38.2140	-	38.222	-	38.19

Table A3 *Uranium-series analyses from the southernmost VFR including errors and analytical methods in italics. Activity ratios in brackets. Reference values for accuracy calculations from Scott et al. 2019, values marked with * from Sims et al., 2013.*

Sample	77OFOS	78DR-03	79DR-01	225KD	227GA-01	229KD	235GA
Cruise	SO167	SO167	SO167	SO67	SO67	SO67	SO67
Latitude (S)	22.85	22.85	22.84	22.84	22.82	22.79	22.88
Longitude (W)	176.75	176.74	176.78	176.78	176.81	176.88	176.69
Elevation (m)	-2213	-2247	-2376	-2073	-2293	-2447	-1819
(ppm)	*MC-ICP-MS*	*MC-ICP-MS*	*MC-ICP-MS*	*MC-ICP-MS*	*MC-ICP-MS*	*MC-ICP-MS*	*MC-ICP-MS*
[Th]	0.538	0.545	0.287	0.294	0.383	0.360	0.479
err. Abs.	*0.006*	*0.006*	*0.003*	*0.003*	*0.004*	*0.004*	*0.005*
[U]	0.235	0.237	0.131	0.130	0.144	0.143	0.188
err. Abs.	*0.003*	*0.003*	*0.001*	*0.001*	*0.002*	*0.002*	*0.002*
(fmol/g)	*MC-ICP-MS*	*MC-ICP-MS*	*MC-ICP-MS*	*MC-ICP-MS*	*MC-ICP-MS*	*MC-ICP-MS*	*MC-ICP-MS*
^{230}Th	14.473	14.428	7.569	7.622	9.756	10.003	12.684
err. Abs.	*0.164*	*0.163*	*0.086*	*0.086*	*0.111*	*0.113*	*0.144*
(^{230}Th/^{232}Th)	1.156	1.137	1.133	1.113	1.093	1.192	1.138
2σ	*0.007*	*0.007*	*0.007*	*0.007*	*0.007*	*0.007*	*0.007*
(^{238}U/^{232}Th)	1.328	1.319	1.384	1.344	1.138	1.201	1.191
2σ	*0.021*	*0.021*	*0.022*	*0.021*	*0.018*	*0.019*	*0.019*
(^{238}U/^{230}Th)	1.149	1.160	1.221	1.207	1.041	1.007	1.047
2σ	*0.018*	*0.019*	*0.019*	*0.019*	*0.017*	*0.016*	*0.017*
(^{230}Th/^{238}U)	0.870	0.862	0.819	0.828	0.960	0.993	0.955
(^{234}U/^{238}U)	0.998	0.997	0.983	0.994	1.011	1.008	0.998
2σ	*0.004*	*0.004*	*0.004*	*0.004*	*0.005*	*0.005*	*0.004*
(fg/g)	*TIMS*	*TIMS*	*TIMS*	*TIMS*	*TIMS*	*TIMS*	*TIMS*
^{226}Ra	264.729	272.804	43.275	49.967	97.523	90.363	102.836
err. Abs.	*5.849*	*6.073*	*0.963*	*1.111*	*2.174*	*1.998*	*2.275*
(^{226}Ra/^{230}Th)	3.824	3.954	1.196	1.371	2.090	1.889	1.695
2σ	*0.086*	*0.090*	*0.027*	*0.031*	*0.048*	*0.043*	*0.038*

Table A3 *(continued)*

Sample	BCR-2	Accuracy (%)	
Cruise	-	-	
Latitude (S)	-	-	
Longitude (W)	-	-	
Elevation (m)	-	-	
(ppm)	*MC-ICP-MS*	-	
[Th]	5.819	-0.137	
err. Abs.	*0.065*	-	
[U]	1.728	2.549	
err. Abs.	*0.019*	-	
(fmol/g)	*MC-ICP-MS*	-	
^{230}Th	117.900	-1.987*	
err. Abs.	*1.335*	-	
(^{230}Th/^{232}Th)	0.870	-1.000	
2σ	*0.005*	-	
(^{238}U/^{232}Th)	0.901	2.738	
2σ	*0.014*	-	
(^{238}U/^{230}Th)	1.035	3.851	
2σ	*0.017*	-	
(^{230}Th/^{238}U)	-	-	
(^{234}U/^{238}U)	0.996	-0.667*	
2σ	*0.004*	-	
(fg/g)	*TIMS*	-	
^{226}Ra	568.000	0.353	
err. Abs.	*12.903*	-	
(^{226}Ra/^{230}Th)	1.006	1.329	
2σ	*0.023*	-	

Table A4 *EMP and XRF standard analyses during measurements of glasses and whole-rocks of the NELSC area. Standard deviation and analytical methods in italics.*

Sample	VG-2 (n=34)	VG-99I (n=35)	VG-99II (n=24)	VG-568 (n=39)	BE-N (n=10)	GA (n=10)
(wt. %)	*EMP*	*EMP*	*EMP*	*EMP*	*XRF*	*XRF*
SiO_2	50.251	50.897	50.238	76.580	38.567	69.899
SD (σ)	*0.479*	*0.452*	*0.554*	*1.252*	*0.072*	*0.044*
TiO_2	1.840	4.092	4.085	0.072	2.607	0.369
SD (σ)	*0.067*	*0.113*	*0.103*	*0.021*	*0.005*	*0.001*
Al_2O_3	14.059	12.635	12.590	12.249	10.370	14.633
SD (σ)	*0.195*	*0.179*	*0.248*	*0.249*	*0.036*	*0.044*
Fe_2O_3	-	-	-	-	12.654	2.656
SD (σ)	-	-	-	-	*0.025*	*0.009*
FeO	11.637	13.227	13.212	1.174	-	-
SD (σ)	*0.104*	*0.104*	*0.117*	*0.093*	-	-
MnO	0.213	0.194	0.205	0.023	0.204	0.087
SD (σ)	*0.031*	*0.029*	*0.028*	*0.019*	*0.001*	*0.000*
MgO	6.883	4.981	4.899	0.032	12.943	0.933
SD (σ)	*0.092*	*0.062*	*0.116*	*0.008*	*0.069*	*0.008*
CaO	11.241	9.350	9.321	0.468	13.866	2.425
SD (σ)	*0.085*	*0.077*	*0.074*	*0.021*	*0.029*	*0.007*
Na_2O	2.793	2.848	2.823	3.631	3.272	3.736
SD (σ)	*0.079*	*0.070*	*0.087*	*0.581*	*0.055*	*0.029*
K_2O	0.187	0.829	0.825	4.806	1.371	4.018
SD (σ)	*0.017*	*0.026*	*0.021*	*0.080*	*0.006*	*0.011*
P_2O_5	0.206	0.454	0.438	0.037	1.199	0.157
SD (σ)	*0.035*	*0.047*	*0.042*	*0.028*	*0.011*	*0.005*
SO_3	0.028	0.022	0.020	0.103	-	-
SD (σ)	*0.007*	*0.005*	*0.005*	*0.009*	-	-
Cl	0.359	0.038	0.035	0.006	-	-
SD (σ)	*0.021*	*0.017*	*0.013*	*0.009*	-	-
LOI	-	-	-	-	2.440	0.880
	-	-	-	-	*0.000*	*0.000*
Total	99.689	99.562	98.686	99.157	99.493	99.793
SD (σ)	*0.517*	*0.607*	*0.832*	*1.339*	*0.012*	*0.005*
Ba	-	-	-	-	963.490	839.010
SD (σ)	-	-	-	-	*9.465*	*15.384*
Cr	-	-	-	-	327.110	10.610
SD (σ)	-	-	-	-	*4.540*	*2.327*
Ga	-	-	-	-	17.980	16.940
SD (σ)	-	-	-	-	*1.585*	*1.124*
Nb	-	-	-	-	102.270	10.950
SD (σ)	-	-	-	-	*1.308*	*1.116*
Ni	-	-	-	-	270.600	8.670
SD (σ)	-	-	-	-	*4.109*	*2.203*
Pb	-	-	-	-	5.680	30.380
SD (σ)	-	-	-	-	*1.119*	*1.385*
Rb	-	-	-	-	46.620	171.170
SD (σ)	-	-	-	-	*0.781*	*1.046*
Sr	-	-	-	-	1395.100	300.200
SD (σ)	-	-	-	-	*4.654*	*1.208*
Th	-	-	-	-	10.020	17.490
SD (σ)	-	-	-	-	*1.900*	*1.327*
V	-	-	-	-	207.090	46.210
SD (σ)	-	-	-	-	*18.113*	*6.471*
Y	-	-	-	-	29.240	18.690
SD (σ)	-	-	-	-	*1.539*	*0.860*
Zn	-	-	-	-	102.800	65.100
SD (σ)	-	-	-	-	*1.652*	*1.206*
Zr	-	-	-	-	262.620	145.000
SD (σ)	-	-	-	-	*2.833*	*1.187*

Table A5 *Average LA-ICP-MS standard analyses at GZN and MQU of the international rock standard BCR-2G. Standard deviation and accuracy in italics. Reference values for accuracy from GeoREM .*

Sample	BCR-2G **GZN**	SD	Accuracy %	BCR-2G **MQU**	SD	Accuracy %
	(n=3)	(σ)	GeoREM	(n=9)	(σ)	GeoREM
Li7	10.290	*1.217*	*14.333*	*10.111*	*0.292*	*12.346*
Sc45	29.867	*0.850*	*-9.495*	40.563	*6.580*	*22.919*
V51	437.000	*9.798*	*2.824*	*439.446*	*3.782*	*3.399*
Cr53	18.500	*0.800*	*8.824*	15.362	*0.820*	*-9.634*
Mn55	1658.667	*26.411*	*7.011*	*1573.458*	*23.006*	*1.513*
Co59	39.933	*1.173*	*5.088*	39.720	*0.633*	*4.526*
Ni60	12.800	*0.668*	*-1.538*	*13.863*	*2.633*	*6.641*
Cu63	17.267	*0.759*	*-17.778*	19.076	*0.428*	*-9.164*
Zn66	168.667	*4.110*	*34.933*	162.908	*3.696*	*30.326*
As75	1.757	*0.109*	-	0.952	*0.099*	-
Se77	-	-	-	-	-	-
Rb85	50.400	*1.871*	*7.234*	50.182	*0.656*	*6.771*
Sr88	307.667	*4.028*	*-10.039*	*335.310*	*2.995*	*-1.956*
Y89	29.900	*0.668*	*-14.571*	31.409	*0.669*	*-10.260*
Zr90	153.667	*1.247*	*-16.486*	*170.046*	*4.489*	*-7.584*
Nb93	11.800	*0.082*	*-5.600*	11.946	*0.152*	*-4.436*
Mo95	284.667	*10.339*	*5.432*	*267.668*	*4.431*	*-0.864*
Rh103	-	-	-	0.016	*0.004*	-
Pd105	0.195	*0.065*		*0.202*	*0.078*	-
Ag107	0.736	*0.072*	-	0.271	*0.060*	*-45.822*
Cd111	0.385	*0.126*	*92.333*	*0.429*	*0.109*	*114.389*
Sb121	0.328	*0.005*	*-6.381*	0.346	*0.042*	*-1.048*
Te125	0.310	*0.000*	-	*0.430*	*0.000*	-
Cs133	1.240	*0.057*	*6.897*	1.215	*0.048*	*4.703*
Ba137	633.667	*9.463*	*-7.223*	*689.361*	*4.863*	*0.931*
La139	23.400	*0.432*	*-5.263*	24.377	*0.397*	*-1.309*
Ce140	51.333	*0.793*	*-3.690*	*53.074*	*0.323*	*-0.423*
Pr141	6.257	*0.123*	*-6.617*	6.631	*0.082*	*-1.028*
Nd146	26.267	*0.910*	*-9.112*	27.691	*0.414*	*-4.183*
Sm147	5.870	*0.130*	*-10.926*	6.427	*0.188*	*-2.479*
Eu153	1.920	*0.054*	*-2.538*	*1.981*	*0.077*	*0.581*
Gd157	6.107	*0.321*	*-8.992*	6.597	*0.292*	*-1.689*
Tb159	0.900	*0.012*	*-11.732*	0.937	*0.047*	*-8.159*
Dy163	6.210	*0.203*	*-3.571*	5.887	*0.190*	*-8.592*
Ho165	1.193	*0.005*	*-6.037*	1.170	*0.047*	*-7.848*
Er166	3.353	*0.128*	*-9.369*	3.408	*0.117*	*-7.898*
Tm169	0.481	*0.024*	*-5.752*	0.472	*0.018*	*-7.451*
Yb172	3.350	*0.212*	*-1.180*	3.130	*0.161*	*-7.670*
Lu175	0.457	*0.025*	*-9.079*	0.456	*0.025*	*-9.278*
Hf178	4.430	*0.036*	*-8.471*	4.697	*0.100*	*-2.961*
Ta181	0.725	*0.061*	*-7.094*	0.698	*0.019*	*-10.470*
W182	0.524	*0.103*	*4.800*	0.501	*0.026*	*0.133*
Pt195	0.219	*0.055*	*-71.880*	0.065	*0.016*	*-91.731*
Au197	-	-	-	0.224	*0.042*	-
Pb208	11.933	*0.386*	*8.485*	11.543	*0.252*	*4.939*
Bi209	0.036	*0.004*	*-28.000*	0.062	*0.017*	*24.000*
Th232	5.610	*0.080*	*-4.915*	5.583	*0.186*	*-5.367*
U238	1.800	*0.088*	*6.509*	1.734	*0.034*	*2.584*

Table A6 *SHRIMP-SI average ANU internal standard measurements. Accuracy calculations by the intended H_2O values of 3870 for 24.1, 13100 dor ND60 and 10200 for ND70 (pers. comm. T. Ireland). The actual water contents of the samples were calculated by multiplying the $[H_2O]$ of the samples with the average $[H_2O]$ (=5577160.311) of all standards.*

Sample	24.1	ND61	ND70
	(n=6)	(n=5)	(n=6)
$^{16}O^{1}H/^{16}O$	6.99E-04	2.37E-03	1.81E-03
(σ)	*4.50E-07*	*4.68E-06*	*1.53E-06*
Sensitivity factor	*5536181.080*	*5571678.620*	*5622707.619*
$[H_2O]$	3899.387	13193.918	10119.342
SD	*58.837*	*1127.334*	*155.601*
Accuracy (%)	*-0.759*	*-0.717*	*0.791*
Reproducibility	*1.509*	*8.544*	*1.538*

Figure A7 *Mounted glass samples for SHRIMP-SI analyses at Australia National University (ANU), Canberra, Australia.*

Disc 1

Disc 2

Figure A7 *(continued)*

Disc 3

Disc 4

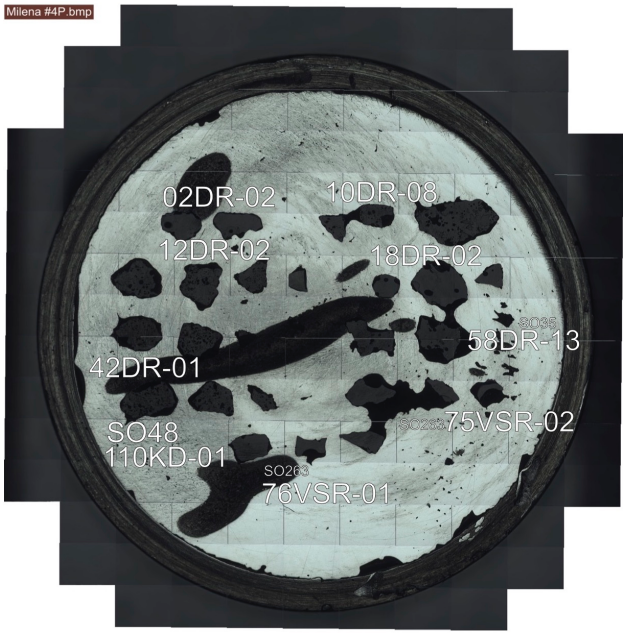

Figure A7 *(continued)*

Disc 5

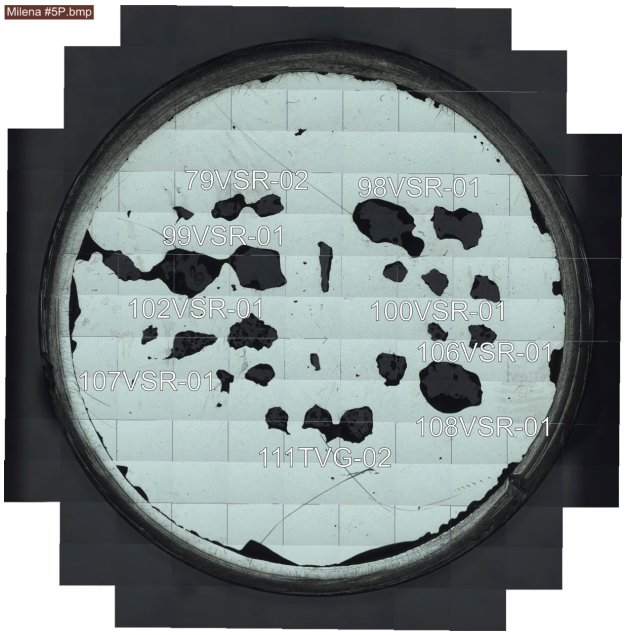

Disc 6